Fluorescence microscopy studies of molecular diffusion and interaction within self-assembled nanomaterials

by

Hao Xu

B.S., Wannan Medical College, 2011

AN ABSTRACT OF A DISSERTATION

submitted in partial fulfillment of the requirements for the degree

DOCTOR OF PHILOSOPHY

Department of Chemistry
College of Arts and Sciences

KANSAS STATE UNIVERSITY
Manhattan, Kansas

2016

Abstract

This dissertation describes the application of fluorescence microscopy techniques to investigations of mass transport phenomena in self-assembled nanomaterials. The microscopic morphologies of the materials and the mass-transport dynamics of probe molecules dispersed within them were assessed with high temporal and spatial resolution by single molecule imaging and spectroscopic methods. Three distinct sets of experiments were performed in completing the work for this dissertation.

In the first study, single molecule imaging was employed to explore the interactions and field-induced migration of double-stranded DNA (ds-DNA) molecules with nanostructured Pluronic F127 gels. While DNA interactions with nanostructured gels have been explored in the past, none had apparently looked at these interactions in gels comprising hexagonally ordered arrays of cylindrical micelles. Therefore, these studies focused on materials DNA dispersed in flow aligned hexagonal F127. DNA molecules were found to be strongly confined in the hexagonal mesophase structures from their elongation, alignment, and exclusively occurred electrophoretic migration in the direction parallel to the cylinder long axis. These observations will lead to a better understanding of macromolecular interactions with nanostructured gels like those now being investigated for use in drug delivery and chemical separations.

In the second study, imaging-fluorescence correlation spectroscopy (imaging-FCS) was used to study the rate and mechanism of sulforhodamine B (SRB) dye within novel bolaamphiphile-based self-assembled nanotubes. These nanotubes were only recently developed and their mass transport properties remain largely unexplored. The nanotubes employed here are unique because they incorporate amine groups and glucose groups on their inner and outer surfaces, respectively. Wide-field fluorescence video microscopy was first applied to locate and image dye-doped

nanotubes dispersed on a glass surface. Imaging-FCS was employed as it allows for the dynamics to be recorded simultaneously from a large sample region, thus the SRB mass transport within nanotubes can be spatially resolved. The coulombic interactions between cationic ammonium ions on the inner nanotube surface and the anionic SRB molecules was shown to play a critical role in governing dye dynamics under varied pH and ionic strength conditions. Mass transport of SRB within the nanotubes is concluded to occur by a desorption-mediated Fickian diffusion mechanism.

In the third set of experiments, solvatochromic dye molecules were employed in novel imaging-FCS studies of the role played by partitioning in governing mass transport phenomena within the same organic nanotubes used above. Two forms of the solvatochromic dye Nile Red (NR) were employed: the commercial hydrophobic form of NR, and a more polar derivative 2-hydroxybenzophenoxazinone (named NR-OH). The partitioning of dye molecules within the nanotubes was investigated assessing the diffusion rate for each dye. The preliminary results suggested NR and NR-OH preferentially partitioned into the tube walls and the ethanol phase filling the tubes, respectively. The diffusion coefficient data indicated NR-OH diffused faster than NR, consistent with the presence of NR-OH in a relatively less viscous environment (e.g., the ethanol phase filling the tubes). The results of these studies afford information essential to the use of organic nanotubes in controlled drug release and possibly in catalysis applications.

Fluorescence microscopy studies of molecular diffusion and interaction within self-assembled nanomaterials

by

Hao Xu

B.S., Wannan Medical College, 2011

A DISSERTATION

submitted in partial fulfillment of the requirements for the degree

DOCTOR OF PHILOSOPHY

Department of Chemistry
College of Arts and Sciences

KANSAS STATE UNIVERSITY
Manhattan, Kansas

2016

Approved by:

Major Professor
Dr. Daniel A. Higgins

Copyright

Abstract

This dissertation describes the application of fluorescence microscopy techniques to investigations of mass transport phenomena in self-assembled nanomaterials. The microscopic morphologies of the materials and the mass-transport dynamics of probe molecules dispersed within them were assessed with high temporal and spatial resolution by single molecule imaging and spectroscopic methods. Three distinct sets of experiments were performed in completing the work for this dissertation.

In the first study, single molecule imaging was employed to explore the interactions and field-induced migration of double-stranded DNA (ds-DNA) molecules with nanostructured Pluronic F127 gels. While DNA interactions with nanostructured gels have been explored in the past, none had apparently looked at these interactions in gels comprising hexagonally ordered arrays of cylindrical micelles. Therefore, these studies focused on materials DNA dispersed in flow aligned hexagonal F127. DNA molecules were found to be strongly confined in the hexagonal mesophase structures from their elongation, alignment, and exclusively occurred electrophoretic migration in the direction parallel to the cylinder long axis. These observations will lead to a better understanding of macromolecular interactions with nanostructured gels like those now being investigated for use in drug delivery and chemical separations.

In the second study, imaging-fluorescence correlation spectroscopy (imaging-FCS) was used to study the rate and mechanism of sulforhodamine B (SRB) dye within novel bolaamphiphile-based self-assembled nanotubes. These nanotubes were only recently developed and their mass transport properties remain largely unexplored. The nanotubes employed here are unique because they incorporate amine groups and glucose groups on their inner and outer surfaces, respectively. Wide-field fluorescence video microscopy was first applied to locate and image dye-doped

nanotubes dispersed on a glass surface. Imaging-FCS was employed as it allows for the dynamics to be recorded simultaneously from a large sample region, thus the SRB mass transport within nanotubes can be spatially resolved. The coulombic interactions between cationic ammonium ions on the inner nanotube surface and the anionic SRB molecules was shown to play a critical role in governing dye dynamics under varied pH and ionic strength conditions. Mass transport of SRB within the nanotubes is concluded to occur by a desorption-mediated Fickian diffusion mechanism.

In the third set of experiments, solvatochromic dye molecules were employed in novel imaging-FCS studies of the role played by partitioning in governing mass transport phenomena within the same organic nanotubes used above. Two forms of the solvatochromic dye Nile Red (NR) were employed: the commercial hydrophobic form of NR, and a more polar derivative 2-hydroxybenzophenoxazinone (named NR-OH). The partitioning of dye molecules within the nanotubes was investigated assessing the diffusion rate for each dye. The preliminary results suggested NR and NR-OH preferentially partitioned into the tube walls and the ethanol phase filling the tubes, respectively. The diffusion coefficient data indicated NR-OH diffused faster than NR, consistent with the presence of NR-OH in a relatively less viscous environment (e.g., the ethanol phase filling the tubes). The results of these studies afford information essential to the use of organic nanotubes in controlled drug release and possibly in catalysis applications.

Table of Contents

List of Figures

List of Tables

List of Acronyms and Definitions

1D/2D	One/Two dimensional
AAO	Anodic alumina oxide
APD	Avalanche photodiode
BCP	Block copolymer
CCD	Charged coupled device
EM	Electron microscopy
EM Gain	Electro-multiplying gain
FCS	Fluorescence correlation spectroscopy
FRAP	Fluorescence recovery after photobleaching
FRET	Fluorescence resonance energy transfer
ITO	Indium tin oxide
LC	Liquid crystal
NA	Numerical aperture
NMR	Nuclear magnetic resonance
NR	Nile Red
PDMS	Poly(dimethylsiloxane)
PEO	Polyethylene oxide
PPO	Polypropylene oxide
SMT	Single molecule tracking
TIRF	Total internal reflection fluorescence
XRD	X-ray diffraction
XS	X-ray scattering

Acknowledgements

First of all, I would like to express my sincere gratitude to my advisor, Dr. Daniel Higgins. Over the five years, I have under his mentoring with his valuable scientific guidance, endless tolerance to my mistakes and continuous encouragement. I highly appreciate his help on teaching me professional writing at the very beginning, his time on revising my paper drafts, proposal writing, and seminar abstracts. I feel so lucky and grateful to have him as my major professor and advisor for my Ph.D. study.

I also thank my co-advisor, Dr. Takashi Ito, for his scientific advice, especially in electrochemistry and nanomaterial fields. His useful suggestions always help me to catch the critical points in my research. I would also like to thank to Dr. Stefan Bossmann, Dr. Philine Wangemann for being on my supervisory committee, and Dr. Anna Zolkiewska for her services at my final Ph.D. examination as the outside chairperson.

I am very thankful to have my previous and current labmates and friends. Dr. Seok Chan Park and Dr. Khanh-Hoa Tran-Ba are especially acknowledged for the time on showing me all the tricks to use the wide-field microscope. Without their help, I could not have made a continuous progress in my research. Dr. Dipak Giri, Dr. Xiaojiao Sun and Kaushalya Perera are also thanked for the interesting discussions on research and daily topics. My friend, Man Zhang, is acknowledged for her patience and time helping me on the synthesis experiments. I also thank all other members of Higgins group: Zi Li, Ruwandi Kumarasinghe and Judith Batusta. It was fun to have you around and I enjoyed a lot working with you guys.

Our collaborators, Naohiro Kameta and Mitsutoshi Masuda from Japan National Institute of Advanced Industrial Science and Technology (AIST), are thanked for providing us the organic nanotube samples and the monomers, also the nanotube structure figure that I applied in the paper.

I greatly acknowledge the faculty and staff in Department of Chemistry at K-state. Especially Mrs. Shinobu Ito for her valuable time on synthesis and preparation of nanotube samples, and teaching me AFM. Also, Christopher Minter is thanked for his early work on the DNA project. Tobe Eggers, Ron Jackson and Jim Hodgson are also thanked for fixing our stubborn electrical instruments, providing me the tools of substrate polishing and tubular glassware, respectively. I also acknowledge the funding support from U.S. Department of Energy to our research projects.

Finally, my sincerely gratitude goes to my wonderful family for their unconditional love, support, understanding and patience as always. I am also blessed to have all my friends in the U.S. and China supporting me during these years. I am very grateful to have their companies through my good and tough times.

Dedication

This work is dedicated to my loving and proud parents, Qin & Zhongdong.

Chapter 1 - General Introduction

Materials are what the world is made of. A broad range of materials properties, from fracture strength to electrical conductivity, depends on the nanometer-scale features of a given material. Indeed, some materials are designed to incorporate features on nanometer length scales and these nanoscale features often employed to access certain physical or functional characteristics of the materials. Nanostructured materials are designed as materials having features (e.g., single units) smaller than 100 nm. Top-down and bottom-up approaches are two strategies commonly employed to generate nanostructures. The self-assembly approach allows nanostructures synthesized by bottom-up methods to self-organize into regular patterns or structures by using local forces to find the lowest-energy configuration. Self-assembled nanostructures include a wide range of complex components in life, such as lipid membranes, structured nucleic acids, folded proteins and protein aggregates. Self-assembly also affords one of the most general and effective strategies to form regular nanostructures, including liquid crystal mesophases,[1] molecular crystals,[2] and phase-separated polymers.[3]

Among the large variety of self-assembled nanomaterials, cylinder-shaped nanostructures have become the focus of intensive research because of their unique applications in mesoscopic physics and in the fabrication of nanoscale devices.[4] Their potential applications include their use in chemical separations,[5] drug delivery,[6] and heterogeneous catalysis.[7,8] In such applications, the interactions between the nanostructures and any included guest molecules are especially important. To reveal the key aspects affecting the interaction and performance of the cylindrical nanomaterials in their potential applications, a full understanding of their properties is necessary. This goal can be fulfilled by high-resolution quantitative characterization of their nanostructures.

The morphology and structural characteristics of self-assembled cylindrical nanomaterials usually can be assessed by electron microscopy (EM),[9-14] X-ray scattering (XS)[4] and nuclear magnetic resonance (NMR) spectroscopy.[15] XS affords average information about the orientation and spacing of ordered nanomaterials within a macroscopic (< 1 mm) sample region. EM provides nm-scale spatial resolution of the nanostructure properties, and a means for visualizing the local structures. However, EM can only be used to image microscopic regions of a given sample, making it time-consuming to study larger areas area (> 10 μm) of the sample. Moreover, none of these methods provide access to both spatial and temporal resolution of mass transport characteristics in the nanostructures. NMR can detect the dynamics of the molecules within the nanomaterials, but it can only provide average information over a relatively large sample region.[16]

Single molecule tracking (SMT) has recently been employed as an unique method to overcome the above limitations.[17,18] SMT is used in exploring relatively slow diffusion of molecules in nanostructures. SMT is used to generate single-molecule trajectories to qualitatively reveal the local mass transport processes and material nanostructures with nm-scale spatial precision and millisecond temporal resolution. It is especially valuable in studying dynamic behaviors and material characteristics in 1D cylindrical nanostructures.[19] SMT can provide specific information on the macroscopic alignment of the 1D structures found within cylindrical nanomaterials, on their sizes and on their continuity. However, they are limited to relatively slow molecule motion. For molecules that move too quickly to be tracked by SMT methods, FCS provides a valuable means to both detect and quantify this motions by autocorrelating the fluorescence fluctuations derived from molecule motion in the detection region.[20] FCS provides information about the diffusion rates, dimensionality, and absorption/desorption kinetics of the molecules, thus revealing the properties of the nanostructures. Imaging-FCS, as a multichannel

variant of the traditional FCS, is able to obtain diffusion information from a relatively broad sample region (e.g. ~3 μm x 3 μm) simultaneously, although by sacrificing some time resolution.[21,22]

1.1 Objectives and Motivations of the Present Research

In the present dissertation, single molecule imaging, imaging-FCS and spectroscopic imaging were used to characterize the mass transport dynamics of guest molecules dispersed within nanostructured materials. Two types of nanostructures were explored: 1) Pluronic F127 micelles assembled into hexagonal mesophases and 2) self-assembled bolaamphiphile-based organic nanotubes. The primary objective of the studies performed for this dissertation is to explore the interactions between the nanostructures and guest molecules passing through them. Along the way, information on the characteristics of the nanomaterials is also obtained. The results obtained help to define the potential utility of the nanomaterials investigated in certain technological applications.

Single molecule imaging was employed to study the interactions between DNA molecules and the microdomains of hexagonal F127 hydrogels. These gels contain DNA, F127 polymer, water and butanol and were flow aligned by injection into a microfluidic channel. Small angle X-ray scattering (SAXS) was used to characterize the size and order of the hexagonal mesophase domains. DNA interactions with the hydrogel are important to their potential applications in drug delivery and chemical separation. The elongation, alignment and electrophoretic migration of DNA were investigated within flow aligned hexagonal F127 mesophases. The obtained information also reveals the flexibility and continuity of the F127 cylindrical domains.

Another cylindrical nanomaterial studied in this dissertation is the self-assembled organic nanotubes derived from bolaamphiphile surfactants. The fundamentals of the interactions between the guest molecules and the organic nanotubes must be fully understood prior to their use in applications such as drug delivery and heterogeneous catalysis. Imaging-FCS studies were performed in this case using dye molecules of different charges and hydrophobicities. The molecular diffusion rate and the mechanism of mass transport in the organic nanotubes were both investigated. Probe partitioning within the organic nanotubes was qualitatively analyzed by two-color imaging microscopy.

1.2 Outline of the Present Dissertation

This dissertation consists of eight chapters. Chapter 2 describes phase separated block copolymers. Their properties and mesophase assemblies are elucidated, as well as the flow alignment of the F127 gel. Self-assembled organic nanotubes are also discussed in this chapter. Information about the formation mechanisms and applications of organic nanotubes are given. The nanotubes formed by asymmetrical bolaamphiphiles are highlighted. In Chapter 3, the sample preparation and characterization techniques applied in this dissertation are introduced. The methods of characterization include SAXS, wide-field fluorescence microscopy and imaging-FCS. In Chapter 4, the interactions between DNA molecules and the F127 gel comprising cylindrical microdomains are investigated. Elongation, alignment, and electrophoretic motion of DNA molecules are assessed by single molecule imaging. Chapter 5 demonstrates the application of imaging-FCS in the study of dye molecule diffusion within organic nanotubes. The diffusion coefficients obtained are reported and a model for the molecule dynamics is established. In Chapter

6, different charged dye probes with varied hydrophobicity are employed to study diffusion within the same organic nanotubes. Imaging-FCS allows for accesses to the dye transport information, while spectroscopic imaging provides partitioning information of the dye molecules. Chapter 7 summarizes all the achievements and results of this dissertation. Future directions are also proposed. Finally, a list of reference cited in this dissertation is given.

Chapter 2 - Self-assembled Nanomaterials

The term 'nanomaterials' describes materials that have structured components with at least one dimension in between 1 and 100 nm. Nanomaterials can be generated by 'top-down' or 'bottom-up' approaches. Top-down[23] approach uses various lithography methods to pattern materials. In bottom-up approach, it employs the techniques of molecular synthesis[24], colloid chemistry,[25] polymer science[26] to build up structures in nanometer dimensions. As one of the bottom-up methods, 'self- assembly' enables the fabrication of materials with the fine resolution and the long-range structures.[27] Self-assembly is a process in which individual components spontaneously organize themselves into ordered patterns. The interactions involved usually are non-covalent, such as hydrogen bonding, electrostatic interactions, van der Waals' forces, coordination interactions and solvophobic effects.[27]

This chapter will introduce two types of self-assembled nanomaterials: self-assembled block copolymers and organic nanotubes. Both of these materials are critical to various scientific applications, including material templates and drug carriers.[27-29] Their properties and applications will be discussed in detail in the text that follows.

2.1 Phase Separated Block Copolymers

One well-known class of self-assembled nanomaterials is derived from block copolymers (BCP). BCPs are macromolecular amphiphiles consisting of chemically distinct homopolymers (blocks) that are covalently linked to each other. BCPs have attracted significant research interests because they often undergo 'microphase separation' to form periodic nanostructures, as shown in **Figure 2.1**. The various nanostructures formed by BCPs include hexagonal, lamellar

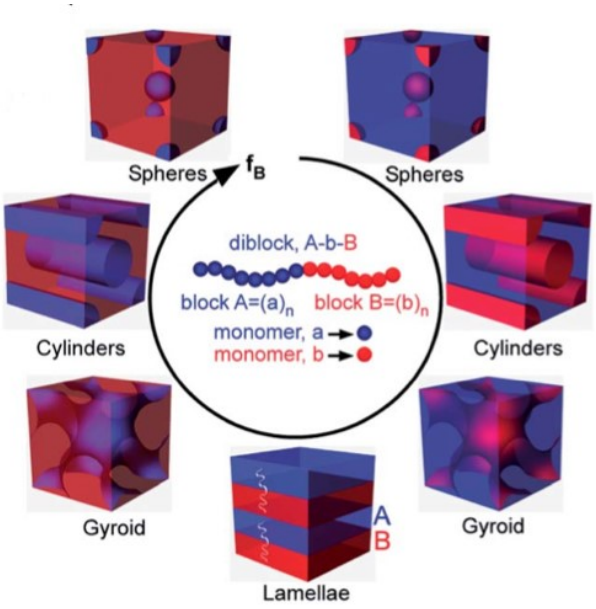

Figure 2.1 Microstructures of diblock A-b-B (block A consists of monomers 'a' and B is made of monomers 'b') with increasing volume fraction of the B block. f is volume fraction of one of the blocks.[30] Reproduced with permission from Ref (30). Copyright 2014 Royal Society of Chemistry.

and spherical structures. Therefore, BCPs offer great potential for designing nanostructured materials and devices. In particular, spherical micelles are known to encapsulate a variety of guest molecules, which makes them useful as drug carriers in drug delivery systems.[29] Other applications of BCPs include their use for creating nanoporous materials,[28,31] as templates to incorporate nanoparticles[32] or biomolecules[33] and as switchable smart surfaces.[34] The nanostructured phases formed by BCPs in aqueous media (i.e., from micelles to gels) also makes them broadly employed in industrial applications, where they are often used as detergents, emulsifiers, and lubricants.

Pluronic polymers are an important class of triblock copolymers that have been shown to be biocompatible and biodegradable. They are nonionic surfactants composed of two polyethylene oxide (PEO) blocks and one polypropylene oxide (PPO) block with a general formula, $PEO_{(x)}$–$PPO_{(y)}$–$PEO_{(x)}$. Pluronics have been successfully applied in drug and gene delivery systems as

they readily solubilize drugs/genes and form polymer-drug/gene associations.[35,36] The incorporation of target molecules into Pluronic micelles can also increase the solubility and stability of some physiologically unfavorable drugs, and also improve the *in vivo* bio-distribution of drug molecules.

Because of its availability and potential utility, F127 ($PEO_{100}PPO_{65}PEO_{100}$), one of the Pluronic polymers, was employed in work described in this dissertation (Chapter 4). The molecular structure of F127 is shown in **Figure 3.2**. Its thermodynamic and phase separation properties have been systematically investigated since 1998.[37] The next section will describe a few important characteristics related to the nanostructure of F127, and how these characteristics influence the interactions between F127 and incorporated guest molecules.

2.1.1 Properties of Block Copolymer F127

Triblock F127 monomers form micelles at certain polymer concentrations and temperatures. The micellization of F127 in aqueous media is driven by heat-induced dehydration of its hydrophobic blocks. The temperature needed to induce dehydration is related to the critical micellization temperature (T_{cm}). At a temperature below T_{cm} for a particular solution, both the hydrophobic and hydrophilic blocks are hydrated and dissolved, hence, F127 polymer is in a solution form. When the temperature is raised above T_{cm}, dehydration of the hydrophobic blocks results in a solubility decrease and aggregation of the blocks, while the hydrophilic blocks maintain their solubility. For F127, this aggregation results in the formation of micelles consisting of a 'core' dominated by the hydrophobic PPO blocks and a 'corona' formed by the hydrophilic PEO blocks. Overall, F127 (typically 15%-40% concentration, by weight) is in a liquid state below ~20ºC, and forms a gel under relatively high temperature conditions.[38] The polymer concentration also affects

the type of micelles formed. Generally, when the concentration increases, T_{cm} will decrease, and large micelles consisting of a larger number of polymers will form.

2.1.2 Mesophase Assemblies of F127

In solutions of high micelle concentrations, the micelles often self-organize into assemblies of nanostructures. For a copolymer of a given block composition and molecular weight, the type of assembly obtained depends on the polymer-solvent composition. The assemblies formed are usually called mesophases, in which the assembled nanostructures have repeat distances falling between 2 and 50 nm. The formed mesophase assemblies are due to unfavorable interaction between polymer segments. Generally, the resulting structure maintains the lowest interfacial area and increased configurational entropy compared to other morphologies, which is an overall energetically favorable system.[39]

This phase separation can be attributed to three components of the system free energy: the degree of stretching of the core blocks, the interfacial tension between the micelle core and the solvent outside the core, and the repulsive interactions within the corona chains. Thus, the morphologies can be controlled by factors affecting any of the three contributions, including copolymer type, copolymer composition and concentration, water content in the solution, nature of the common solvent and presence of additives.[40] Phase separation depends on three parameters. First, Flory-Huggins parameter, χ, describes the incompatibility between two constituent immiscible blocks, which is typically inversely proportional to the temperature. Second, phase separation is affected by the total degree of polymerization N. Finally, the volume fractions f of the thermodynamically different blocks controls the forming morphologies.[41,42] For diblock copolymers, when polymer concentration is high enough, a lamellar phase can be obtained from

symmetric diblocks (f = 0.5). Increasing the degree of compositional asymmetry leads to cylindrical, and finally, spherical phases.[43] Multiblock copolymers have been found to form more than 30 different morphologies, a much higher level of complexity than is observed for diblock copolymers.[44]

In our studies, the F127 mesophase assemblies employed are those that develop in ternary copolymer-water-oil mixtures. In 1998, Linderman and Alexandridis et al. completed the comprehensive study of ternary phase diagrams for several Pluronic block copolymers, including F127, in Pluronic-water-butanol mixtures.[37] The microstructures they discovered included cubic, hexagonal, lamellar mesophases of spherical and cylindrical micelles as well as planar structures. For the studies described in Chapter 4, the concentration of each component in the ternary phase diagram was carefully selected to form cylindrical micelles that self-organize into the hexagonal mesophase. The hexagonal mesophase was of primary interest in this investigation because its one dimensional structure was believed to afford an efficient route to flow aligned materials.[45,46]

2.1.3 Flow-alignment of Block Copolymers in the Hexagonal Mesophase

Cylindrical polymer domains in hexagonal mesophase have been frequently used as templates in many technology applications, especially in thin films. Thus, it is important the mesophase structures are relatively defect-free. To obtain hexagonal mesophase, it is usually hard from spontaneously formed polymer sol-gels, since they most likely do not exhibit long-range order, and consist of a large number of defects, such as dislocations and disclinations. Due to the inherent softness of the block copolymers (i.e., high viscosity of polymer liquids), macroscopic pore order can be achieved by external guiding force, for example using electric fields, surface patterns, or shear forces.[42]

In 1993, shear flow was shown to be a practical method for inducing macroscopically anisotropic polymer domains. Albalak and Thomas conducted a 'roll-casting' experiment and obtained long range cylindrical and lamellar microdomains for film thicknesses down to 50 μm.[47] In this study, polymer solutions in toluene were rolled between two co-rotating cylinders; meanwhile, the solutions were removed at a controlled rate. After solvent evaporation, oriented macroscopically aligned domains formed by hydrodynamic flow and gradual drying of the polymer solution between the two cylinders. In 2004, Angelescu et al. successfully prepared macroscopically oriented block copolymer monolayers by shear flow.[48] The AFM measurements revealed arrays of microdomains in the ~30 nm thick polymer film. The shear-induced flow in this work was imparted by the slow displacement of a poly(dimethylsiloxane) (PDMS) pad on top of the copolymer 'melting' film.

Techniques such as electron beam lithography (EBL) could also be employed to fabricate grains for polymer 'melts' to obtain ordered block copolymer domains.[49-51] EBL is limited by its small working scales (usually in nanometer or micrometer scales). However, industry needs require the alignment of microdomains over large areas (e.g. centimeter scale). It would be very time-consuming for preparing large area structures by using EBL. Flow-alignment procedures, on the other hand, provide a convenient route to achieve long-range ordered polymer domains, although it contains random detects which limits the order.

2.2 Self-assembled Organic Nanotubes

Organic nanotubes represent another important class of self-assembled, one-dimensional, porous nanomaterials. Porous nanomaterials, including metal–organic frameworks,[52,53] nano- and

mesoporous cylinder arrays,[54] nanotubes, and nanocapsules,[55] possess different internal dimensions and surface properties, which allow them to be used for the capture, storage, and release of drugs, pollutants, reagents, analytes, etc. Therefore, nanoporous materials have significant potential applications as matrices for drug delivery, catalysis, bioengineering, and chemical separations, to name a few. Among these materials, nanotubes including carbon, silicon, and organic nanotubes have attracted growing attention because of their cylindrical shape and spacious interior. In 1984, three groups reported pioneering work describing the self-assembly of lipid nanotubes from synthetic amphiphile molecules.[56,57] Since then, many more types of nanotubes consisting of organic molecules and macromolecules, named 'organic nanotubes', have been synthesized, and their applications have been actively investigated.

Compared to other nanotube materials, organic nanotubes exhibit better biodegradability and biocompatibility,[58,59] making them promising materials for use in bioengineering and medicine. In addition, the surfaces, morphologies, sizes, and functionalities of organic nanotubes can be easily and precisely controlled by modification of the nanotube monomers and/or the tube-forming process. The following discussion in this chapter will explain the organic nanotube formation process, introduce a special and crucial class of organic nanotubes formed by asymmetrical bolaamphiphiles, and finally discuss the applications of organic nanotubes in various fields.

2.2.1 Formation Mechanisms of Organic Nanotubes

Organic nanotubes can be prepared via two types of methods. One is to assemble small amphiphilic molecules into tube-shaped entities. Assembly processes of this type include chiral self-assembly, scrolling of sheets and packing-directed self-assembly. Macromolecules can also form nanotubes by molecular sculpting and templating procedures, which are fulfilled by cross-linking of polymer segments and applying templates. **Figure 2.2** summarizes the mechanisms of "these formation processes.

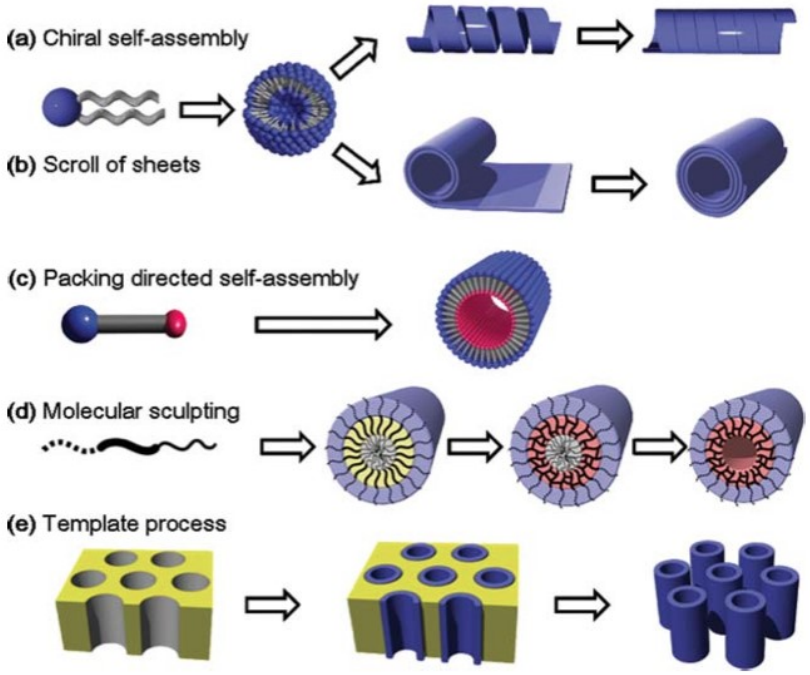

Figure 2.2 Formation mechanisms of organic nanotubes: (a) chiral self- assembly, (b) scroll of a sheet, (c) packing-directed self-assembly, (d) molecular sculpting, and (e) template process.[6] Reproduced with permission from Ref (6). Copyright 2011 Royal Society of Chemistry.

Chiral Self-assembly

Low-molecular-weight amphiphiles with chiral centers form nanotubes by chiral self-assembly. When cooling from hot aqueous solution, some amphiphiles form bilayer-membrane

structures. As the temperature cools below $T_{gel\text{-}lc}$ (the gel-to-liquid crystalline phase transition temperature), the self-assemblies grow into one-dimensional tapes. When chiral amphiphiles are employed, these tapes further assemble into helical ribbons that form tubular structures. This latter step is directly induced by molecular chirality.

Scrolling Approach

For achiral molecules, no spontaneous twisting of the self-assembled tapes occurs. Rather, the flat membranes spontaneously scroll into tube shape structures, as shown in **Figure 2.2(b),** to reduce the surface area exposed to solution, and hence, their surface energy. However, in relatively concentrated solution, flat membranes may stack onto each other.[60,61]

Packing-directed Self-assembly

Wedge-shape amphiphiles can form tube shapes directly without a helical ribbon intermediate. When the amphiphiles possess hydrophobic chains in a fluid state, a structural guideline can be applied to predict the aggregate morphology for diblock copolymers. Israelachivili proposed a model of self-assembly morphologies depending on the critical packing parameter P,[62]

$$P = v/a_0 \times l_c \qquad \text{(Eq. 2.1)}$$

where v is the volume of the hydrophobic chain of the amphiphile, a_0 is the polar head surface area at the critical micelle concentration, and l_c is the amphiphile chain length. When $P < 1/3$, the amphiphiles are likely to assemble into spherical micelles; if $1/3 < P < 1/2$, they tend to form cylindrical hollow tubes; when $1/2 < P < 1$, bilayers with a spontaneous curvature (vesicles) will be favored; if $P = 1$, planar bilayers are produced; and if $P > 1$, micelle aggregates can be formed with a reverse curvature.

Molecular Sculpting and Templating

A triblock copolymer with cross-linkable middle block can be used to produce nanotubes by molecular sculpting. In this process, the block copolymers first self-assemble into cylindrical micelles, and the middle block is subsequently cross-linked. Finally, the micelle core is chemically removed to form open nanotubes. The process is shown in **Figure 2.2(d)**.

Templating is another effective method to prepare nanotube structures.[63] Typically, a nanoporous template, such as an anodic alumina oxide (AAO) membrane, is employed for nanotube construction. Macromolecules are first absorbed onto the nanopore surfaces, then the template is removed to release the nanotubes. The templating process allows for precise dimensional control of the resultant nanotubes. However, removal of the templates requires harsh conditions, such as exposure to acidic or basic solutions, which may damage the nanotubes.

2.2.2 Organic Nanotubes Formed by Asymmetrical Bolaamphiphiles

Amphiphiles that have two different hydrophilic headgroups and a hydrophobic chain in between, are often called asymmetrical bolaamphiphiles.[64,65] These materials afford an important route to self-assembled organic nanotubes having tunable diameters and surface chemistries. Because of these attributes, bolaamphiphile-based nanotubes are employed in the work described in Chapters 5 and 6 of this dissertation. The nanotubes obtained from bolaamphiphiles have certain specific and important attributes. First, the use of asymmetrical bolaamphiphiles allows for tubes having different inner and outer surfaces to be prepared. The resulting differences in tube surface chemistries allow for selective surface functionalization,[66] efficient loading of the nanotubes with reagents, drugs and analytes,[67] and controlled release of biomolecules.[68] Especially, the outer surfaces can be modified with glucose groups, which lead to in an effective biocompatibility *in*

vivo.[22] Second, the diameter of the asymmetrical nanotubes can be precisely controlled by changing the molecular shape.

When applying asymmetrical bolaamphiphiles, the control over molecular packing is necessary to ensure the resultant nanotubes possess distinct inner and outer surfaces. Among all the packing possibilities, only parallel packing and head-to-tail stacking of bolaamphiphile monomers can form asymmetrical nanotubes.[6] It has been found that hydrogen bonds play a critical role in molecular packing. Shimizu and coworkers found that the introduction of triglycine moieties into the bolaamphiphiles with amine and glucose moieties as end groups enables the regulation of parallel molecular packing via polyglycine-II-type hydrogen bonding, resulting in the formation of asymmetrical organic nanotubes.[69,70] Liu et al. reported that an Aβ-peptide with a cytosine base dyad, ccQALVFFA–NH_2, exclusively formed asymmetrical nanotubes.[71] While nanotubes formed from the same peptide without the cytosine residue resulted in a molecular packing of antiparallel β-sheets.[71,72] Ordered porous alumina templates can also be employed with a layer-by-layer deposition method to prepare nanotubes with different inner and outer surfaces.[73,74]

Generally, control over the resulting nanotube dimensions (inner diameter, outer diameter and length) can be achieved by changing the solvent conditions during self-assembly (i.e., pH, solvent composition, ionic strength),[75] the structure of the lipids,[76] and the composition of the lipid mixtures for complex assembly systems.[77]

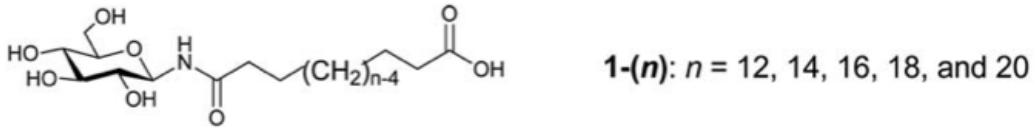

Figure 2.3 Chemical structure of α,ω-Bipolar amphiphiles with glucose and carboxylic acid head groups, with varied carbon chain length.[6] Reproduced with permission from Ref (6). Copyright 2011 Royal Society of Chemistry.

Kameta and coworkers have found that the inner diameter (D_{in}) of nanotubes formed by packing-directed self-assembly of asymmetrical bolaamphiphiles **1–(*n*)** (n = 14, 16, 18, and 20) follows the simple model[6] given in Eq. 2.2. The structure of **1** is depicted in **Figure 2.3**.

$$D_{in} = 2A_{small}L/(A_{small} - A_{large}) \quad \text{(Eq. 2.2)}$$

According to this equation, D_{in} can be estimated from the cross-sectional areas of the two head groups (A_{small} and A_{large}) and the molecular length (L) of the amiphiphile monomer. The inner diameter can be adjusted by varying the length of the oligomethylene chain (n) in **1–(*n*)**. The Shimizu group also confirmed this model: for the same lipid head groups, when n increased from 14 to 20, D_{in} enlarged from 17 to 22 nm.[64] The diameter of the tubes can also be affected by temperature. In Douliez's work, an ethanol amine salt of racemic 12-hydroxy stearic acid formed nanotubes with an outer diameter of 0.6 μm at room temperature.[78] At 48ºC, the diameter increased to 4 μm. Upon further heating, a flat tape morphology was formed and then tubular structures with 2 μm diameters formed again until the structures melted at 65ºC.[78,79] X-ray diffraction (XRD) measurements were conducted to illustrate the phenomenon. From these studies, it was shown that heating decreased the molecular packing order of the original chiral self-assemblies and increased the tube diameter until the tubular structure collapsed into tape shapes. Furthermore, it was suggested that heating might induce bilayer interdigitation, which could lead to chiral crystallization and hence, reformation of the nanotube structures. Tube lengths can be regulated by changing the solvent composition,[80] cooling rate[81,82] and addition of metal salts.[83]

2.2.3 Applications of Organic Nanotubes

Because of the numerous possible modifications that can be made to the nanotube dimensions and structure, they have many potential applications, especially in the bioengineering field. Their possible applications include their use as nanocarriers of anti-cancer drugs in drug delivery systems, as vectors for nonviral gene transfer, as heterogeneous oxidation catalysts, and as nanopipettes.[84]

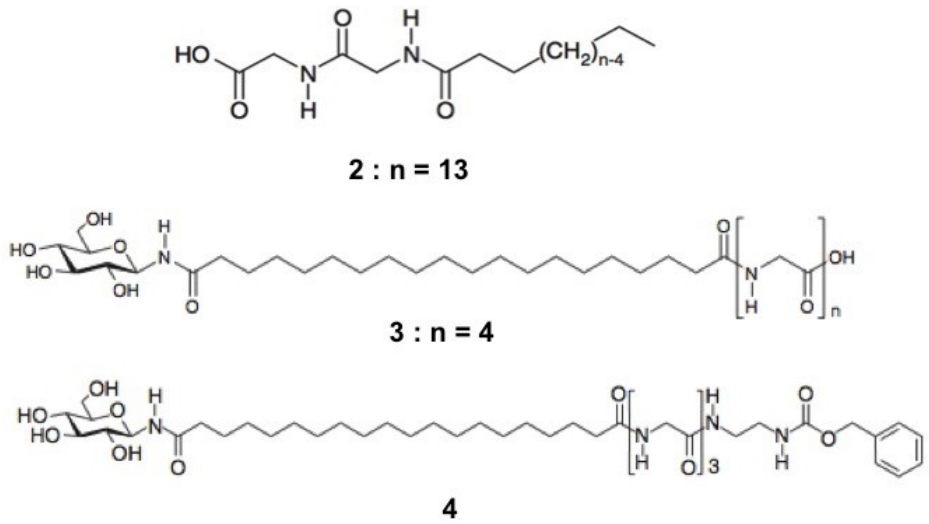

Figure 2.4 Molecular structure of amphiphiles 2-4.[84] Adapted with permission from Ref (84). Copyright 2014 Nature Publishing Group.

<u>*Nanocarriers in Drug Delivery Systems*</u>

Organic nanotubes may serve as nearly ideal carriers in drug delivery systems. The adjustable inner nanospace can be used to encapsulate molecules with a range of sizes from very small organic or organometallic molecules to high molecular weight macromolecules, including proteins and DNA.[85-87] The inner and outer surfaces of the organic nanotubes can be modified to obtain high bio-compatibility and selectivity by electrostatic interactions,[88-90] hydrophobic interactions,[91] prodrug conjugation[92] and chelate formation.[93,94] One attractive advantage of using

organic nanotubes as drug vehicles is the shape effect[95] which can be applied *in vivo*. It has been found that the high axial: radial ratio of flexible filament micelles enables longer persistence times in the blood than using spherical polymersomes.[95] Early work employing this class of organic nanotubes in drug delivery applications involved the encapsulation of doxorubicin hydrochloride (an anticancer drug) into the nanotubes.[89] Drug delivery was tested using individual cells. The nanotubes employed were assembled from amphiphile **2** (**n**=13, as shown in **Figure 2.4**). Later *in vivo* studies revealed that these anionic nanotubes specifically accumulated in the lungs of mice.[90] Thus, this type of nanotube might be the most useful as a lung-targeting drug delivery system. Organic nanotubes derived from mixtures of amphiphiles **3** and **4** introduced the hydrophobic benzyloxycarbonyl (-Cbz) group into the inner space of the nanotubes.[88] This allowed for the controlled release of doxorubicin hydrochloride. The results demonstrated the released amount of doxorubicin hydrochloride at 48 h decreased significantly to <10% for the hybrid nanotubes with the molar ratio of **3**/**4** = 6:5, while the nanotubes assembled from only **3** released 60% of doxorubicin hydrochloride.

The inner tube surfaces can be modified to allow for encapsulation and release of specific drugs. For example, chelate formation has been applied to encapsulate platinum-based anticancer drugs into organic nanotubes.[94] The chloride on the anticancer drug cis-dichlorodiammineplatinum(II) (CDDP) was replaced by the carboxylate group on the inner surface

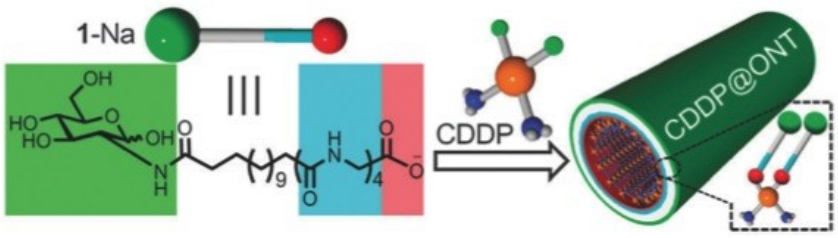

Figure 2.5 CDDP-assisted assembly of organic nanotubes.[94] Reproduced with permission from Ref (94). Copyright 2012 Royal Society of Chemistry.

of the nanotubes (**Figure 2.5**), so that the drug molecules selectively localized on the tube inner surfaces. Coordination of the cisplatin resulted in its slow release from the nanotubes in HEPES buffer solution.

Nonviral Gene Transfer Vectors

Organic nanotubes can also be used to transfer genetic drugs *in vivo*.[96] Hsieh and coworkers prepared cationic peptide nanotubes by assembly of dipeptides (H-Phe-Phe-NH_2·HCl) at physiological pH values.[97] Negatively charged nucleic acids were able to strongly bind to the outer surfaces of the nanotubes and be delivered into cells. The authors demonstrated that the nanotubes spontaneously converted to vesicles when diluted. The vesicles formed traversed the cell membrane and effectively delivered their nucleic acid cargo. Later, it has been found that nanotubes of short lengths were able to act as delivery carriers without inducing changes to their morphology. Organic nanotubes co-assembled with three different amphiphiles (with the added ones having arginine and polyethylene glycol (PEG) moieties on the outer surfaces) efficiently formed complexes with plasmid DNA, and remained of tubular morphology *in vivo*.[98] While long nanotubes (> 1μm) mostly attached on the cell surfaces, shorter ones that were 400–800 nm in length successfully entered into the cells and delivered DNA into the cytoplasm.

Heterogeneous Oxidation Catalysts

Heterogeneous catalysts supported on 1D nanostructures such as nanotubes have recently been prepared.[99-101] Nanotubes are promising catalyst supports because they possess large inner and outer surface areas and the morphology of the structures simultaneously suppresses agglomeration. Significant interest in heterogeneous catalysts in general has arisen lately because their use allows for reaction products to be more easily recovered than when homogeneous catalysts are used. Organic nanotubes have been employed to catalyze Diels-Alder reactions[99] and the hydrolysis

from *p*-nitrophenyl acetate to *p*-nitrophenol.[100] Among various organic nanotubes, the carboxylate-terminated peptide lipids are especially promising, because the terminal carboxylate groups can coordinate with metal ions that often exhibit catalytic activity in oxidation reactions.[102] For example, Shimizu and coworkers utilized Cu-tube and Ni-tube complexes to catalyze the oxidation of primary and secondary alcohols, an α,β-unsaturated alcohol, olefin derivatives, aldehydes and a variety of other organic compounds.[103,104] The nanotube-metal ion complexes were stable and remained as tubular structures under the reaction conditions employed. The catalyst showed ~80% selectivity for both Cu-tube and Ni-tube complexes, and ~60% conversion for Ni-tube complex and ~20% for Cu-tube complex.

Nanopipettes

In attoliter chemistry, it is of importance in controlling manipulation and delivery of a small volume of liquid.[93,105,106] Organic nanotubes can be applied as a nanopipette to be fixed to the end of a glass micropipette so that an attoliter-order volume of liquid can be delivered through it.[107] The interface of the nanotube and micropipette can be sealed with photo-crosslinkable resin. The release of liquid was controlled by applying voltage from 0-526 V. By using nanotubes as disposable 'tips' instead of fabrication of nanopipettes directly, significant manufacturing time and effort could be saved.

2.3 Summary

In this chapter, two important types of nanomaterials were introduced. The characteristics of assembled F127 hexagonal mesophases and the flow-alignment of the F127 hydrogel were elucidated. This F127 hydrogel is employed in Chapter 4 and incorporates with ds-DNA molecules

to study the interaction between the two. The organic nanotubes self-assembled from asymmetrical bolaamphiphiles were described in this chapter as well. The unique properties brought by the distinct inner and outer tube surfaces make the tubes promising in many technological applications. Chapters 5 and 6 utilize this type of organic nanotube and investigate probe diffusion and probe interaction within the tubes.

Chapter 3 - Experimental Considerations

This chapter is devoted to describing the specific materials applied in this dissertation, including the properties of YOYO-1 dye as a stain for DNA molecules, the F127 hydrogel preparation and the synthesis of the organic nanotubes used in Chapters 5 and 6. It also covers the instrumentation and specific spectroscopy methods applied in the data acquisition. Chapters 4 and 5 give more specifics on experimental setups and sample preparation conditions.

3.1 YOYO-1 Dye as a Stain for DNA

To visualize DNA and detect its motion in a fluorescence microscope, it is necessary to stain the DNA with dye molecules. Generally, there are three types of classic nuclei acids stains: intercalating dyes, minor-groove binders and other base-pair selectively binding stains. The intercalating dyes involve primarily bis-intercalation. That is, for dye molecules that have two monomer units, each unit intercalates between the bases of DNA backbone.

YOYO-1, as a well-known bis-intercalator (**Figure 3.1b**), has been frequently applied in DNA staining owing to its exceptional sensitivity for nucleic acids. YOYO-1 dyes are symmetric dimers in the cyanine dye family. The structure is shown in **Figure 3.1a**. Four positive charges are present on each molecule, which lends the dye a high affinity for ds-DNA. YOYO-1 is essentially non-fluorescent in the absence of nucleic acids. Upon intercalating into the DNA double strand, its fluorescence is enhanced 100- to 1000-fold, giving a high quantum yield (generally between 0.2 and 0.6).[108] The fluorescence obtained from intercalated YOYO-1 is sufficient for detecting single molecules of labeled nucleic acids by optical imaging. Upon intercalating into DNA molecules, YOYO-1 has a maximum absorption at 489 nm and maximum fluorescence emission

at 509 nm. In the fluorescence imaging experiments of Chapter 4, a blue diode laser (488 nm) was used to excite the YOYO-1 dye. Since the association of YOYO-1 and DNA is highly stable, YOYO-1 is also widely used for doping nucleic acids prior to electrophoresis.

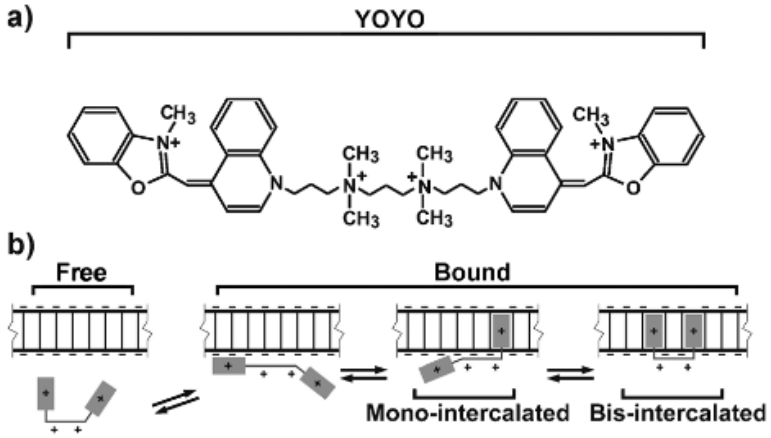

Figure 3.1 (a) Structure of YOYO-1 dye. (b) Binding states of YOYO-1.[109] Reproduced with permission from Ref (109). Copyright 2012 WILEY-VCH Verlag GmbH & Co. KGaA, Weinheim.

However, some mechanical properties of DNA are altered by intercalation of YOYO-1, such as the contour length[110] and the overstretching transition of the DNA.[111] The contour length is increased with YOYO-1 intercalation. For example, staining at a 13:1 ratio of base pairs to YOYO-1 increases the contour length of λ-DNA from 16.5 μm to 19.3 μm.[112] Therefore, the effects of introducing YOYO-1 dyes for staining need to be taken into consideration in experiments, especially in which the mechanical properties of DNA play an essential role in the results.

3.2 Preparation of F127 Hydrogel

F127 gels applied in Chapter 4 were prepared by mixing F127, 2-amino-2-hydroxymethylpropane-1,3-diol (tris), HCl, butanol and YOYO-1 doped DNA. The tris and HCl formed a 0.1 M buffer with pH = 7.5. **Figure 3.2** shows the ternary phase diagram for F127, water

and butanol. Two different samples were employed in these studies; these fell within the hexagonal and cubic regions, labeled H_1 and I_1 on the phase diagram, as designated by the small black circles. The hexagonal region comprises a hexagonal arrangement of cylindrical micelles. The cubic region represents a cubic assembly of spherical micelles in which the mesophase has isotropic characteristics. The specific compositions of the samples are defined in **Table 3.1**.

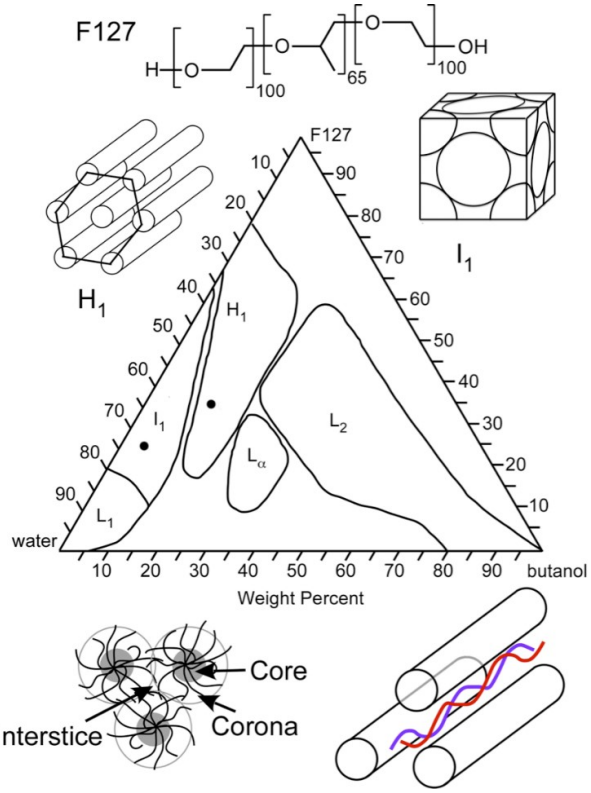

Figure 3.2 Chemical structure of Pluronic F127, and phase diagram for ternary F127: water: butanol mixtures, modified from ref 37. Shown are the normal hexagonal (H_1), isotropic (I_1), lamellar (L_α), and normal (L_1) and reverse (L_2) micellar regions. The filled circles appended to H_1 and I_1 depict the approximate compositions of samples investigated. The diagrams at the bottom depict the core, corona and interstitial regions of the F127 micelles and a model for elongated, aligned ds-DNA incorporated in the aqueous interstitial regions.[112] Reproduced with permission from Ref (112). Copyright 2014 American Chemical Society.

In preparation of the gels, Pluronic F127 was first weighed into a 5 mL glass vial. Buffer and butanol were then added. Afterwards, 70 µL of DNA and YOYO-1 stock solution was added

to the mixture. The stock solution was 500 mg/mL in DNA and 10 μM in YOYO-1. The vial was then repeatedly inverted and centrifuged for several hours over the course of two days to remove air bubbles. The gel was stored at 4 °C in the dark for at least two days prior to use. YOYO-1 dye intercalates into double stranded DNA,[108] allowing for its visualization by fluorescence methods. The final mixture incorporated DNA at 10 μg/mL, while YOYO-1 was present at a concentration of 1.2 μM. On average, these concentrations result in labeling of the DNA at a 13:1 ratio of base pairs to YOYO-1. The gel sample with microstructures in hexagonal region was highlighted in Chapter 4.

Table 3.1 F127 gel composition (in wt%).[112] Reproduced with permission from Ref (112). Copyright 2014 American Chemical Society.

	H_1	I_1
F127	34.8	26.4
Tris-HCl buffer	34.3	54.5
butanol	16.9	5.1
DNA&YOYO-1 soln	14.0	14.0

3.3 Synthesis of Organic Nanotubes

The synthesis of the organic nanotubes employed in Chapters 5 and 6 involves packing-directed self-assembly. The fundamentals of packing-directed assembly are described in Section 2.2.1. The monomer of the nanotubes is an asymmetric bolaamphiphile, *N*-(β-D-glucopyranosyl)-*N'*-(2-glycylglycylglycine-amideethyl)-icosane-diamide. **Figure 3.3** shows the structure of the

monomer. Synthesis of the nanotubes employed in this dissertation was performed by Mrs. Shinobu Ito.

The specific process is as follows: monomer solution (HCl salt, 10 mg, 13 μmol) is refluxed in Milli-Q water (10 mL) for 10 min. The hot solution is then gradually cooled to room temperature. NaOH standard solution (0.1 M, 200 μL) is added into the above solution. The resultant solution becomes turbid during nanotube formation. Due to the high pH, the nanotubes formed are expected to have deprotonated amino groups on the inner surface. The protonation state of the amino groups can be adjusted by addition of acids such as HCl to achieve protonated amino groups at pH 6-7. The resultant nanotubes are dried and stored in glass vials for future use. The final nanotubes applied in Chapters 5 and 6 have glucose groups on the outer surface and neutral deprotonated amino groups on the inner surface. The inner diameter is 10 nm, and outer diameter is 17 nm. More details about the nanotube characterization are given in Chapter 5.

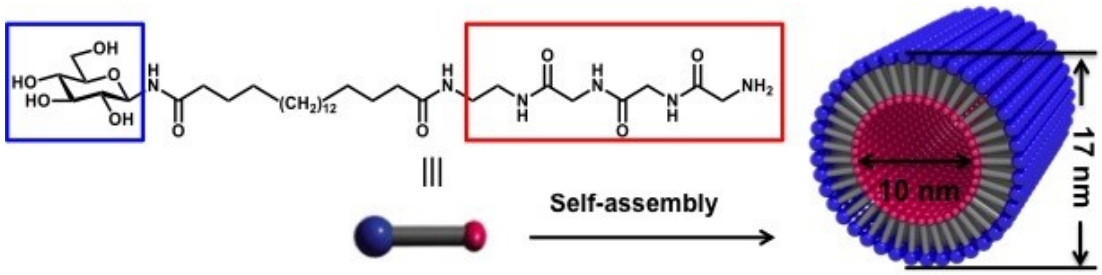

Figure 3.3 Bolaamphiphile monomer structure, and illustration of the molecular packing in the organic nanotubes.[22] Reproduced with permission from Ref (22). Copyright 2016 Royal Society of Chemistry.

3.4 Instrumentation

3.4.1 Two-dimensional (2D) Small Angle X-ray Scattering (SAXS)

SAXS is employed in Chapter 4 to characterize the order of the F127 hydrogel. SAXS affords information about the shape and size of macromolecules, pore sizes, and characteristic distances of partially ordered materials. In contrast to XRD, SAXS can be used to characterize molecular organization even in the presence of solvents, such as with micelles in a hydrogel form. Both methods offer information on average domain spacing and orientation over macroscopic sample regions and throughout the bulk materials.

In two dimensional (2D) SAXS, the morphology of the nanoscale structure is probed by irradiating the sample with an X-ray source and by simultaneously detecting the elastic scattering of the X-rays at very small angles ($2\theta < 10°$). From a 2D detector, both the order and orientation of the ordered structure can be obtained. The typical experimental setup for SAXS measurements is depicted in **Figure 3.4**. According to Bragg's law, the scattering angle (θ) is directly governed by the spacing/distance (d) between the periodic structures (domains or pores):

$$2d \sin\theta = n\lambda \qquad \text{(Eq. 3.1)}$$

where λ is the wavelength of the X-ray source (0.154 nm in this dissertation) and n is the order of the scattering peak. For periodically arranged morphologies, the scattered waves add constructively (n=1, 2, 3, …). The scattering peaks observed as a function of angle can be used to determine order/spacing of the included nanostructures, such as domains and pores. Thus, the scattered intensity offers valuable information on the periodicity and average morphology of the materials across the entire thickness for a macroscopic sample region.

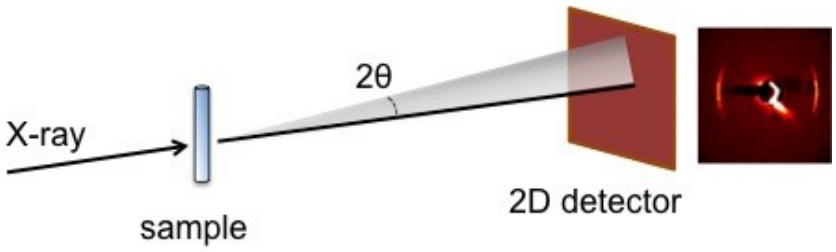

Figure 3.4 Schematic of a 2D-SAXS instrument with its major components: an X-ray source, sample and a 2D detector. The anisotropic pattern of scattering intensity indicates an ordered and aligned meso-structure of the sample.

Organizational information, such as the mesophase structural characteristics can also be obtained from SAXS. In **Figure 3.4**, the right image shows strong scattering peaks interpreted as scattering along the 100 direction of a hexagonal mesophase. Weaker peaks at other angles are also often observed. Taken together, these provide conclusive evidence of a hexagonal mesophase.

However, because of the broad illumination beam, X-ray data can only reveal averaged information of materials structure. Details about local heterogeneities cannot be obtained by SAXS/XRD.

3.4.2 Wide-field Fluorescence Microscopy

This section introduces wide-field fluorescence microscopy technique. Under high spatial resolution condition, it is possible to detect and image single molecules. By studying the dynamic behaviors of single molecules, the local heterogeneities of the materials can be revealed. All fluorescence imaging studies described in this dissertation were performed on a wide-field fluorescence microscope. A typical setup is shown in **Figure 3.5**. The system starts with a laser light source (488 or 514 nm), the light is first passed through appropriate optical components including optical filters and dichroic mirrors, and is then delivered to a high magnification and high numerical aperture (*NA*) objective lens (100X magnification, 1.49 *NA*) to excite the dye

molecules in the sample. An objective in high *NA* and magnification is very advantageous in fluorescence microscopy. A high *NA* objective enables the effective detection of weak fluorescence signal and provides for higher resolution. Higher resolution offers smaller detection area on the sample per pixel. This is especially essential in some particular microscopy techniques. For example, imaging-FCS requires detection of a small enough region on the sample surface to ensure the low concentration of the probe molecules, as described in Chapters 5 and 6. *NA* values differ from specific objectives. According to the definition of numerical aperture, $NA = nsin\,\theta$, where θ is the convergent angle in the medium light travels, *NA* can be large for a medium with larger *n* (refractive index of the medium in which the objective is working). For example, *n* of oil (1.52) is much larger than that of air (1.0). Thus, the objective that can work in oil medium would have a higher NA than the ones working in air. High magnification of the objective also facilitates the diffraction-limited detection of single molecule spots. After the laser excites the fluorophores in the sample, the fluorescence signal emitted by the sample is directed back through the same objective and finally detected by a sensitive charge-coupled device (CCD) camera. A beam splitter cube can be inserted into the detection path prior to the detector to obtain two-image channels. In Chapter 6, this beam splitter is used to obtain two videos simultaneously in two different emission wavelength ranges. More details about two-channel imaging are provided in Chapter 6. The CCD camera employed has built-in electron-multiplying (EM) gain capabilities and this enables detection of rapidly diffusing molecules. EM gain generates secondary electrons via impact ionization by applying high voltages between the electrodes, and thus significantly amplifies the

charge signal. With EM gain, the readout noise is effectively suppressed and the S/N ratio of the fluorescence images can be greatly increased.

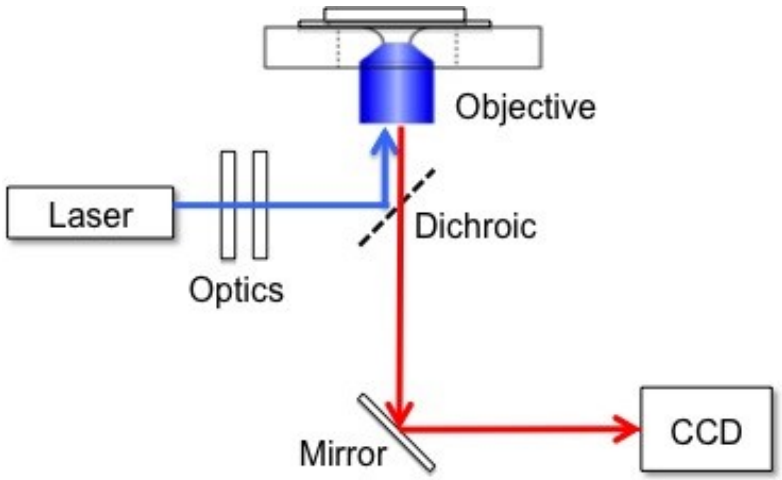

Figure 3.5 A scheme of an epi-fluorescence microscopy system for fluorescence imaging.

In wide-field microscopy, the sample is illuminated across a relatively large area (e.g. 32 μm x 32 μm in Chapter 4), compared to the size of a focused spot in a confocal microscope.[113] Thus, many fluorescent molecules can be detected simultaneously. Also, when coupled to a new generation CCD camera, which affords high sensitivity and high temporal resolution in video data, it allows for the detection of single molecule dynamics almost in real time. Many of the experiments in this dissertation were performed on optically thick samples for which out-of-focus sample regions could present challenges by producing high levels of background. As a means to help eliminate this background, while also simplifying the optical geometry, an epi-illumination configuration was employed in all studies described in this dissertation. In the epi-illumination mode, the fluorescence signal emitted from the sample is transmitted through the same objective, which is used to focus the illuminating light source. Owing to the reduced background and low excitation light allowed to the detector,[113] this illumination mode is more advantageous than the transmission microscopy configuration.

To achieve additional background reduction in thick samples, total internal reflection fluorescence (TIRF) mode was also employed in all experiments. This mode exploited the evanescent field produced immediately adjacent to the interface between two media having different refractive indices. Commonly, TIRF mode is employed at the interface between a glass slide and the sample, in which the refractive index of sample (n_s) is smaller than that of glass (n_g). When the incident angle is larger than the critical angle at this interface, light is totally reflected, as depicted in **Figure 3.6**. The critical angle (θ_c) can be derived from Snell's law:

$$\theta_c = \sin^{-1}(n_s/n_g) \quad \text{(Eq. 3.2)}$$

The produced standing electromagnetic evanescent field excites the fluorescent molecules in a thin slab at the interface. The penetration depth (d_p) can be estimated by the following equation:[114]

$$d_p = \lambda/4\pi\sqrt{n_g^2 sin^2\theta - n_s^2} \quad \text{(Eq. 3.3)}$$

where λ is the wavelength of the incident light, and θ is the incident angle. The penetration depth is typically ~200 nm.[115] Thus only the fluorescent molecules near the interface of the glass and sample are excited. Background fluorescence from the bulk sample can be significantly eliminated by using TIRF mode.

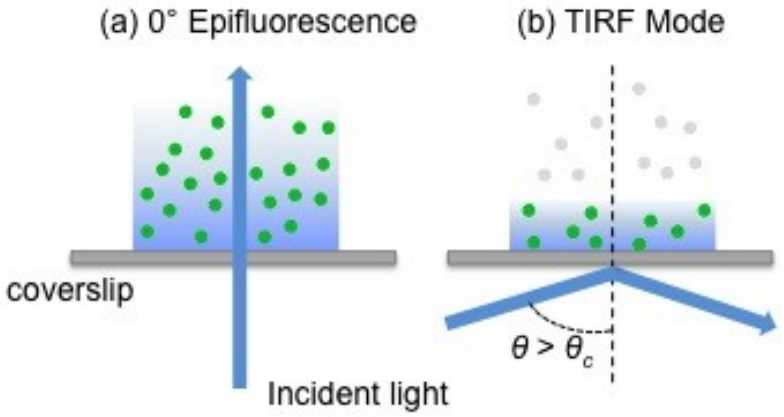

Figure 3.6 Schematic of (a) epi-fluorescence and (b) TIRF imaging mode.

3.5 Imaging-Fluorescence Correlation Spectroscopy (FCS)

3.5.1 Traditional Confocal FCS

FCS is a powerful method to detect molecule motion with high spatial and temporal resolution. In contrast to other fluorescence techniques, the parameter of interest is not the fluorescence intensity itself, but rather the spontaneous intensity fluctuations caused by molecule diffusion behaviors within the detection volume.

In traditional FCS, probe fluorescence is recorded by an avalanche photodiode (APD) from a single spot on the sample by point illumination. The diffusion of individual dye molecules in and out of the detection volume (**Figure 3.7a**) results in the observed fluorescence signal fluctuations. To ensure detection of individual molecule motions, FCS requires extremely small concentrations of the molecules present in the detection volume. The fluorescence signal from the small observation region is recorded over time, giving a time transient trace (**Figure 3.7b**). The time transient data is autocorrelated in time (**Figure 3.7c**) to extract information on the molecular diffusion processes underlying the fluctuations. The autocorrelation function basically measures the self-similarity of a time signal. The equation describing the autocorrelation function, $C(\tau)$, is written as follows:

$$C(\tau) = \frac{\langle i(t)i(t+\tau)\rangle}{\langle i(t)\rangle^2} - 1 \qquad \text{(Eq. 3.4)}$$

where $i(t)$ is the time transient data, $i(t + \tau)$ is the time transient shifted by a time lag, τ, and the brackets, $\langle\,\rangle$, indicate the time averaged value is calculated. The shape of the curve gives a hint of how fast the molecules diffuse and how many different components contribute to the diffusion behavior (e.g., one dimensional or a combination of one and two dimensional motion).

Quantitative information on parameters such as the diffusion coefficient of the molecule motion can be obtained by fitting of the autocorrelation curve with appropriate models.

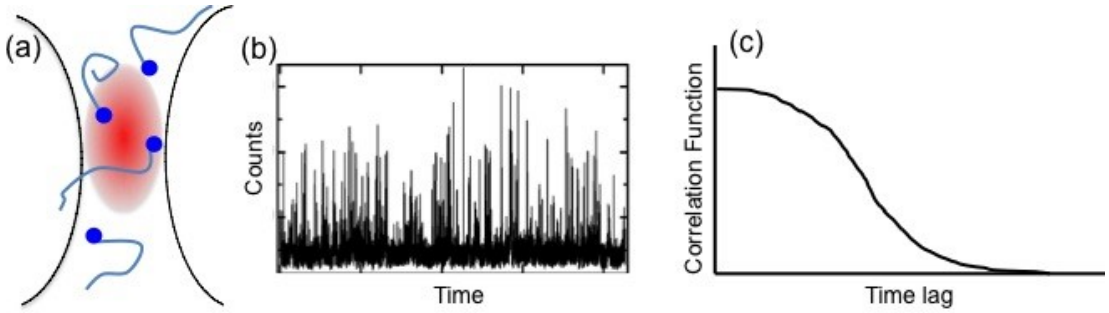

Figure 3.7 (a) Fluorescent molecules give emitted signal when diffusing across the detection volume; (b) Fluorescence fluctuations from the detection volume over time;[116] Adapted with permission from Ref (116). Copyright 2006 American Chemical Society. (c) Autocorrelation function calculated from (b) over time.

FCS provides access to the measurements of fast dynamics that cannot be easily detected by many other methods such as single molecule tracking[117,118] and fluorescence recovery after photobleaching (FRAP).[119] Although it offers high temporal and spatial resolution, it is not well suited for imaging of the diffusion dynamics in heterogeneous materials. For heterogeneous sample, time transients need to be recorded at each point in the image area, which would be very time-consuming.

3.5.2 Imaging-FCS

Imaging-FCS is a combination of fluorescence imaging with an autocorrelation analysis. It allows for many time transients to be collected simultaneously across a broad image area, greatly enhancing the data acquisition rate, albeit with some sacrifice in time resolution. A wide-field microscope is employed in imaging-FCS, while traditional FCS is conducted on a confocal microscope. EM-CCD cameras are needed for imaging-FCS in order to achieve high temporal

resolution. Imaging-FCS has also been shown to afford sub-diffraction-limited spatial resolution.[120] It has been applied in studies of measuring solution diffusion of lipid molecules in a planar lipid bilayers,[121,122] as well as diffusion of fluorescent polystyrene beads and small fluorescent molecule probes in highly viscous media.[123] The technique can also be adapted to TIRF mode to obtain lateral diffusion information near the glass-sample interface.[124]

Figure 3.8 depicts a typical data acquisition process in imaging-FCS. By limiting the acquisition region on the CCD to a subset of pixels (8x8 pixels in **Figure 3.8**), the readout is more rapid than reading the entire chip (the full image shown on the left in the figure), allowing fast rates capable of following fast diffusion. The location of the small interrogated region on the surface can be selected manually on the area of interest. After the long video is taken on the small region, one can select a smaller area digitally to obtain a time transient trace, for example, from a 2x2 or 4x4 pixel region, and extract diffusion information from the selected sub-pixels by autocorrelation of the time transient. However, it must be remembered that the selected pixel region needs to be small enough to maintain a low concentration of fluorophores in the detection region so that fluctuations can still be detected.

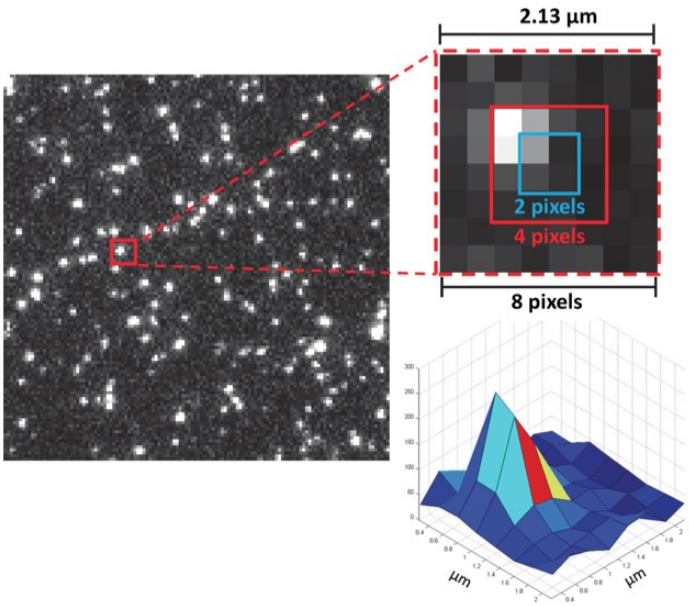

Figure 3.8 Imaging of DiI on C_{18}-modifed surface (30 ms acquisition time, 128 × 128 pixels). Expansion shows the imaging-FCS acquisition areas, and a surface plot below illustrates the fluorescence intensity profile for the imaged molecule over the 8 × 8 pixel area.[21] Reproduced with permission from Ref (21). Copyright 2014 American Chemical Society.

Imaging FCS is particularly well suited for investigations of heterogeneous samples, because many time transients can be acquired simultaneously for neighboring regions of a sample. In traditional FCS, individual transients would need to be acquired one at a time from neighboring sample regions to access the same data set. Such experiments would be time-consuming and would suffer from significant photobleaching of the dye molecules. Imaging FCS provides a more efficient way to explore fast diffusion with much less photobleaching effect on the sample.

Chapter 4 - Elongation, Alignment and Guided Electrophoretic Migration of ds-DNA in Flow-Aligned Hexagonal F127 Gels

Adapted with permission from The American Chemical Society. Published as: Hao Xu, Christopher J. Minter, Shinobu Nagasaka, Takashi Ito, Daniel A. Higgins, *J. Phys. Chem. B*, **2014**, 118 (15), pp 4151–4159.

4.1 Introduction

Rod-shaped biomolecules like ds-DNA are known to exhibit strong interactions with both thermotropic and lyotropic liquid crystal (LC) mesophases. These interactions are of significant fundamental interest and also have potential technological applications. For example, in work by Clark and coworkers,[125] shear-aligned films of calf thymus DNA were used to orient certain thermotropic LCs. The LC was found to align at oblique angles to the ds-DNA long axis in these studies. Chiral organization of achiral LC molecules was also found near the ds-DNA-coated surface. The inherent chirality of the ds-DNA and physical interactions of the LC molecules with the major and minor grooves were concluded to guide LC alignment. Schwartz et al.[126] also reported oblique alignment of thermotropic LC molecules in the presence of oriented, elongated ds-DNA. Interestingly, LC alignment parallel to the extension direction was observed for single stranded (ss)-DNA in these same studies. It was concluded that DNA-LC interactions might afford a simple optical means for discriminating between ss- and ds-DNA.

The mesogens in lyotropic LCs usually comprise much larger self-assembled structures (e.g., micelles) than in small-molecule thermotropic LCs and are therefore expected to interact

differently with biopolymers like ds-DNA. Lyotropic LCs may form spherical or cylindrical micelles or planar structures. Further self-organization leads to the assembly of cubic (isotropic), hexagonal or lamellar mesophases. As a result of possible unique interactions between DNA molecules and these organized, nanostructured materials,[127,128] lyotropic LC mesophases have long been investigated as alternative gel phases for DNA separations.[129-131] LC-DNA interactions in this case may lead to improved performance over random gel matrixes.[129-131] Further advantages include the ability to optimize a separation by simply changing the composition or temperature of the gel to alter its structure. Similar advantages have been claimed for lyotropic LC mesophases used in drug delivery,[36,132] and gene therapy.[133]

Pluronic F127 is one of many important lyotropic LC materials that have been investigated for use in the above applications. F127 is a tri-block copolymer comprised of a central poly(propylene oxide) block sandwiched between two poly(ethylene oxide) blocks, as described in Section 2.1. Ternary mixtures of water, F127 and an organic cosolvent such as butanol afford access to a broad range of nanostructures,[37] including cubic, hexagonal, and lamellar mesophases. A representative phase diagram for these materials is shown in **Figure 3.2**.

Rill and coworkers[129], Baba, et al.[131] and Chu, et al.[134] have all employed F127 gels in demonstrations of electrophoretic DNA separations. Each notes certain advantages of using F127 as the gel matrix, compared to more common gel media. However, full optimization of separations based on F127 will require greater knowledge of the interactions between the DNA molecules and the gel matrix. For example, it remains uncertain whether DNA becomes entangled in the micelles or if it is trapped between them, passing through in a linear fashion under the influence of an applied field. Both the Van Winkle[135] and Baba[131] groups have

explored these issues for cubic F127 mesophases. These researchers report imaging studies in which the motions of single dye-labeled DNA molecules migrating through F127 gels were recorded. While linear motion of the DNA molecules was observed under certain conditions,[131,135] there is some disagreement on the extent to which F127-DNA interactions govern DNA motions and on the mechanism of DNA transport through the gels.[136,137] In particular, the Åkerman group has reported that DNA does not enter the gel structure but rather migrates along grain boundaries at low fields;[137] while Van Winkle, et al.[135] report that the DNA can pass into and through the cubic F127 mesophase for relatively high gel concentrations at high field strengths. Although Chu and coworkers[134] have studied DNA electrophoresis in hexagonal F127 mesophases, no images of DNA motions in this mesophase have been published to date, to our knowledge. As a result, it remains unclear how the cylindrical F127 micelles may interact with the DNA molecules and guide or limit their conformations and motions. It is well known that these micelles interact strongly with small molecules, confining their diffusive motions to one dimension, at least on short time scales.[138-141]

In this chapter, the interactions between λ-DNA molecules and two different F127 gels prepared in the hexagonal and cubic regions of the ternary F127/butanol/buffer phase diagram are investigated. DNA-doped F127 gels are prepared and pumped into microfluidic optical cells for use in these studies. Wide field fluorescence video microscopy is used to obtain images of gel-entrapped DNA molecules doped with YOYO-1 dye, a well-known DNA intercalator.[108] Images are acquired both in the absence and presence of applied electric fields. The purpose of these investigations is to explore the extent to which the flow-aligned gel matrix may cause the alignment and elongation of the DNA, and guide its field-driven motions.[142] Emphasis is given to studies of the flow aligned hexagonal mesophase, because it is expected to play an important

role in defining these behaviors and has not yet been investigated in detail. Conductance anisotropy within the mesophases is also explored as a means to better understand the phenomena observed. The structure of the F127 mesophase and the flow alignment of the micelles are confirmed by SAXS.

4.2 Experimental Considerations

4.2.1 Materials

Pluronic F127 was purchased from Anatrace. The n-butanol (reagent grade) used in F127 gel preparation was obtained from Sigma Aldrich. YOYO-1 dye was purchased from Molecular Probes, while the λ-DNA was obtained from New England BioLabs. All were used as received. The procedures for preparation of DNA incorporated F127 gel were described in Section 3.2.

4.2.2 Microfluidic Chip Fabrication

The microfluidic device used in the present experiments consisted of a PDMS-based microfluidic channel affixed to a patterned ITO electrode. The device configuration is shown in **Figure 4.1a**. The PDMS monolith was prepared by casting uncured poly(dimethylsiloxane) (PDMS) onto a prefabricated glass mold. After the PDMS was cured, the monolith was removed and contacted to an indium-tin-oxide (ITO) coated glass coverslip (SPI Supplies). The PDMS monoliths were 1.5 mm in thickness, 2.5 cm in length, 1.2 cm in width. The microfluidic channel dimensions were 0.5 mm × 2.5 mm × 15 mm (depth × width × length) as defined by the glass mold. A 1 mm diameter biopsy punch was used to fabricate inlet and outlet holes at each end of the channel. The ITO coated coverslip was photolithographically patterned to allow for

application of an electric field to the F127 gels. The patterning process is diagrammed in **Figure 4.1b**. The ITO-coated coverslip was first cleaned with water, acetone and isopropanol and subsequently dried by heating at 60ºC on a hot plate. A layer of primer solution (MCC Primer 80/20) was then spin-coated on the coverslip surface, followed by a layer of positive tone photoresist (Shipley 1813); both were coated at 1500 rpm. The coated coverslip was next baked

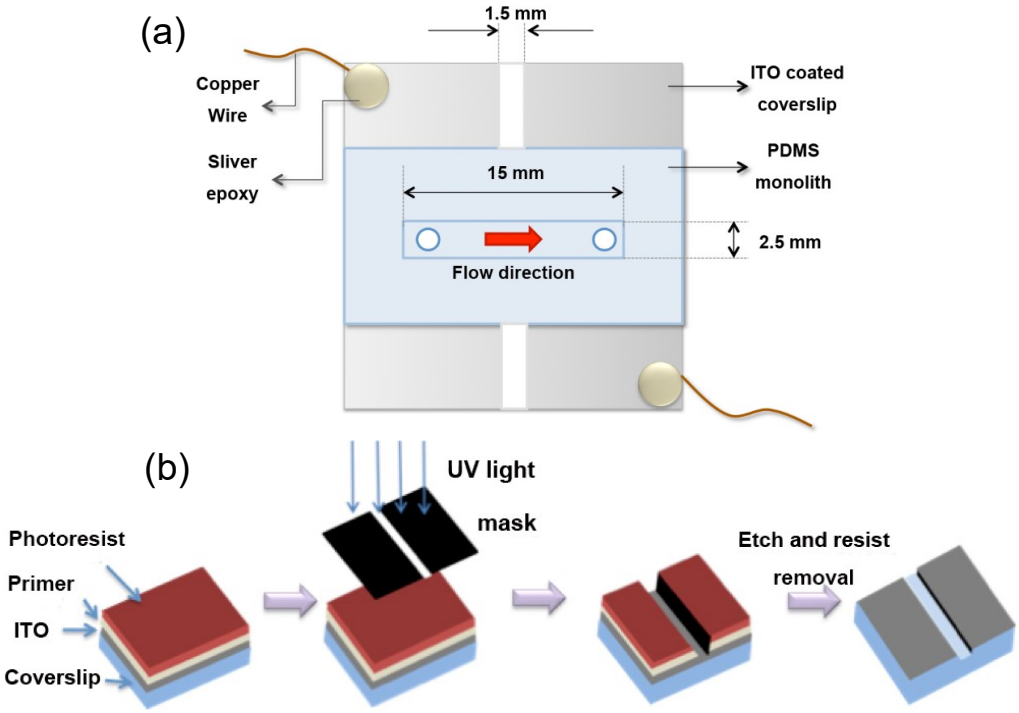

Figure 4.1 (a) The microfluidic device used in the experiments. (b) Photolithographic process used to pattern the ITO electrodes

at 105ºC for 15 min to remove residual solvents. The photoresist was patterned by exposure to UV light through a laser printed photomask. The exposed region was subsequently removed by rinsing in developer solution (Microposit 351 Developer). To harden and improve adhesion of the photoresist, the coverslip was next heated at 120ºC for 20 min. As a final step, the ITO was etched by immersing in an acidic solution of 4:2:1 $HCl:H_2O:HNO_3$. The resulting ITO pattern consisted of two rectangular conductive pads separated by a 1.5 mm wide gap. For application of an electric

field, the ITO electrodes were electrified by attaching copper wires to them using silver epoxy. The direction of the applied field was changed by simply orienting the microfluidic channel along different directions relative to the gap between the electrodes. In the configuration shown below, the flow direction and applied electric field are parallel to each other.

4.2.3 Flow Alignment of Gels

The microfluidic channels were filled with F127 by first drawing the gel into a glass capillary using a syringe pump. The capillary was then contacted to the channel inlet and the syringe pump reversed to load the channel. The flow velocity of the hexagonal and cubic gels were ~8 mm/min and ~6 mm/min, respectively. After filling, the inlet and outlet holes were immediately sealed using two-part five-minute epoxy.

4.2.4 2D SAXS Measurements

2D SAXS measurements were performed at the Characterization Facility at the University of Minnesota (Minneapolis, MN) using a SAXS instrument with a Rigaku 18 kW Cu source (λ= 1.54 Å) and a multiwire area detector. The sample to detector distance was 282.9 cm. SAXS samples were prepared by loading the F127 gels into 1 mm diameter thin-walled capillaries (10 μm wall thickness; Charles Supper Co.). After loading, the capillaries were sealed to prevent evaporation of the solvents.

4.2.5 Fluorescence Microscopy

Images of single DNA molecules entrapped in the F127 gels were acquired on an inverted epi-illumination microscope (Nikon TiE) that has been described previously in

detail.[143] Light from a blue diode laser (488 nm) was used to excite YOYO-1 fluorescence. TIRF mode was employed to minimize background fluorescence from deep within the gel and to facilitate detection of single DNA molecules. The images obtained are therefore limited to regions within ~200 nm of the gel-glass interface. In the majority of experiments, an oil immersion objective (Nikon Apo TIRF 100X, 1.49 numerical aperture) was used for sample illumination and for collection of the emitted fluorescence. The incident laser power was maintained at 1 mW. Fluorescence collected from the sample was directed through an appropriate dichroic mirror and bandpass filter to block residual source light. Fluorescence videos were acquired by detecting YOYO-1 fluorescence with a CCD camera (Andor iXon DU-897). Videos were acquired with 0.5 s exposure times, with sequential frames separated by a 1.5 s dark period. Each video was 200 frames in length. Measurements of molecule alignment, length and mobility were performed using the freely available ImageJ software. To induce migration of the DNA molecules, a square-wave AC voltage (±3.5V, 0.01 Hz) was applied across the microfluidic channel, using a CH Instruments, Inc. electrochemical analyzer.

4.2.6 Conductance Experiment

Conductance measurements were carried out using an YSI model 35 Conductance Meter. Prior to measuring the conductance of F127 gels, the response of the individual microfluidic cells was first calibrated by measuring the conductance of a series of KCl solutions (0.0005M, 0.001M, 0.003M, and 0.005M) for the different field directions. The conductance values for the hexagonal gels (0.1 M tris/HCl buffer) loaded into the same cells were subsequently measured and corrected for differences in exposed electrode area, using the KCl results. All measurements were made at room temperature (~23 ºC).

4.3 Results and Discussions

4.3.1 SAXS Characterization of F127 Alignment

Micelle organization and alignment in the F127 mesophases was investigated by 2D SAXS. **Figure 4.2a** (inset) shows a SAXS pattern from a representative DNA-doped hexagonal sample contained within a glass capillary. The capillary axis was oriented along the vertical direction on the figure. In this configuration, the strongest scattering was found in the plane perpendicular to the capillary axis. This observation is consistent with the presence of cylindrical micelles aligned parallel to the capillary axis and hence, along the original flow direction. The scattering intensity is also plotted as a function of 2θ in **Figure 4.2a**. The characteristic (100) peak of the hexagonal mesophase is located at $2\theta \approx 0.62^{o}$, giving a d-spacing of 14.2 nm. This indicates that the center-to-center distance between the micelle cores is 16.4 nm, based to the cross sectional structure of the F127 micelles.[37] Weak SAXS precluded similar measurements on the cubic mesophase. Comparison of SAXS data obtained in the presence and absence of DNA showed no clear differences, suggesting the dilute DNA employed has little effect on the average organization of the F127.

As a hydrophilic biopolymer, DNA is expected to preferentially partition to the aqueous interstices between the micelles. These regions are approximately triangular in shape and ~ 6 nm in height, in the hexagonal mesophase. Since the ds-DNA helix diameter is only 2 nm,[144] it is reasonable to expect that the DNA molecules may be found in the interstitial space, and that their conformations and motions may be influenced by the cylindrical micelle structure.

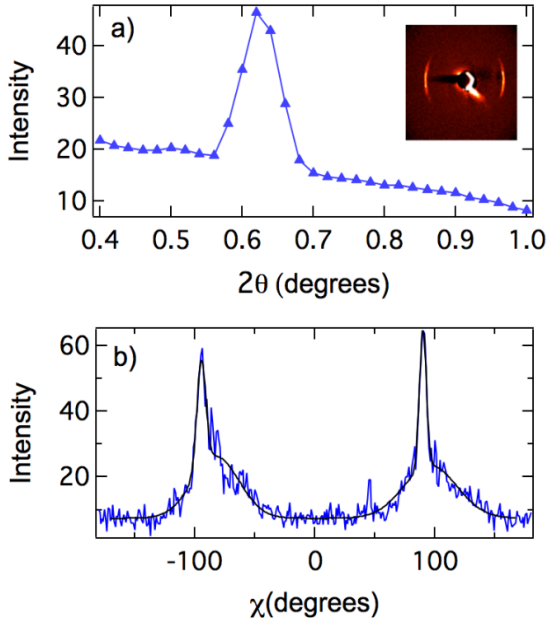

Figure 4.2 (a) X-ray scattering intensity as a function of scattering angle (2θ) derived from 2D SAXS pattern shown in the inset. (b) Scattering intensity as a function of azimuthal angle (χ), from the hexagonal mesophase. The black curve shows a double Gaussian fit to the data.

Figure 4.2b depicts the (100) scattering intensity for the hexagonal gel as a function of azimuthal angle, again demonstrating micelle alignment along the capillary axis (i.e., peaks near ±90°). The azimuthal dependence also appears to show two distinct levels of order, as reflected by the presence of both broad and narrow scattering distributions. To quantitatively describe the micelle order, these distributions were fit to a two-component Gaussian function. The Gaussian width, σ, in each case was used to determine the 2D order parameter <P> for each domain,[145] where:

$$\langle P \rangle = 2cos^2\sigma - 1 \qquad \text{(Eq. 4.1)}$$

For the data shown in **Figure 4.2b**, $\langle P \rangle = 0.99$ and 0.52 for the narrow and broad distributions, respectively. Data acquired from replicate gels reveal variable organizational order and domaining between samples. However, all depict similarly high levels of organizational order.

4.3.2 DNA Imaging Studies: Zero-Field Experiments

Figure 4.3 shows fluorescence images of YOYO-1 labeled DNA molecules dispersed in hexagonal and cubic F127 gels in the absence of an electric field. These images were acquired in both TIRF mode (**Figure 4.3a,b**) and from deep within the gel, under conventional illumination (**Figure 4.3c**). The latter was collected using a water immersion objective. A predominance of elongated DNA molecules aligned parallel to the flow direction (horizontal on the images) is found in the hexagonal mesophase, near the gel-glass interface (see **Figure 4.3a**). In the cubic mesophase (**Figure 4.3b**) the DNA molecules are not elongated to the same extent and appear to be randomly aligned or are present as coils. This difference reveals a strong dependence of DNA conformation and alignment on the structure of the supporting mesophase. The cylindrical micelles in the hexagonal mesophase likely play a role in both elongation and alignment of the DNA molecules along the flow direction. In contrast, the cubic mesophase presents an isotropic medium that interacts very differently with the DNA. The results in the cubic mesophase are consistent with previous reports in which F127-incorporated DNA molecules were present as coils or randomly aligned strands.[135,136]

In contrast to the clear alignment of elongated DNA molecules near the gel-glass interface, little evidence of DNA alignment along the flow direction was found in regions far from the gel-glass interface, as shown in **Figure 4.3c**. This image was acquired using a water immersion objective and represents observations made at > ~ 10 μm distances from the interface. The

dependence of DNA elongation and alignment on distance from the interface will be addressed further, below.

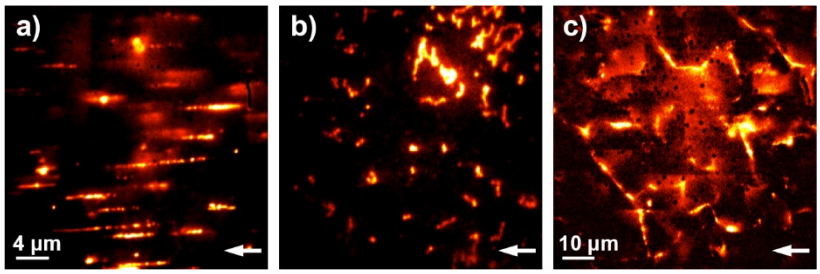

Figure 4.3 Representative wide-field fluorescence images of DNA molecules dispersed in the hexagonal mesophase (a) and the cubic mesophase (b) recorded in TIRF mode, and an image of DNA molecules in a bulk hexagonal gel (c) recorded by conventional wide-field illumination. These images depict the first frame of a 200-frame video and were acquired in the absence of an electric field. Solid arrows depict the flow direction during filling of the channel. The false image color depicts the intensity of YOYO-1 fluorescence. These images have been background subtracted. Scale bar in Fig 4.3(a,b): 4 µm, in Fig 4.3(c): 10 µm.

Elongation lengths and alignment angles for the DNA molecules were determined by manually selecting the individual molecules and measuring their end-to-end lengths and orientations on the images. **Figure 4.4** plots the distribution of molecular lengths for both the hexagonal and cubic mesophases, as observed in TIRF mode. The DNA length distribution in the hexagonal mesophase (**Figure 4.4a**) is peaked near 5 µm. The λ-DNA employed is 48,502 base pairs in length with a full contour length of 16.5 µm.[146] After staining by YOYO-1 dye, the contour length increases to ~ 19.3 µm.[147] Some of the DNA molecules approach these lengths (see **Figure 4.4a**) in the hexagonal mesophase. While some are also found to be longer than the full contour length (~ 24 µm), these are attributed to the overlapping of two DNA molecules in the images. The presence of butanol in the gels should not significantly alter the DNA conformation as collapse of

DNA to a globular conformation occurs in a narrow range near 40 wt% butanol in aqueous solution.[148]

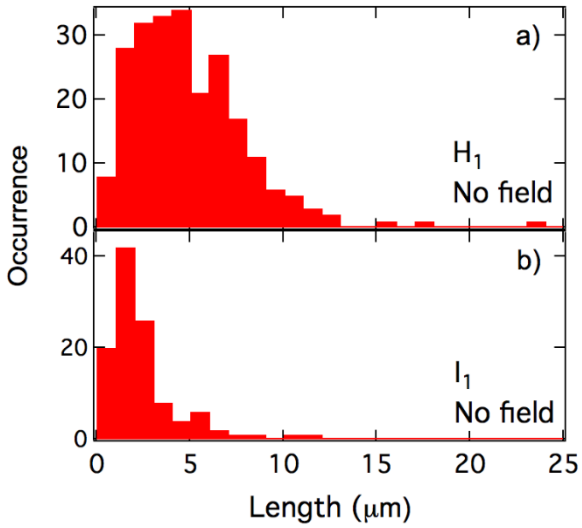

Figure 4.4 Histogram showing the DNA molecules elongation length (μm), in hexagonal (a), and cubic (b) mesophase, in the absence of an applied field.

Figure 4.4b shows the elongation of DNA molecules in the cubic mesophase. Because the DNA molecules are mostly bent or coiled in this case, the net length of each molecule along its longest dimension is reported. The peak in the histogram is located at 1.6 μm, which is only ~ 50% larger than the value expected from the radius of gyration of λ-DNA (~ 500 nm)[149,150] in an isotropic matrix and similar to the mean end-to-end distance (1.4 μm) expected for a wormlike chain.[142] Thus, without the guiding interactions of the cylindrical micelles in the hexagonal mesophase, the DNA molecules in the cubic mesophase appear to take on a random coil conformation.

As shown in **Figure 4.3a**, the DNA molecules near the glass-gel interface align mostly along the horizontal direction in the hexagonal mesophase. A histogram quantitatively showing

the alignment angles for DNA molecules in the near-surface region in the absence of field are given in **Figure 4.5**. These data were compiled from measurements on ~ 200 molecules observed in multiple videos of three different samples. It shows strong alignment of the DNA molecules parallel to the original flow direction (0°), and parallel to the cylindrical micelles.

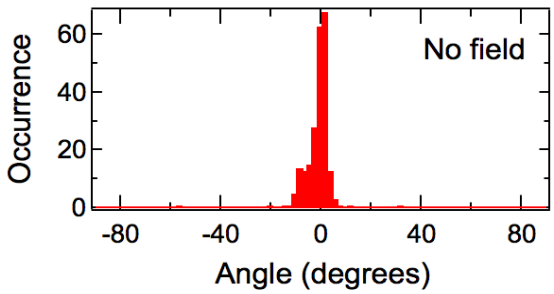

Figure 4.5 Histogram of alignment angles of DNA molecules in the hexagonal mesophase, in the absence of an applied field. The X-axis plots alignment relative to the expected direction (0°).

4.3.3 Mechanism of Flow-Aligned DNA Behavior in Hexagonal Mesophase

Two phenomena are believed to be important in elongation and alignment of the DNA found in the interfacial regions of the hexagonal F127 gel. First, as suggested by the dependence of DNA alignment on distance from the interface (**Figure 4.3**), shear forces active during filling of the microfluidic channel likely play a significant role. Photographs of the leading edge of the gel within the channel are shown in **Figure 4.6**. These reveal that the flow profile is not parabolic and very steep near the interface. In fact, F127 gels are known to exhibit shear thinning.[151] However, it appears the macroscopic flow profile is not the most important factor, as these photographs suggest a strong velocity gradient exists over distances of ~ 100 μm. In contrast, the data in **Figures 4.3a,c** suggest elongation and alignment occurs only at distances << ~ 10 μm from the interface. It is known that PEO-based polymers, including F127, form adsorbed layers a few nanometers in thickness on glass surfaces.[152] This adsorbed F127

comprises a stagnant layer at the interface. Entrapment of one end of a DNA molecule in this adsorbed, structured layer and the other in the nearby flowing gel may therefore be the cause of its initial elongation and alignment. Alternatively, one end of each molecule could adsorb to the underlying glass surface through defects in the stagnant F127 layer.

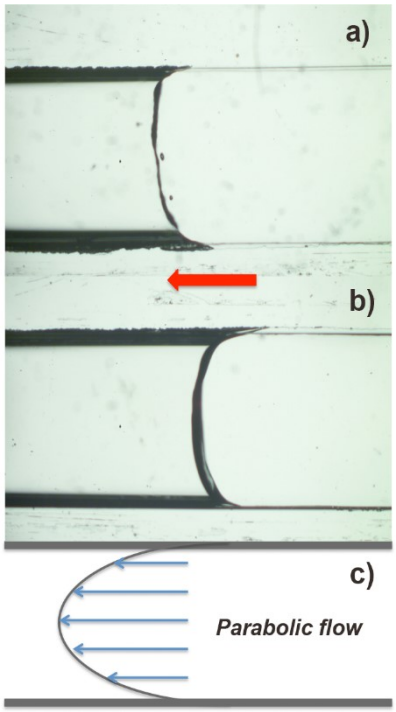

Figure 4.6 Flow profile of gels in the hexagonal (a) and cubic (b) mesophases in the microfluidic channel. A theoretical parabolic flow profile (c) is shown for comparison. The red arrow depicts the flow direction of the gel. The width of each channel is 2.5 mm.

Deeper within the gel, the DNA molecules appear to reside in 'cracks' that form at domain boundaries such as has been described in previous reports on cubic F127 materials.[135,137] Note that the 2D SAXS data is consistent with good alignment of the hexagonal mesophase throughout the gel. Hence, misaligned DNA observed far from the gel-glass interface is unlikely to be caused by gel disorder. Rather, it is likely alignment does not occur in these

regions because the different gel domains move at nearly identical velocities during channel filling.

While shear forces are clearly important in producing aligned, elongated DNA in the hexagonal F127 gels, these forces dissipate long before the images are acquired. Thus, a second mechanism must prevent the elongated DNA from subsequently relaxing to random coils. As is now well-known, DNA molecules confined within cylindrical nanopores become elongated as the pore diameter approaches the persistence length (~ 50 nm for ds-DNA) of the polymer.[146] In the present materials, the aqueous interstices in F127 gels are believed to behave as soft 'pores'. Our SAXS data, along with knowledge of the gel structure, indicate that the interstitial space between adjacent cylindrical micelles is nominally triangular in shape and ~ 6 nm height. Thus, this system would appear to fall in the Odijk regime,[153] in which the DNA persistence length is much larger than the pore diameter. Several groups have confirmed the Odijk theory for ds-DNA within nanochannels formed in fused silica and PDMS.[154,155] The nanochannels in these experiments had widths of 30-400 nm. They found the DNA had elongated to ~ 80% of its contour length in the 30 nm wide nanochannels. In the present materials, the elongation length (**Figure 4.4a**) is ~ 26% of the contour length, suggesting that the confining nanochannels are actually much wider than the interstitial regions. The elongation lengths observed are consistent with an effective 'pore' diameter of ~ 160 nm, placing this system in the Gauss-de Gennes regime,[156] where the pore diameter is more than twice the persistence length.[146] In this case, the elongated DNA would comprise aligned anisometric blobs.[156] These blobs may be manifested in the videos obtained as bright spots along the image of each DNA molecule (see **Figure 4.3a**). The DNA molecules must distort the F127 mesophase to some extent to achieve this conformation, as has also been noted by Chu and coworkers.[134] While it is possible the full

length of each DNA could be adsorbed to the surface,[157,158] preventing its relaxation, this typically requires chemically modified cationic surfaces and is therefore discounted as a possibility. Furthermore, as shown below, many of the elongated DNA molecules migrate under the influence of an electric field, which is inconsistent with their attachment to the surface. It is concluded that the observed extent of elongation represents at least a transient condition where the energetics of DNA elongation and mesophase distortion are balanced.

Comparison of the data in **Figures 4.3a,b**, provides additional evidence that the micelle structure must play a role in at least maintaining DNA elongation and alignment. A strong velocity gradient is expected at the gel-glass interface for both the hexagonal and cubic mesophases, yet clear evidence of elongation and alignment is only found in the former. The absence of aligned DNA in the cubic mesophase suggests that anisotropy in the interfacial F127 layer may be important in producing DNA alignment in the hexagonal mesophase. Alternatively, any elongated molecules in the cubic mesophase may have simply relaxed to random coils prior to imaging. Unfortunately, experimental limitations prevent imaging of these samples during or immediately after channel filling. It is concluded that flow-induced alignment and elongation of the DNA in the hexagonal mesophase likely result from both shear forces active at the gel-glass interface during channel filling, and the anisotropic structure of the F127 mesophase, which prevents conformational relaxation of the DNA.

4.3.4 DNA Video Studies: Field Dependence of Drift Velocity

Further evidence of strong interactions between the DNA molecules and F127 micelles was obtained by investigating DNA mobility under the influence of an applied electric field. Here, the flow aligned F127 gels were exposed to electric fields aligned at 0°, 45° and 90° to

the flow direction. A square waveform (± 3.5 V) was applied across the samples such that the electric field reverses direction every 50 s (i.e., every 25 frames). Wide field fluorescence videos of the DNA motions were acquired throughout these experiments.

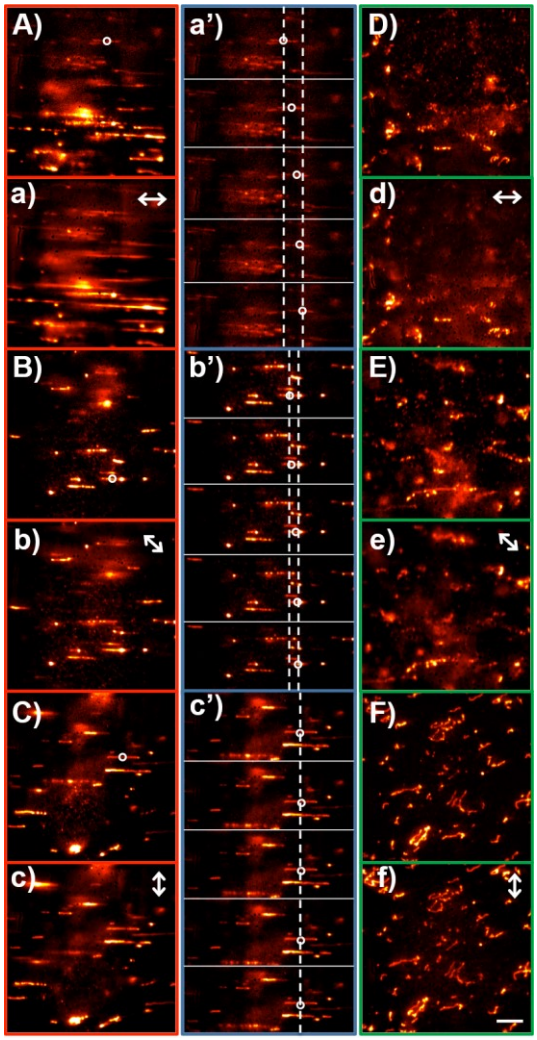

Figure 4.7 Fluorescence images of YOYO-1 labeled DNA molecules in hexagonal F127 (left and center columns) and cubic F127 (right column) migrating under the influence of electric fields applied along different directions (double ended arrows). Images labeled with uppercase letters depict the first frame of the field cycle while those labeled in lowercase show images compiled from the whole movies, which were comprised of 4 field cycles. The images in the center column depict the center-of-mass motions of each marked molecule (open circles) during the first half field cycle. The dashed vertical lines mark the distance traveled by each molecule. These images have been background subtracted. Scale bar: 5 µm.

Figure 4.7 shows representative images depicting the DNA motions. The panels labeled with uppercase letters show the first frame acquired under the influence of a field. The images labeled with the lowercase letters show a compilation of all frames acquired along the entire movie. The latter were obtained using the 'z-project' command in the ImageJ software package. Field driven motions of the DNA molecules in the hexagonal mesophase are best demonstrated by the center column of images in **Figure 4.7**. These show a sequence of five video frames for each of the three field directions. The frames shown were obtained during the first half of the first field cycle and represent frames 1, 6, 12, 18, 24 of the videos. The appended vertical dashed lines show the maximum center-of-mass displacements for a representative DNA molecule in each sequence, as designated by the open circles. Clear evidence of field-driven motions is seldom observed in the cubic mesophase.

The data shown **Figure 4.7**, and the associated videos, demonstrate that DNA mobility is strongly dependent upon mesophase structure (hexagonal vs. cubic). They also reveal a strong dependence on the direction of the electric field with respect to the flow alignment direction, for the hexagonal mesophase. In **Figure 4.7 (A-a'),** when the field direction is parallel to the flow direction, the elongated DNA molecules move relatively rapidly along the horizontal direction, parallel to the cylindrical F127 micelles. In **Figure 4.7 (B-b'),** where the applied field is at ~ 45^{o} to the flow alignment direction, the elongated DNA molecules are again observed to move along the horizontal direction, rather than parallel to the applied field. Importantly, the migration velocity is also smaller than in **Figure 4.7 (A-a')**. These data indicate DNA motions are strongly guided by the mesophase structure. The data shown in **Figures 4.7 (C-c')** reveal little or no field-

driven motion of the DNA molecules in any direction when the field is applied perpendicular to the flow direction.

Some elongated DNA molecules were also found to show no detectable motions under the influence of the applied field. These molecules may interact strongly (e.g., through hydrogen bonding) with either the adsorbed F127 layer at the channel surface, or with the glass surface itself. Likewise, little or no motion was observed for coiled DNA molecules.

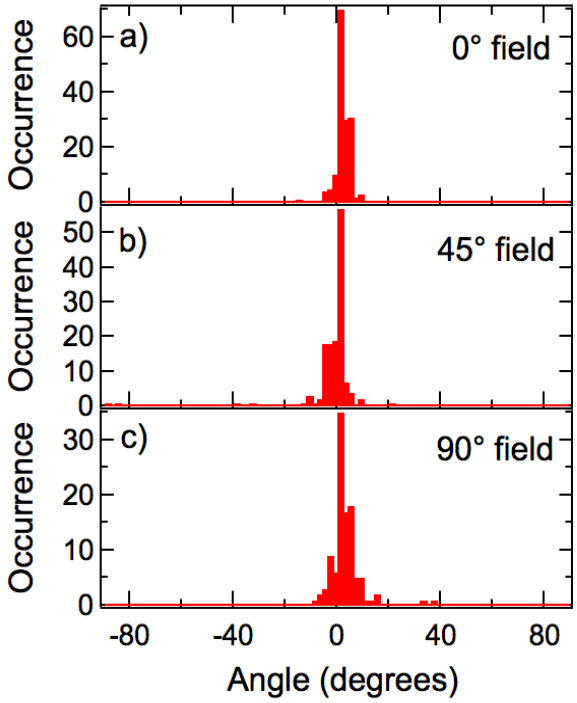

Figure 4.8 Histograms of DNA alignment angles in the hexagonal mesophase, for applied fields at 0° (a), 45° (b), and 90° (c) relative to the flow alignment direction.

The alignment angles of the DNA molecules in hexagonal mesophase were quantitatively measured for three different field directions. **Figures 4.8a-c** show these data. The peak of each histogram closely corresponds to the flow alignment direction, regardless of the field direction, showing that the DNA molecules are predominately aligned by the flow process alone. While the

Åkerman[137] and Chu[134] groups have shown that electrophoretic motions of F127-gel encapsulated DNA lead to its elongation and alignment, the lack of motion observed in directions other than the original flow direction prevent such effects from being observed in the present studies.

In the cubic mesophase (**Figure 4.7 D,d** to **F,f**), the DNA molecules are once again found to be present as coils or randomly aligned strands. In contrast to the hexagonal mesophase, little or no field-induced motion of the DNA was observed, regardless of the field direction. Previous studies by Van Winkle[135] and Åkerman[137] observed DNA migration through cubic F127 mesophases under similar, though not identical, conditions. They did not report observation of immobile DNA coils, likely because their DNA was electrophoretically loaded into the gels, rather than being incorporated at the time of preparation, as is the case here. Direct incorporation of the DNA in the gel may lead to its entrapment in or entanglement with the micelle structure, limiting its mobility. Alternatively, it may be adsorbed to the substrate surface.

To quantitatively assess the field-driven motions of the DNA molecules, the electrophoretic drift velocities, v_d, of the individual DNA molecules parallel to micelle alignment were also determined. **Figure 4.9** plots these values. Specifically, for each field direction (0°, 45º, 90°), 6-10 molecules were randomly selected from different movies and sample gels. The center-of-mass (x) of a DNA molecule was first determined by locating the two ends of the molecule and finding its center position from the average value. A set of data points (x_1, t_1), (x_2, t_2), …, (x_m, t_m) at times $t_m = m\tau$ were obtained for each molecule,[135] where m is the frame number, and τ is the time difference between adjacent frames. Next, the center-of-mass displacement, Δx, was calculated between pairs of frames separated by $\Delta t = n\tau$ time units, where n = 1, 2, 3, …. The average displacement, $\overline{\Delta x}$, for several molecules was then determined for each n and plotted vs Δt. The slope of this plot yields the drift velocity directly. This calculation was performed

along the flow alignment direction, and obtained from 6, 7, and 6 molecules for 0°, 45° and 90° fields, respectively. The results (**Figure 4.9**) show a strong dependence on the field direction, consistent with confinement of the DNA motions to the micelle alignment direction.

The drift velocity is related to the electrophoretic mobility, μ_p, along the micelle alignment direction by the following equation:

$$v_d = \mu_p |E| cos\theta \qquad \text{(Eq. 4.2)}$$

where |E| is the magnitude of the applied field, and θ is the angle between the field and flow directions. It may initially be assumed that the DNA moves freely along the interstitial space while experiencing negligible interactions with the confining micelles. In this case, the electrophoretic mobility along the alignment direction is expected to be constant, regardless of the field direction. The drift velocity along the micelles should then scale as $\cos\theta$ and its value for the 45° field should be ~ 71% of that for the parallel (0°) field. Interestingly, the drift velocity measured for the 45° field is found to be 54% of that for the parallel field, suggesting that the electrophoretic mobility along the flow direction is not constant. Mobility values of 62 ± 10 $\mu m^2/V{\cdot}s$ and 47 ± 8 $\mu m^2/V{\cdot}s$ are obtained for 0° and 45° fields, respectively. One possible explanation for this observation is that the DNA molecules may interact strongly with the micelle coronas, leading to increased frictional drag on the DNA as the field angle increases.

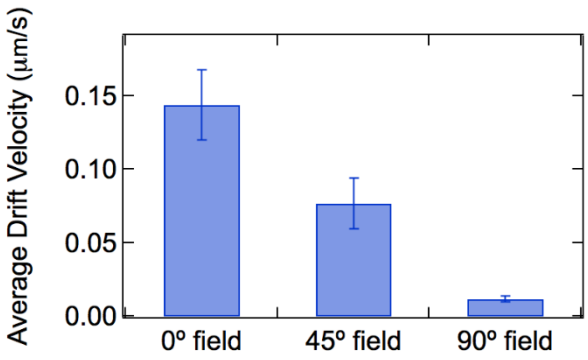

Figure 4.9 Average drift velocity of DNA molecules parallel to the aligned cylindrical micelles in the hexagonal mesophase as a function of field direction. The error bars represent the standard error of the mean value in each case.

4.3.5 Conductance Measurements

The above results show that the hexagonal F127 mesophase produces strongly anisotropic migration of the DNA molecules. This anisotropy may result from a difference in the electric field strength for different field directions (i.e., dielectric anisotropy). It may also reflect general anisotropy in ionic mobility within the hexagonal gel. That is, the DNA motions may be restricted by limitations to the motions of any/all ions in general, rather than by physical confinement of the DNA itself. To explore such possibilities, the conductivity of the F127 gels was also measured as a function of field direction.

Prior to making conductivity measurements on the DNA-loaded gels, the conductivities of standard aqueous KCl solutions were first measured. These measurements allowed for correction of variations in the data due to changes in the exposed electrode area for the different cell geometries employed as a function of field direction. Afterwards, the hexagonal F127 gels were immediately loaded into the same microfluidic channels for measurements of their conductivities. These latter results are shown in **Figure 4.10**.

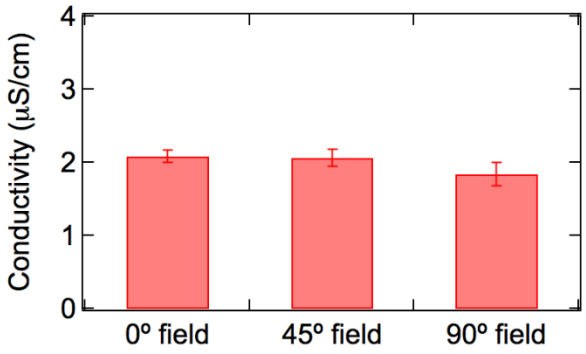

Figure 4.10 Conductivity of hexagonal F127 gels for 0°, 45°, and 90° fields. The error bars represent the standard error of the mean value in each case.

According to these data, F127 gel conductivity is almost invariant with field direction. This demonstrates that the dielectric anisotropy of the gel is very small and also that small ions can move freely through the organized gel structure, regardless of the direction of their motions. In contrast, the mobilities of the DNA molecules in the hexagonal mesophase (see **Figure 4.9**) were found to be strongly anisotropic, with their average mobility under the influence of a parallel field ~ 36 fold larger than that for the perpendicular field. These results show that limitation of the DNA motions is most likely due to physical interactions of the large DNA molecules with the micelles comprising the hexagonal F127 mesophase.

4.4 Conclusions

In this chapter we have investigated the interactions between λ-DNA molecules and the micelles comprising F127 gels prepared in the hexagonal and cubic regions of the ternary F127/butanol/buffer phase diagram. Flow injection of the DNA-loaded gels into microfluidic channels led to elongation and alignment of the DNA near the gel-glass interface in the case of

hexagonal gels, while the DNA was found to concentrate in 'cracks' formed between domain boundaries in these same gels, far from the interface. In the cubic mesophase, the DNA was present largely as coils and randomly aligned strands. These observations were attributed to shear alignment and elongation of the near-surface DNA in the hexagonal mesophase brought about by the steep flow profile that appears at the gel-glass interface during filling of the microfluidic channel. Confinement of the DNA within the (expanded) aqueous interstitial regions formed between the cylindrical F127 micelles very likely contributes to the conformational stability of the aligned, elongated DNA molecules within the gel. DNA mobility in the presence of applied electric fields was also investigated. Strongly anisotropic motions were observed, with the DNA molecules migrating most easily along the flow alignment direction, parallel to the cylindrical micelles comprising the organized gel. Little or no motion of the DNA was observed when the field was applied perpendicular to the alignment direction in the hexagonal gels. The strongly anisotropic and gel-dependent motions of the DNA molecules demonstrate that they strongly interact with and are guided by the micelle structures in the F127 gels. These results provide a better understanding of molecular interactions between DNA and the mesogens comprising lyotropic liquid crystal mesophases. Enhanced knowledge of these interactions promises to lead to improved applications of these materials in drug delivery and chemical separations.

4.5 Contributions of Authors

Christopher Minter first explored DNA elongation in F127 gels in our labs during the summer of 2011. Shinobu Nagasaka helped with preparation of buffer and DNA solutions.

Daniel Higgins and Takashi Ito guided the research and were instrumental in preparing the work for publication.

Chapter 5 - Imaging Fluorescence Correlation Spectroscopy Studies of Dye Diffusion in Self-Assembled Organic Nanotubes

Adapted with permission from The American Chemical Society. Published as: Hao Xu, Shinobu Nagasaka, Naohiro Kameta, Mitsutoshi Masuda, Takashi Ito, Daniel A. Higgins, *Phys. Chem. Chem. Phys*., **2016**,18, 16766-16774.

5.1 Introduction

Self-assembled organic nanotubes have been prepared from a variety of materials, including proteins, peptides, synthetic and natural lipids, and synthetic organic amphiphiles.[75,84,159] Synthetic nanotubes have attracted particular interest because they afford access to tailor-made materials with hydrophobic, hydrophilic and/or biocompatible outer surfaces, uniform tubular morphologies and internal nanospaces of controllable dimensions and surface chemistries. These attributes make them suitable for use in a wide variety of applications, including as nanopipettes,[160] nanocontainers for biomacromolecules[67] and as vehicles for drug delivery.[98,161,162]

A unique subset of synthetic organic nanotubes is those derived from bolaamphiphile surfactants.[67] Unlike many surfactant assemblies, bolaamphiphile-based materials afford nanotubes with differently functionalized (and functionalizable)[66] hydrophilic internal and external surfaces that can be used to encapsulate and transport water-soluble molecules into aqueous biological environments. Kameta and coworkers have recently synthesized bolaamphiphile-based nanotubes incorporating amine groups on their internal surfaces and sugars on their external

surfaces.[67] The sugars improve nanotube biocompatibility, while the amine terminated internal surfaces provide the means to load and immobilize molecules within the nanotubes, as well as allowing for them to be released in response to some stimulus.[68,163] Release of encapsulated molecules into the surrounding medium relies upon, among other factors, their diffusion within the nanotubes.[164,165] An in-depth understanding of mass transport rates and mechanisms within organic nanotubes is therefore critical to the development of materials for controlled release applications.

Molecular diffusion within nanoscale pores and microdomains can be explored by a number of different optical imaging and spectroscopic methods, including SMT,[17,18] FRAP,[119,166,167] fluorescence resonance energy transfer (FRET) imaging,[66] confocal FCS[167] and imaging-FCS.[120] SMT has been used previously to investigate the effects of surfactant nanostructures on molecular diffusion within one dimensional (1D) lyotropic liquid crystal mesophases.[138] However, SMT is difficult to implement in the characterization of single organic nanotubes, because of the low dye concentrations required. FRAP is a common ensemble method that has recently been used to probe diffusion in the 1D poly(ethylene oxide) microdomains of phase separated poly(ethylene oxide)-polystyrene block copolymer films.[119] Unfortunately, FRAP is best suited to investigations of diffusion over long distances (i.e., > 10 μm) and is thus challenging to implement in studies of single relatively short nanotubes. FCS has provided valuable information on diffusion rates and adsorption/desorption kinetics in studies of organic nanotubes.[167] However, FCS would require several long time transients be recorded sequentially at a number of different positions along each nanotube. Imaging-FCS instead allows for many time transients to be collected simultaneously across a broad image area, and thus avoids frequent photobleaching to different positions on one

tube. Autocorrelation of the time transient obtained at each image pixel is then used to determine the time scale for diffusion.

In this chapter, imaging-FCS was employed to investigate both the rate and mechanism of diffusion for SRB dye molecules doped into bolaamphiphile-based self-assembled organic nanotubes. The SRB dye served as a model for anionic molecules that might be loaded into and released from these nanotubes in drug delivery applications. The dye-doped nanotubes were dispersed on glass substrates so that individual nanotubes could be located and imaged one at a time, using wide-field fluorescence video microscopy. They were immersed in buffer solution to mobilize the dye molecules within the nanotubes. Wide-field video data acquired from isolated nanotubes were collected, autocorrelated on a pixel-by-pixel basis, and the autocorrelation decays fit to an appropriate model to determine the apparent diffusion coefficient of the dye as a function of position along each tube. Both the ionic strength and the pH of the buffer solution were varied as a means to modulate any coulombic interactions between the SRB molecules and the charged inner surfaces of the nanotubes. The results showed that SRB diffusion was governed by more than the random thermal motions of Fickian diffusion, with coulombic interactions playing an integral role in slowing mass transport of the dye. The results of this study will aid in the development of bolaamphiphile-based nanotubes for use in controlled drug release applications by providing a better understanding of the factors governing the rates and mechanisms of mass transport within the nanotubes.

5.2 Experimental Section

5.2.1 Materials

The organic nanotubes were formed from an asymmetric bolaamphiphile monomer: *N*-(*β*-D-Glucopyranosyl)-*N′*-(2-glycylglycylglycine-amideethyl)-icosane-diamide. The structure of the monomer is shown in **Figure 3.3**. The resultant nanotubes consist of a single layer of bolaamphiphiles, in which hydrogen bonds strongly hold the polyglycine-II-type network together.[93] The inner and outer surfaces of the nanotubes are terminated with ammonia and glucose headgroups, respectively (see **Figure 3.3**). Section 3.3 described the synthesis procedures of this organic nanotube.

To prepare the tube samples for imaging experiments, the nanotubes were dispersed on glass coverslips. In this process, an aqueous solution of nanotubes (0.1 mg/mL) was drop cast on a plasma-cleaned glass coverslip, and the water was allowed to evaporate. The coverslip was subsequently rinsed with water to remove any loosely adsorbed nanotubes and blown dry with nitrogen. The nanotubes remaining on the surface were then doped with SRB (Acros Organics) for fluorescence imaging. The structure of SRB is shown in **Figure 5.1c**. The nanotubes were dyed by depositing 200 μL of 120 μM SRB in aqueous solution over the coverslip. This solution was allowed to sit in contact with the nanotubes for a period of 2 h. The coverslip was then rinsed with 18 MΩ·cm water and blown dry with nitrogen. This final rinsing step removed SRB molecules loosely bound to the exterior of the nanotubes and to the coverslip surface.[167]

Fluorescence videos of the nanotubes were acquired under buffer solution. To maintain contact between the buffer and nanotube samples, a rectangular PDMS well was fabricated and placed over the coverslip. The PDMS well was filled with any one of a series of phosphate buffered saline (PBS) solutions (Aldrich), immediately prior to the imaging experiments. The

PDMS well was then covered with a PDMS slab to prevent solution evaporation. The PBS solutions employed were buffers of pH 6.4, 7.4 and 8.4. Each was prepared in four different ionic strengths (1.73 mM, 17.3 mM, 173 mM and 520 mM).

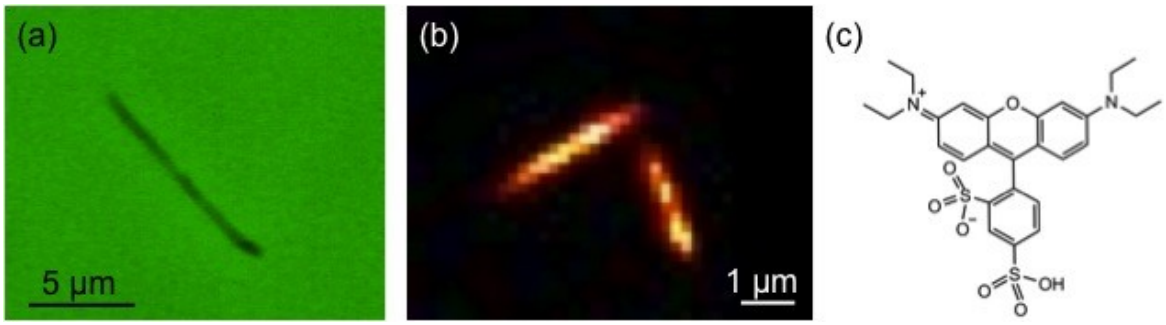

Figure 5.1 (a) Optical phase contrast image of one nanotube. (b) Wide-field fluorescence image of sulforhodamine B stained nanotubes. Different nanotubes are shown in panels a and b. (c) Structure of sulforhodamine B.

5.2.2 Fluorescence Microscopy

Images of individual dye-doped nanotubes were acquired on an inverted epi-illumination microscope (Nikon TiE) that has been described previously in detail.[143] Briefly, light from an argon ion laser (514 nm) was used to excite SRB fluorescence. TIRF mode was employed to minimize background fluorescence from bulk solution. An oil immersion objective (Nikon Apo TIRF 100×, 1.49 numerical aperture) was used for sample illumination and for collection of the emitted fluorescence. The incident laser power was maintained at 0.8 mW in all experiments. This power level afforded a sufficient signal-to-noise ratio while also reducing photobleaching of the dye molecules. Fluorescence collected from the sample was directed through an appropriate dichroic mirror and bandpass filter (580/40) to block residual source light. Fluorescence videos were acquired by detecting SRB fluorescence with an EM-CCD camera (Andor iXon DU-897). Videos were acquired with 2 ms exposure time, and ~ 6 ms cycle time. The EM gain was set to 30, the readout rate to 10 MHz, and 3x3 pixel binning was employed. Each video was 25,000

frames in length. The lateral dimension of the detection volume was estimated from a convolution of the pixel size (0.1875 μm) with the Gaussian point spread function width (0.240 μm) of the microscope.[168] In this case, the largest diffusion coefficients that can be measured by this method are ~ 5 $\mu m^2/s$. This is significantly smaller than the ~ 470 $\mu m^2/s$ expected for SRB diffusion in bulk solution.[169] Therefore, only the relatively slow diffusion of SRB molecules interacting with the nanotubes can be probed in these studies.

The excitation region in the images covered a relatively large lateral area of 32 μm × 32 μm. Images were initially recorded from the full field of view to identify and locate individual nanotubes. Much smaller regions (~ 2.5 μm x 2.5 μm) showing individual nanotubes were then selected and video data acquired. The videos were subsequently loaded into a program written in the LabVIEW (National Instruments) programming environment. This software subtracted the image background and calculated the temporal autocorrelation function at each pixel, across the final 20,000 video frames. The autocorrelation decays were subsequently fit to an appropriate model that included contributions from dye diffusion and photobleaching (see below).

5.3 Results and Discussions

5.3.1 Wide-Field Fluorescence Images

The nanotubes studied in this chapter are 10 nm in inner diameter, 3.5 nm in wall thickness and several micrometers in length.[93] **Figure 5.1a** shows an optical phase contrast image obtained from one nanotube. While this tube appears to be slightly bent at one end, only straight nanotubes were selected for further investigation. **Figure 5.1b** shows a wide-field fluorescence image obtained from a pair of SRB stained nanotubes. As with all fluorescence videos employed below,

this image was acquired in TIRF mode in order to minimize background fluorescence from bulk solution. The nanotubes can be clearly distinguished above the background, owing to SRB staining. These tubes are ~ 2 μm in length, close to the average length of the full population of nanotubes examined in these studies. Videos were typically recorded of individual nanotubes.

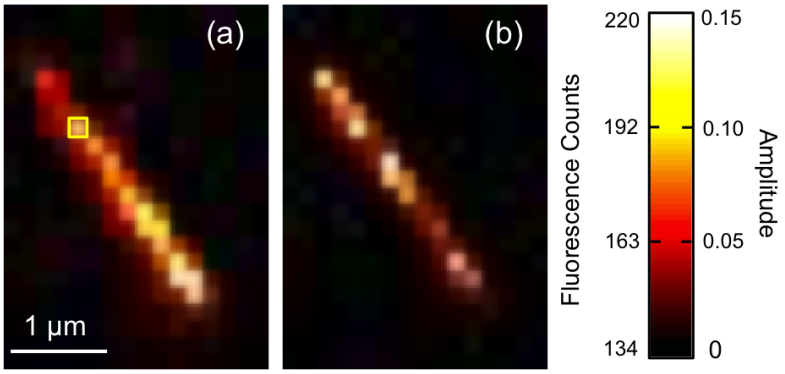

Figure 5.2 Representative wide-field fluorescence video data from an organic nanotube in PBS buffer solution at pH 7.4 and 0.1mM ionic strength. The video is presented as an image and was obtained by averaging the fluorescence across 20,000 frames. (b) Image showing the fitted autocorrelation decay amplitude for each pixel in (a). Scale bars show the fluorescence counts (in 2 ms, left) and amplitude values (right) for panels (a) and (b), respectively.

Representative video data from a single nanotube is shown in **Figure 5.2**. This image was obtained by averaging the fluorescence across 20,000 video frames at each pixel. The apparent width of the nanotube shown is ~ 375 nm (full-width-at-half-maximum). Its width is much larger than the expected value of 17 nm because of the limited spatial resolution (~ 240 nm) of the optical imaging system. Neither the image shown in **Figure 5.2a**, nor the original video data show clear evidence of fluorescent spots produced by individual SRB molecules. This is likely due to the presence of several dye molecules within the nanotube. Because of their brightness, the individual nanotubes can be clearly differentiated from much weaker fluorescent spots found in the surrounding regions. These background spots may reflect the presence of very short nanotubes, nanotube fragments, or residual unassociated SRB molecules.

The fluorescence intensity observed along a single nanotube can potentially provide information on the uniformity of nanotube doping. Indeed, the average fluorescence intensity (averaged across 20,000 video frames) was found to vary along the length of the nanotube shown in **Figure 5.2**. Such spatial variations in average fluorescence were observed in virtually every nanotube imaged in these studies. This observation suggests that the tubes were not uniformly doped with SRB. However, no clear trend in the position dependence of the signal levels could be identified, as discussed later. It is believed the non-uniform fluorescence of the nanotubes may reflect the relatively low concentration (quasi single molecule levels) of dye found within the nanotubes. Furthermore, the fluorescence intensity of local regions along the individual tubes was observed to vary in time. These variations are consistent with time dependent variations in the local concentration of dye and are attributable to Brownian-like motion of the SRB molecules within the nanotubes.

5.3.2 Imaging Fluorescence Correlation Spectroscopy

The apparent diffusion coefficients for SRB molecules diffusing within the nanotubes were determined by autocorrelating the fluorescence video data on a pixel-by-pixel basis and fitting the autocorrelation decays obtained to an appropriate model. **Figure 5.3a** plots a representative time transient obtained from the pixel highlighted by the yellow box in **Figure 5.2a**. The fluorescence spikes shown in the time transient depict signal fluctuations attributable to diffusion of individual SRB molecules in and out of the detection volume along the nanotube. It is the mean time scale of these signal fluctuations that gives a measure of the apparent diffusion coefficient for the SRB molecules. However, the signal level also gradually decays in time due to the inevitable photobleaching of the limited number of dye molecules found within the nanotube. The

background fluorescence from regions surrounding the nanotube also exhibits a similar bleaching decay. It should be noted that no dye was added to the buffer solution and hence, the bleaching was essentially permanent.

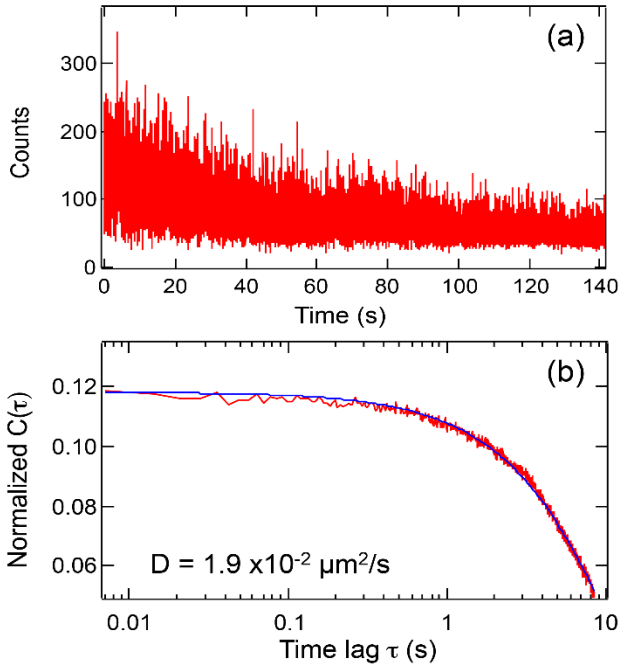

Figure 5.3 (a) Representative time transient from the one pixel in Figure 5.2a (yellow box); (b) autocorrelation function (red line) derived from the data in (a), using Eq. 3.4 and its fit to Eq. 5.1 (blue line).

Individual time transients were obtained from each pixel along the tube in each video. The time transient data were then correlated by autocorrelation function. The function was described in Section 3.5.1. **Figure 5.3b** shows the autocorrelation function obtained from the time trace in **Figure 5.3a** (red data points). While the autocorrelation function was obtained from the full 20,000 frames, it is only plotted out to τ = 1200 frames, due to the limited signal averaging that occurs at longer lag times.[170-172] The autocorrelation functions obtained from the nanotubes commonly incorporate two decay components: one attributable to mass transport of the SRB

molecules and the other to SRB bleaching. As is readily apparent from the data shown in **Figure 5.3**, fluctuations due to diffusion occur on a several second time scale, while the bleaching decay occurs over several tens of seconds. Because of the approximately 10-fold difference in these two time scales, the contributions of diffusion and bleaching can readily be distinguished.

In selecting an appropriate model for use in fitting of the autocorrelation functions, it was noted that the nanotube inner diameter (~ 10 nm)[93] is very small compared to its length (> 2 μm). Therefore, SRB diffusion within the tube is expected to be strongly confined to 1D. Furthermore, no evidence of long adsorption events, such as have been observed previously for diffusion of charged dyes near other charged surfaces,[116,173] was found in any of the videos acquired in the present studies. The absence of anomalously long adsorption events suggests that a model for Fickian diffusion may be appropriate. The equation employed for fitting of the data thus included components for both 1D diffusion and photobleaching, and is given by:[174]

$$C(\tau) = \frac{A}{\sqrt{1+\frac{\tau D}{\sigma^2}}} \times \frac{(\exp[k(T-\tau)]-1)}{k(T-\tau)} \qquad \text{(Eq. 5.1)}$$

Here, D represents the apparent diffusion coefficient of the SRB molecules within the tube, A is the amplitude of the autocorrelation decay, σ^2 is the squared radius of the detection region (σ ~ 0.310 μm), k represents the bleaching decay rate constant, and T is the total length of the video in time. While all parameters could be obtained by fitting the individual autocorrelation decays, the bleaching time constant was instead obtained by separately fitting the decay of the background fluorescence in each video. The bleaching decay constant obtained was then employed in Eq. 5.1 as a constant parameter, with the only adjustable parameters being A and D.

Figure 5.2b shows the amplitude data obtained by fitting the autocorrelation function from each image pixel in **Figure 5.2a**. The zero delay point ($\tau = 0$) was not included in the fitting

process as its value includes contributions from significant uncorrelated noise. Brighter pixels indicate larger amplitudes. The amplitude image reveals the tube location and width with improved, sub-diffraction-limited spatial resolution,[120] which can be observed as a narrowing of the tube image between **Figures 5.2a** and **5.2b**.

Concentration Dependence. The autocorrelation decay amplitude is often used as a means to estimate the concentration of diffusing molecules in a sample and is expected to be inversely dependent upon the concentration of diffusing dye molecules.[175] However, as noted in previous work,[176] a more complicated concentration dependence occurs in the presence of significant background. In this case, the autocorrelation amplitude actually increases with increasing dye concentration, passes through a maximum, and subsequently decreases. In order to fully understand the conditions under which the present data were acquired, autocorrelation results were obtained as a function of dye concentration in the nanotubes, which was varied by changing the SRB concentration in the loading solution from 10 μM to 70 mM. It was found that the autocorrelation amplitude initially rises with dye concentration, peaks at ~ 140 μM and later decreases, as expected.[176] The decrease in the autocorrelation amplitude at higher dye concentrations is consistent with assignment of the signal fluctuations to single molecule diffusion phenomena. Because of this rather complex concentration dependence, no conclusions on the uniformity of dye loading could be drawn from the autocorrelation amplitude data. However, these results were used instead to select an optimum dye concentration of 120 μM for loading of the nanotubes, as it provides relatively high amplitudes while avoiding the possibility for SRB dimerization.[177] All subsequent experiments were performed on nanotubes loaded at this concentration.

Apparent Diffusion Coefficients. The autocorrelation fits also provide valuable data on the apparent diffusion coefficient, *D*, at each image pixel along each nanotube (see Eq. 5.1). The *D* value obtained from the pixel highlighted in **Figure 5.2a** is 1.9×10^{-2} $\mu m^2/s$, based on the fit shown in **Figure 5.3b**. The *D* values obtained along the full length of this same nanotube are similar and are best depicted as an image constructed from the *D* values. While an apparent *D*

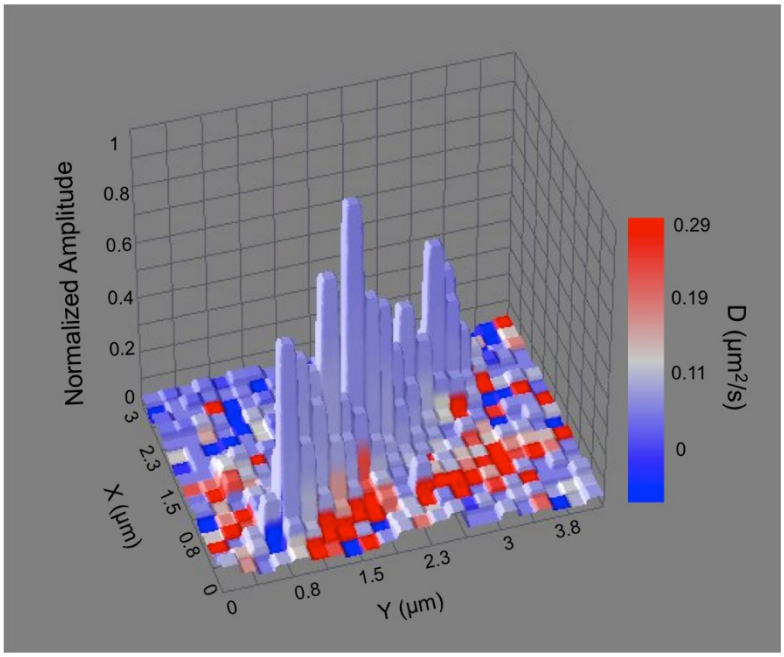

Figure 5.4 3D surface plot showing a composite image of the nanotube in Figure 5.2 with the normalized autocorrelation amplitude shown as height, and the measured diffusion coefficient depicted by the color scale.

value is obtained from every image pixel, many of the pixels have little or no signal and so their *D* values are often meaningless. The former is found off the tube, over background regions, while the values obtained from the nanotube itself are useful. To better depict regions where meaningful *D* values were obtained, a composite 3D image was prepared, as shown in **Figure 5.4**. This image depicts the autocorrelation amplitude as height and the measured *D* value by the image color. The amplitudes are very close to zero off the tube, where little or no dye diffusion is detected. Likewise,

the *D* values obtained off the tube vary substantially from pixel to pixel because they are dominated by noise. In contrast, the *D* values obtained along the tube are largely invariant with position, as depicted by the uniform image color along the nanotube axis. This image suggests the *D* values are qualitatively similar along the tube length.

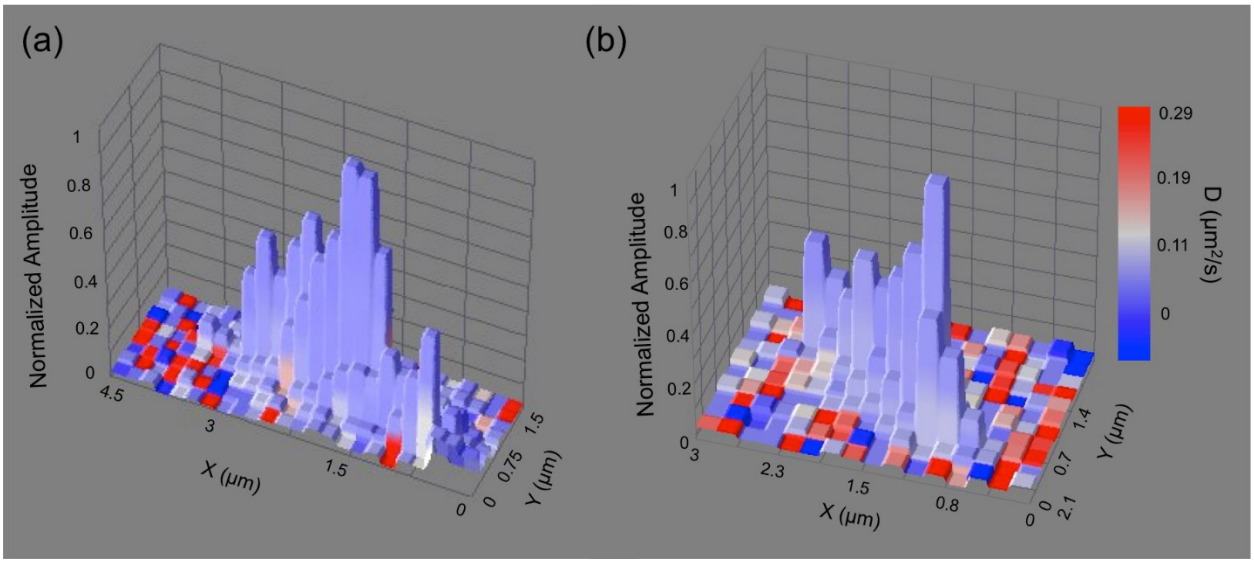

Figure 5.5 3D surface plots of two additional nanotubes, showing the normalized autocorrelation amplitude as height, with the measured diffusion coefficient depicted by the color scale.

Figure 5.5 depicts two additional 3D surface plots showing composite images of the autocorrelation amplitude and diffusion coefficient data. Similar to **Figure 5.4**, the amplitudes are approximately zero off the nanotube and the diffusion coefficients obtained are dominated by noise in these regions. Meaningful diffusion coefficient data are only obtained from the nanotubes themselves, for which the uniform color depicts only relatively small variations in these values.

Along with the data shown in **Figure 5.4**, these three composite images of the nanotubes reveal the consistency of the diffusion coefficient data obtained from different tubes. These same data also demonstrate that there is no clear position dependence in the concentration of diffusing SRB molecules in the nanotubes.

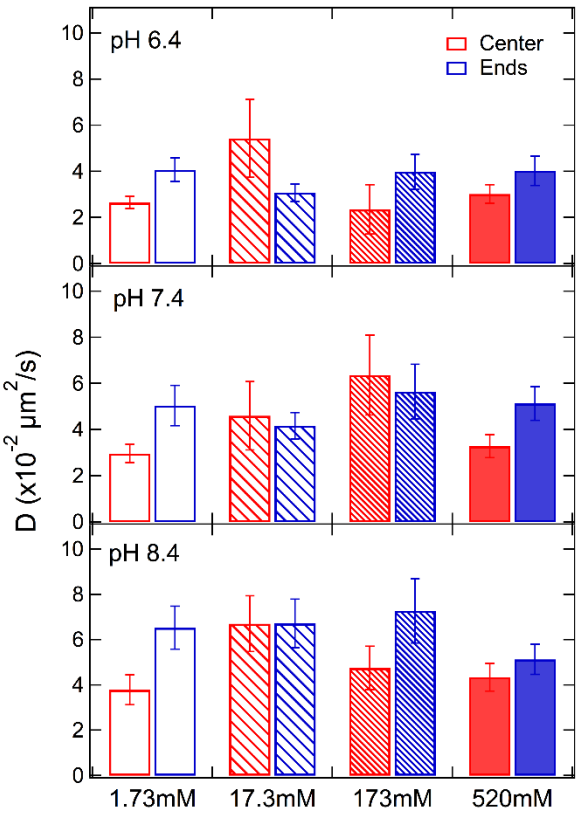

Figure 5.6 Averaged apparent diffusion coefficients obtained at tube center and ends in varied pH and ionic strength conditions. Error bars represent the standard deviation on the mean.

Further analysis of position dependence of SRB diffusion along the nanotubes was conducted by averaging the SRB diffusion coefficients for the nanotube centers and ends. Each nanotube was equally divided into three regions (two ends and the center) along the long axis of the tube. The mean diffusion coefficient for each region was then obtained by averaging the *D* values of each pixel in one region. **Figure 5.6** plots the diffusion coefficients obtained from center and ends of the nanotubes under different pH and ionic strength conditions. No clear trends are observed in

these data. Statistically, only five cases out of twelve show differences in D at > 80% confidence, while opposite trends are frequently observed between the tube ends and center. It is concluded that the diffusion dynamics are relatively homogeneous along the full length of the tubes. This result contrasts with those obtained from lipid nanotubes in which the rate of diffusion was found to be faster at the tube ends and slower in the nanotube center.[167] In the latter, the observed differences were attributed to heterogeneous packing of lipids. The results obtained from our present nanotubes are consistent with a homogeneous nanotube structure and homogeneous filling of the nanotubes with aqueous solution (at least on resolvable length scales).

Averages of the data obtained along the full length of the aforementioned nanotubes (**Figures 5.4**, **5.5a** and **5.5b**) yield D values of 1.6×10^{-2} $\mu m^2/s$, 5.6×10^{-2} $\mu m^2/s$ and 1.9×10^{-2} $\mu m^2/s$, respectively. These values are all substantially smaller than the diffusion coefficient of SRB in bulk solution, which has been reported to be 470 $\mu m^2/s$.[169] It is possible that coulombic interactions between the anionic dye molecules and the cationic inner surfaces of the nanotubes could lead to rapid, reversible adsorption of dye to these surfaces, slowing its apparent diffusive motions. The difference between the bulk and apparent nanotube D values could also be the result of an increase in the viscosity of the solution inside the nanotubes. The D values should then scale inversely with the local viscosity, as defined by the Stokes-Einstein relation. However, the 10^4-fold reduction in D is too large to be explained by an increase in the viscosity of the water filling the nanotubes. Alternatively, the organic phase of the nanotube walls may provide the high viscosity environment suggested by the small D values. In this case, the SRB molecules would need to partition from the aqueous phase into the walls of the nanotubes. This possibility may be discounted because the octanol-water partition coefficient (K_{ow}) for SRB is ~ 0.0095,[178] indicating that the dye is very polar and most likely confined to the aqueous phase inside the nanotubes. While it has been

demonstrated that water confined within organic nanotubes having glucose moieties on their inner surfaces exhibits a 20% decrease in polarity compared to bulk water,[179] this effect is deemed insufficient to dramatically enhance partitioning of the SRB into the nanotube walls. As with many organic dyes, SRB may aggregate in aqueous solution, altering its physical size and reducing its rate of diffusion. While SRB dimers have been reported to form at cationic surfaces,[180] such species would be immobilized inside the nanotubes and would not contribute to the measured *D* values. SRB aggregates in aqueous solution have only been found under relatively extreme (i.e. high salt content) conditions that are far different from those of the present experiments.[177] It is concluded that coulombic interactions between the dye and nanotube inner surface are the most likely cause of slow SRB diffusion.

It should be noted that SRB diffusion is also slower than might be expected from prior literature results. For example, the diffusion of green fluorescent protein (GFP) has previously been investigated inside similar organic nanotubes by FRET methods.[181] In this case, the average diffusion coefficient was found to be 0.36 $\mu m^2/s$ at pH 6.8, approximately 7-fold larger than the *D* values measured for SRB. This apparent discrepancy may reflect differences in experimental details: GFP is surrounded by stabilizing agents such as glycerol (20 wt%), and thus its interactions with the cationic sites on the nanotube inner surface are suppressed, while SRB is expected to interact more strongly with the nanotube. The possible role played by coulombic interactions in limiting SRB diffusion is the focus of the remainder of this chapter.

5.3.3 Ionic Strength Dependence of SRB Diffusion

The role played by coulombic interactions in governing mass transport of the SRB molecules can be explored by altering the ionic strength of the aqueous solution filling the nanotubes. Higher

ionic strengths will lead to narrower electrical double layers (i.e. shorter Debye lengths) at the nanotube surfaces. These conditions will better screen any coulombic interactions between the anionic dye and cationic sites on the nanotube surfaces, and are expected to lead to an increase in the apparent rate of SRB diffusion.

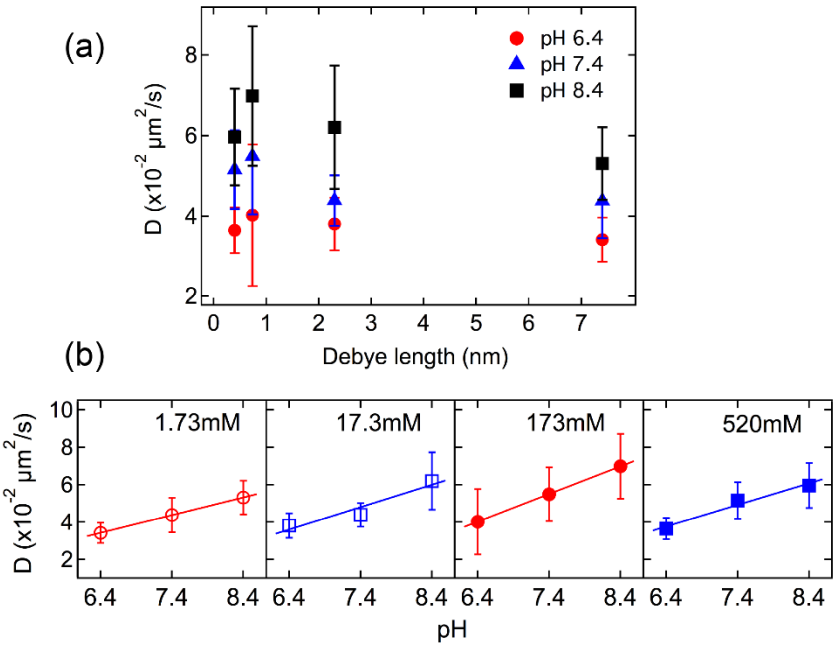

Figure 5.7 Average apparent diffusion coefficients for SRB as a function of Debye length (a) and buffer pH (b). Error bars are standard errors on the mean. The solid lines fitted to the data in (b) have been added only as a means to better depict the trends in the data.

The average SRB diffusion coefficients obtained from several different nanotubes are plotted as a function of Debye length in **Figure 5.7**. These data were acquired by averaging across the entire length of each tube and then averaging the individual tube data. The data shown are for ionic strengths of 1.73 mM, 17.3 mM, 173 mM and 520 mM, at three different pH values. The pH dependence of the data is discussed below. In all cases, the diffusion coefficients showed similar trends, with *D* increasing as the Debye length decreased from 7.4 nm to 0.74 nm (i.e., with increasing ionic strength). The *D* values subsequently decreased as the Debye length decreased to

0.4 nm. It is noteworthy that the electric double layers from opposite surfaces inside the nanotubes overlap when the Debye length is as large as 7.4 nm. Under this condition, relatively little screening of the dye and nanotube surface charges occurs and relatively strong dye-surface interactions are expected. As the ionic strength increases and the Debye length becomes shorter, the apparent SRB diffusion coefficient initially increases, consistent with increased coulombic screening. The decrease in the apparent SRB diffusion coefficient at the highest ionic strength is suggestive of a change in the nature of the physical interactions governing SRB motion. This latter observation might be explained by a 'salting out' of SRB at the highest ionic strength, leading to an abrupt increase in the strength of the relevant dye-surface interactions.

5.3.4 pH Dependence of SRB Diffusion

While the dependence of the apparent SRB diffusion coefficient on solution ionic strength is consistent with a slowing of dye motion caused by coulombic interactions between the dye and nanotube surface, it does not necessarily confirm a dependence on surface charge. Such a dependence is best demonstrated by monitoring SRB diffusion under different surface charge conditions. The surface charge was readily altered by changing the pH of the buffer solution filling the nanotubes. The pK_a of the ammonium groups on similar nanotubes (having the same headgroups but thinner hydrophobic walls) has been determined to be 7.27.[68] As the solution pH increases above 7.27, the density of ammonium ions on the inner nanotube surface will decrease, while lower pH values will lead to an increase in surface charge density. In the present studies, buffers having pH values of 6.4, 7.4 and 8.4 were employed to explore a range of surface charge conditions. It is noteworthy that the pK_a of the highly acidic sulfonic groups on the SRB dye is <

1.5.[178] Therefore, the SRB molecules will remain negatively charged across the range of pH values investigated.

Table 5.1 Summary of the mean apparent diffusion coefficients (x10^{-2} μm^2/s) with standard errors on the mean at each solution pH and ionic strength investigated. The number of nanotubes characterized in each case is given in parentheses.

	pH 6.4	pH 7.4	pH 8.4
1.73mM	3.4 ± 0.6 (11)	4.4 ± 0.9 (9)	5.3 ± 0.9 (6)
17.3mM	3.8 ± 0.7 (7)	4.4 ± 0.6 (12)	6.2 ± 1.5 (10)
173mM	4.0 ± 1.8 (7)	5.5 ± 1.5 (10)	7.0 ± 1.7 (5)
520mM	3.7 ± 0.6 (10)	5.2 ± 1.0 (10)	6.0 ± 1.2 (17)

Figure 5.7b plots the average apparent SRB diffusion coefficients as a function of pH for the four different ionic strengths. The numerical values used in construction of **Figure 5.7** are given in **Table 5.1**. Each set of data reveals a clear trend towards higher *D* with increasing buffer pH. At pH 6.4, the amine groups on the inner nanotube surfaces should be almost fully (~ 90%) protonated, while at pH 7.4 and 8.4, the expected degree of protonation decreases substantially (~ 43% and ~ 7%, respectively).[68] The results in **Figure 5.7b** therefore demonstrate a clear surface charge dependence in the apparent *D* values, consistent with an important role for coulombic interactions in governing mass transport.

It should be noted that the simple calculations presented above suggest that the surface charge density varies by more than an order of magnitude for the range of solution pH values investigated, while the observed *D* values change by only a factor of two. This apparent discrepancy has several possible origins. First, coulombic interactions may represent only one of several phenomena leading to slow dye diffusion, with pH independent phenomena also playing a role. For example, an increase in solution viscosity inside the nanotubes could also contribute to the slowing of SRB diffusion. Second, coulombic interactions between the surface and dye might become saturated

above a certain surface charge density. The density of amine groups on the nanotube surface is estimated to be ~ 4 x 10^{14} cm^{-2}, suggesting a distance of ~ 0.5 nm between cationic sites at pH = 6.4. At pH = 8.4, the distance between cationic sites is ~ 1.9 nm, a factor of only ~ 4 greater. As the energy of coulombic interactions scales linearly with distance, this observation is consistent with a much smaller decrease in role played by these interactions at higher pH. Third, it is well known from the literature on the acid-base chemistry of amine-modified surfaces that the pK_a of surface-bound ammonium ions decreases with increasing charge density.[182,183] Therefore, a significant fraction of amine groups cannot be protonated, even at very low pH. The charge density at pH = 6.4 is likely to be far smaller than predicted above, as a result.

5.3.5 Model for SRB Mass Transport in Bolaamphiphile Nanotubes

The results discussed above in this chapter suggest a model for diffusion of negatively charged SRB molecules within the organic nanotubes. **Figure 5.8** provides a pictorial representation of this model in which the blue circles represent individual SRB molecules. Diffusion within the tubes clearly does not occur by a Fickian mechanism alone. The results show a dependence on both the ionic strength and the pH of the aqueous buffer filling the nanotubes, and no such dependence is expected for Fickian diffusion. It is concluded that coulombic interactions between the SRB molecules and the inner nanotube surfaces play an important role in limiting mass transport of the dye. These interactions likely involve adsorption and desorption of the dye from the nanotube surface. Previous investigations of diffusion by charged dyes in close proximity to charged surfaces have demonstrated that the dyes can adsorb to the surface for long periods of time.[116,173] Such events appear as anomalously long upward fluctuations in the fluorescence signal from the detection volume. No evidence of such long adsorption events was

found in any of the videos obtained for these studies. It is thus concluded that adsorption of the anionic dye to the (possibly) positively charged inner surfaces of the nanotubes occurs at high frequency, and that these events are short-lived on the imaging time scale. These adsorption events retard or briefly interrupt dye motion, while dye diffusion most likely occurs within the aqueous solution filling the tubes once they desorb. Little or no contribution from SRB molecules that have partitioned into the tube walls is expected, because the dye partitions too strongly into the aqueous phase. In this case, the mechanism for mass transport of the anionic SRB molecules within the tubes may best be described as desorption-mediated Fickian diffusion, in which the dye molecules may be viewed as 'hopping' between adsorption sites along the nanotube surface.

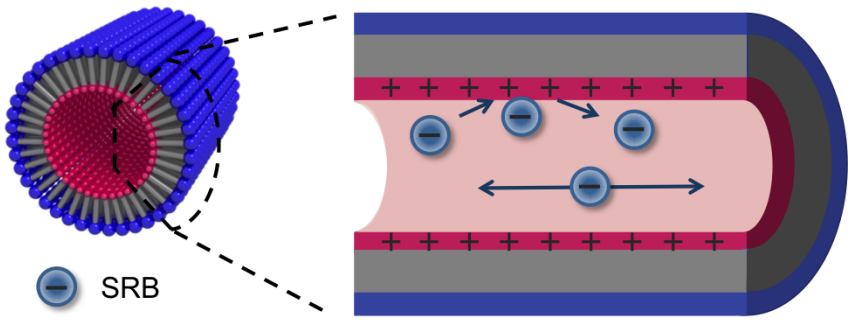

Figure 5.8 Model for SRB diffusion inside the organic nanotubes. The blue circles carrying negative charges represent individual SRB molecules. Diffusion involves a fast 'hopping' of the anionic molecules between cationic sites on the inner nanotube surface. The molecules are not drawn to scale to allow for better visualization.

Desorption-mediated diffusion has been observed for a wide variety of other materials as well.[184-186] Previous studies primarily employed single molecule tracking as a means to determine the mass transport mechanism and the dominance of desorption-mediated diffusion was revealed by a characteristic change in the single molecule step size distribution. In the present studies, we

show that changes in the apparent rate of diffusion brought about by modulation of the dye-surface interactions can also be detected in imaging-FCS studies and used to identify contributions from non-Fickian mass transport mechanisms. The participation of desorption-mediated diffusion would otherwise be difficult to detect within short nanotubes because of the small distances over which molecular motions occur.

5.4 Conclusions

The rate and mechanism of diffusion for anionic SRB dye molecules within self-assembled organic nanotubes was investigated by imaging-FCS. The organic nanotubes were assembled from unique bolaamphiphile monomers and carry a pH-dependent positive charge on their inner surfaces. Related nanotubes are being investigated by others as vehicles for use in controlled drug delivery.[98,161,162] The imaging-FCS data revealed that the SRB molecules moved along the nanotube long axis and that their apparent rate of diffusion was dependent upon both the ionic strength and pH of the aqueous buffer filling the tubes. The apparent rate of SRB diffusion was found to increase with increasing solution ionic strength at relatively low buffer concentrations and then to decrease at the highest ionic strengths. The role played by surface charge was revealed through an observed increase in the apparent rate of SRB diffusion with increasing buffer pH. These observations demonstrated that coulombic interactions between the cationic ammonium ions on the nanotube inner surface and the anionic SRB molecules played an integral role in governing SRB diffusion. It was concluded that mass transport of the dye within the nanotubes occurred by a desorption-mediated Fickian diffusion mechanism in which the dye molecules frequently adsorb to the nanotube inner surface and diffuse by Brownian-like motion when released from the surface into the solution filling the tube.

The results of these studies provide a better understanding of mass transport phenomena relevant to the use of these and other organic nanotubes in drug delivery applications. They reveal how ionic strength and pH may be used to control the rate of mass transport of drug molecules within the nanotubes and suggest possible means to trigger their release. Enhanced knowledge of these phenomena promises to lead to improved performance of these materials in drug delivery applications.

5.5 Contributions of Authors

Shinobu Nagasaka synthesized the organic nanotubes from monomers and helped with nanotube sample preparation. Naohiro Kameta and Mitsutoshi Masuda provided us with the nanotube materials and the tube structure figure used in the paper. Daniel Higgins and Takashi Ito guided the research and provided indispensable advice and suggestions during the experiments and publication preparation.

Chapter 6 - Studies of Nile Red and a Derivative Partitioning within Organic Nanotubes by Spectroscopic Imaging and Imaging Fluorescence Correlation Spectroscopy

6.1 Introduction

The development of environmentally friendly oxidation technologies is of current interest for chemical synthesis in both industry and academia.[187] The unsuccessful recovery of solvents from many existing oxidation processes are harmful to the environment.[188] Homogenous catalysts provide very high yields but can be difficult to separate from the reaction products. Heterogeneous catalysts can provide a solution to the issue.[189,190] However, the reactivity is generally lower because of the low availability of active sites.

Nano-catalysts with high surface area are able to significantly improve the contacts between reactants and the catalysts. They could also provide better separation from the reaction mixture due to their insolubility in the reaction media.[191] Organic nanotubes are one of the promising nano-catalysts. They are synthesized from low-cost natural materials under mild conditions,[160] and have well-defined morphologies and dimensions.[75,192] The carboxylate-terminated peptide lipids are especially interesting because these groups can coordinate with metal ions, making these nanotubes potential solid supports for metal ion catalysis.[83,193] Metal ion-coordinated organic nanotubes have been successfully applied as catalysts for the oxidation of various organic compounds in the presence of hydrogen peroxide and tert-butyl hydroperoxide.[104] The organic nanotubes have outer diameters of tens to hundreds of nanometers and are micrometers in length.

The high radial dimension allows for a large surface area for reaction. Multiple metal-coordinating layers afford even more reaction sites for the reactants. Liu and coworkers applied self-assembled organic nanotubes with five coordinating layers as catalysts in a Diels–Alder reaction.[99] The higher density of active sites resulted in an enhanced catalytic reaction. Thus, it would be advantageous for catalysis if the reactants could partition and interact more within the active sites of the catalysts.

In this chapter, solvatochromic dyes were used to investigate the partitioning of molecules within organic nanotubes submersed in organic solvent. NR and its derivative, 2-hydroxybenzophenoxazinone (NR-OH) were selected as models for reactant molecules with different polarity characteristics. NR molecules are neutral and relatively hydrophobic, while NR-OH with an extra phenolic hydroxyl group is more hydrophilic than NR. This work may afford information on the accessibility of reactant molecules to different reactive sties in organic nanotubes, and thus help to improve the performance of nanotube-based catalysis systems.

6.2 Experimental Section

6.2.1 Materials

The specific organic nanotube applied in this chapter is the same as the one in Chapter 5. They are formed from monomers of *N*-(*β*-D-Glucopyranosyl)-*N′*-(2-glycylglycylglycine-amideethyl)-icosane-diamide. The resulting nanotubes have amine groups on their inner surfaces, glucose headgroups on their outer surfaces, and hydrophobic hydrocarbon chains as the tube wall. The molecular structure and characterization of the nanotubes was shown in **Figures 3.3 and 5.1**.

Detailed properties of the nanotubes were given in Chapter 5. NR dye was purchased from Sigma-Aldrich, and was used as received. The structures of NR and NR-OH are shown in **Figure 6.1**.

The nanotubes were first immobilized on the glass coverslip and then doped with NR at 150 μM or NR-OH at 30 μM. The doping procedures were described in Section 5.2.1. The selection of dye concentration was based on the experimentally determined relationship between autocorrelation amplitude and the doping concentration. For FCS imaging experiments, a rectangular PDMS well was fabricated and placed over the coverslip. The PDMS well was filled with ethanol immediately before the imaging experiments and was then covered with a PDMS slab with a small opening. Ethanol was added continuously to the PDMS well during the experiment to prevent evaporation. All fluorescence videos of the nanotubes were acquired under an ethanol environment.

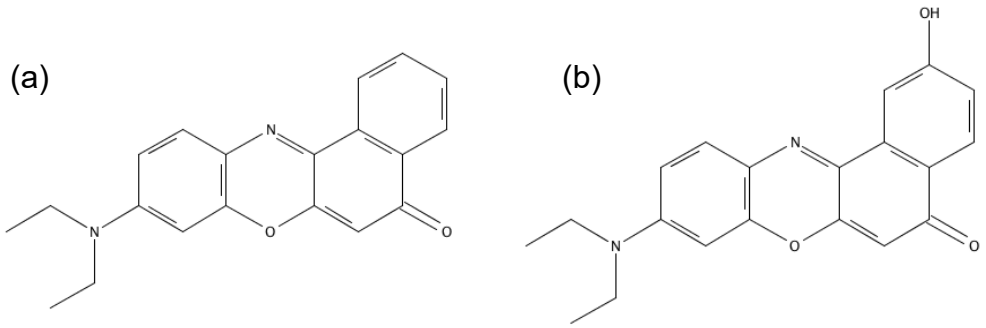

Figure 6.1 Chemical structures of (a) NR and (b) NR-OH.

In order to determine the pKa of the phenolic proton in NR-OH, titration of the dye was conducted in an ethanol/water (1:1) solution mixture. Titration involved adding 0.1% NaOH aqueous solution to the dye solution. The pH change was measured by a pH meter, while the fluorescence spectra of the dye were recorded on a fluorimeter. The concentration of NR-OH in the solution mixture was 10 μM.

6.2.2 Fluorescence Microscopy

All samples were imaged on a wide-field epi-fluoresence microscope. The microscopy setup is depicted in **Figure 6.2**. Individual dye molecules were excited by 514 nm laser light. The source light was passed through a dichroic beam splitter (Chroma 555, DCLP) and subsequently focused into an oil immersion objective (1.49 *NA*, Nikon Apo-TIRF, 100X). The incident power was maintained at 0.5 mW in all experiments. The excitation region in the images covered a relatively large lateral area of 32 μm × 32 μm. The fluorescence emission was reflected back through the same objective, and transmitted through a dichroic mirror and a 550 nm colored-glass long-pass filter. TIRF mode was employed to minimize background fluorescence from bulk solution. For spectroscopic imaging studies, two-color imaging was used to achieve the partition information.

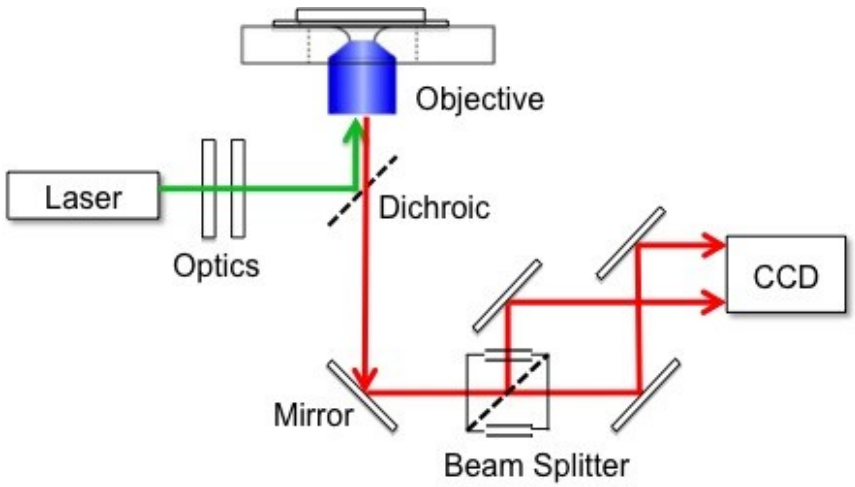

Figure 6.2 Wide field microscopy used for two-color imaging.

In this technique, the fluorescence was subsequently split into two spectral bands using an image splitter (Cairn Research OptoSplit II). The image splitter incorporated a second dichroic mirror (Chroma 605, DCLP) and appropriate bandpass filters to divide the fluorescence into

separate spectral bands spanning 625±20 nm and 580±20 nm. Fluorescence in these two bands was simultaneously detected using an EM-CCD camera (Andor iXon DU-897). Images were initially recorded from the full field of view to identify and locate individual nanotubes. A small region (usually ~10 μm x 3 μm) covering each chosen nanotube was then manually selected. Fluorescence videos of the selected regions were then recorded for imaging-FCS analysis. All fluorescence videos were recorded with 2 ms exposure times and were 25000 frames in length. The EM gain was set to 30, the readout rate to 10 MHz, and 3 x 3 pixel binning was employed. The videos were subsequently loaded into a program written in the LabVIEW (National Instruments) programming environment. This software subtracted the image background and calculated the autocorrelation function at each pixel, across the final 20,000 video frames. The autocorrelation decays were then fit in the software to an appropriate model (the model described in Chapter 5) that included contributions from dye diffusion and photobleaching.

6.3 Preliminary Results and Discussion

In this section, preliminary results for the NR and NR-OH experiments are given and discussed. First, the partitioning of NR and NR-OH was studied by spectroscopic imaging, diffusion behavior of NR and NR-OH was then explored by the imaging-FCS method.

6.3.1 Spectroscopic Imaging Studies

The partitioning information for the dye molecules within the organic nanotubes was obtained by the analysis of spectroscopic two-color imaging data. Similar methods have been employed in studies of local polarity in surfactants and micellar solutions.[194-196] Before studying

the dye partitioning behavior, the spectroscopic response of each dye to environments of different polarity (i.e., dielectric constant) was first explored. The spectral response of the dye molecules was obtained using a series of bulk ethanol/hexane mixtures. The solution-phase response of the dye (e.g., fluorescence emission ratio) was recorded on the same microscope used in the two-color imaging experiments. In these experiments, dye solutions were loaded into a liquid cell (designed in-house) that was placed on top of the microscope objective. Fluorescence videos were then acquired from each dye solution. Finally, the background-subtracted average signals in the 580 and 625 nm image channels were measured to determine the emission ratio. The emission ratio, *E*, for each solution was then calculated, as given in Eq. 6.1.

$$E = \frac{I_{625} - I_{580}}{I_{625} + I_{580}} \quad \text{(Eq. 6.1)}$$

Three replicate experiments were conducted in three days and average *E* values were obtained. **Figure 6.3** shows the calibration data for the NR and NR-OH dyes. As shown in the figure, the *E* values were found to be linearly dependent on the Clausius-Mossotti factor (CM factor), (ε -1)/(2ε + 1), of the solvent mixture.[197] The empirical relationship between the *E* values and CM factor is given in Eq. 6.2.

$$E = K\left(\frac{\varepsilon - 1}{2\varepsilon + 1}\right) + C \quad \text{(Eq. 6.2)}$$

The Onsager reaction field model[194] describing the solvent polarity dependence of dye emission includes a second term that is based on the optical frequency dielectric constant, n^2. Here, this second term ($(n^2-1)/(2n^2+1)$) was included as a constant, because hexane and ethanol have similar refractive indexes.[196] For NR dye, fitting of the data points in **Figure 6.3a** to Eq.6.2 yields the parameters $K = 3.6 \pm 0.20$, and $C = -0.93 \pm 0.07$. While for NR-OH, the calibration curve is also in linear dependence. The *K* and *C* values generated are 3.1 ± 0.17 and -0.74 ± 0.06, respectively. By this calibration, it is possible to relate the *E* values to dielectric constants, and thus the polarity

of the local environment in which the dye molecules are found. For example, the *E* values of NR range from -0.32 to 0.82, corresponding to dielectric constants ranging from 1.89 (pure hexane) to 24.6 (pure ethanol).

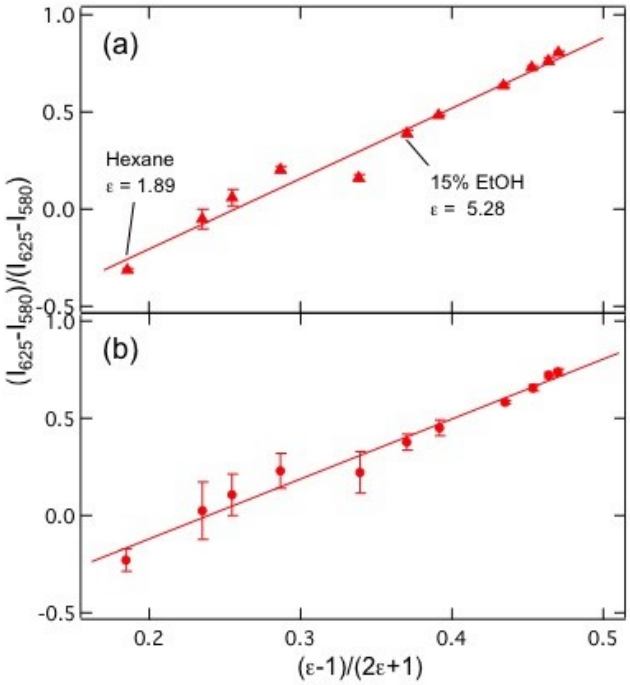

Figure 6.3 The emission ratios (I_{625} - I_{580})/(I_{625} + I_{580}) of NR (a) and NR-OH (b) as a function of the CM factor for a series of hexane/ethanol mixtures. From the left, the solution compositions are 0%, 2%, 3%, 5%, 10%, 15%, 20%, 40%, 60%, 80%, and 100% ethanol (by volume), with the remainder being hexane. The dye concentration in each case was 2 µM. The error bars are standard deviations of 3 replicate measurements for NR and 11 measurements for NR-OH.

Figure 6.4a,b shows a typical two-color wide-field image of the NR-doped nanotubes in emission channels centered at 625 nm (a) and 580 nm (b). Most nanotubes appeared to be brighter in the 625 nm channel than in the 580 nm channel. This indicates a positive *E* value for these nanotubes. To quantitatively assess the partitioning behavior, analysis of the *E* values for each dye-doped nanotube was carried out. First, a position dependence of the dye partition behavior along the tubes was studied. Each nanotube was equally divided into three regions (two ends and

a center) along the tube long axis in ImageJ software. Then, fluorescence intensities for each region in the two channels were averaged over the first ten frames in the fluorescence videos. Finally, averaged *E* values for NR and NR-OH at the ends and the center of each nanotube were obtained. The averaged *E* values for NR were 0.24 ± 0.12 and 0.23 ± 0.12 for tube ends and center, respectively. The values obtained demonstrate that there is no position dependence in the *E* values along the nanotube length. The data of NR-OH also showed no position dependence in the *E* values. Therefore, in the following data analysis, the *E* value was averaged over the whole tube region, affording one *E* value for each tube. **Figure 6.4c** shows the distribution of *E* values and corresponding CM factors measured from 19 NR-doped nanotubes. The main population was fitted with Gaussian function, giving a peak of *E* value at 0.25 and CM factor at 0.33. The peak value is very similar to the calculated result (0.24) averaged from the 19 data points. The peak value corresponds to an environment with polarity similar to that of a ~10% EtOH mixture with hexane. The dielectric constant for this environment is calculated to be 3.9. The distribution of *E* values spread from -0.06 to 0.4. This result indicates that the polarity of the NR environment may vary from that of a ~3% EtOH solution to that of a ~15% EtOH solution, in the absence of measurement error. Therefore, these results demonstrate that the NR molecules locate in relatively nonpolar regions within the nanotubes, possibly in the hydrocarbon region of the tube wall, but near the triglycine moieties.

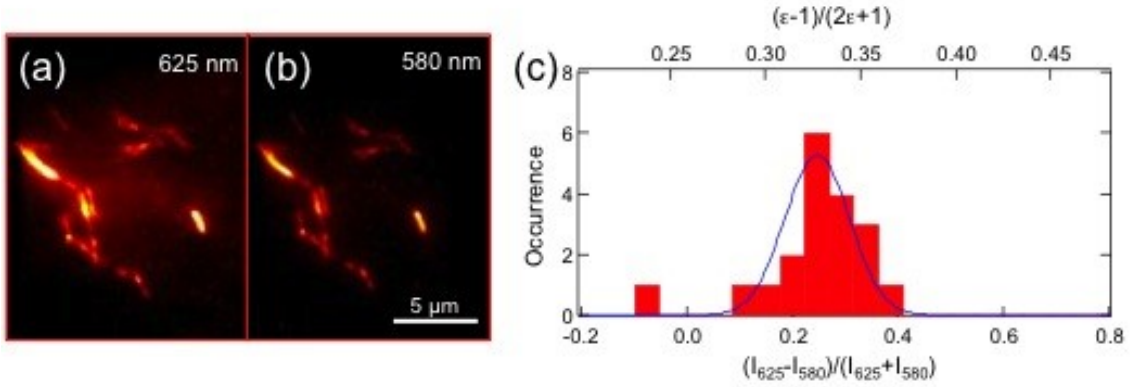

Figure 6.4 (a, b) Fluorescence images showing nanotubes doped with NR in a two-channel image for emission centered at 625 nm and 580 nm, respectively. (c) Distributions of *E* values (bottom) and CM factors (top) for 19 nanotubes doped with NR. Each data point represents one *E* value/CM factor averaged from one nanotube. The blue curve shows the fitting of the main populations to Gaussian functions.

For NR-OH, the averaged *E* value obtained from 12 nanotubes was 0.20 ± 0.06, and this corresponds to a CM factor of 0.30 ± 0.02. This indicates the NR-OH molecules may have partitioned into more nonpolar regions than NR. Since NR-OH is expected to be more polar than NR, this data is somewhat unexpected. However, it is likely that the number of measurements performed to date is simply too few to draw a concrete conclusion on polarity and partitioning of these dyes. We also suspect that the amine groups on the tube inner surfaces may deprotonate the phenolic hydroxyl groups on NR-OH when it interacts with the tube inner surfaces. If this were true, the calibration curve of NR-OH would be incorrect to apply for the nanotube system. Therefore, a fluorescence emission spectrum of NR-OH was taken in a concentrated amine environment to examine the possible deprotonation effect by the amine groups in the nanotubes. **Figure 6.5** shows the emission spectrums of 200 nM NR (red) and NR-OH (blue) in ethanol (solid curve) and pure 3-methoxylpropylamine (dash curve). NR molecules emitted peak fluorescence at 633 nm in ethanol and 598 nm in pure amine solvent. The slight blue-shift might be due to the dielectric constant change of the solvent environment. However, the emission peak of NR-OH

shifted from 622 nm in ethanol to 525 nm in pure 3-methoxylpropylamine with significant change in peak shape. The reason of this shift is not clear yet. But it is possible that the phenolic hydroxyl groups on NR-OH dye were deprotonated by the amine groups. Nagy and coworkers found the absorption spectrum of NR-OH broadened and the maximum shifted from 547 to 523 nm on the addition of 9.9 mM tetrabutylammonium hydroxide (Bu_4NOH) in methanol.[198] A similar shift was also observed using NaOH as a base in 5% methanol aqueous solutions. Titration of NR-OH was conducted in solvent mixtures of ethanol and water (1:1) to examine the pK_a of the hydroxyl groups on NR-OH. The pK_a was determined to be ~ 8.4, which is slightly larger than the pK_a of amine groups (7.27) on the tube inner surfaces.[68] Nevertheless, it is noteworthy that the pK_a of amine groups were measured in a solution of the nanotubes. Thus, the value was averaged over a large amount of tightly packed amine groups. Aliphatic amines, however, usually have pK_a values at around 10 in dilute solution. For example, the pK_a of 0.02 M methylamine was determined to be 10.67 in water.[199] Therefore, some individual sites of the amine groups on the tube inner surfaces might possess much higher pK_a value than 7.27 and be able to deprotonate the hydroxyl group on NR-OH easily.

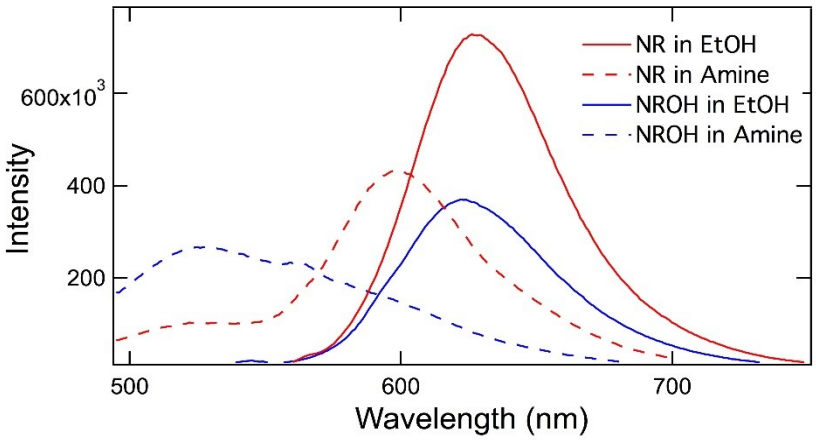

Figure 6.5 Fluorescence emission spectra of 200nM NR (red) and NR-OH (blue) in ethanol (solid curve) and pure 3-methoxylpropylamine (dash curve), respectively.

In the next step, we worked on the modification of the NR-OH to remove the acidic proton to prevent the aforementioned effects. Details of the modification are given in the Section 6.4 of this chapter.

6.3.2 Imaging-FCS Studies

Imaging-FCS was applied to obtain diffusion information of dye molecules within the organic nanotubes. The apparent diffusion coefficients were determined by autocorrelating the fluorescence video data on a pixel-by-pixel basis and fitting the autocorrelation decays obtained to an appropriate model. The specific procedures of analysis and the fitting model were described in Section 5.3.2. The resulting apparent diffusion coefficients determined from the 580 nm and 625 nm image channels are respectively abbreviated as D_{580} and D_{625} hereafter.

Figure 6.6 plots the averaged apparent diffusion coefficients D_{580} and D_{625} for NR and NR-OH molecules. Each D value was averaged over the entire tube region on a pixel-by-pixel basis. Overall, the diffusion coefficient for NR-OH was found to be larger than NR in both image channels. For example, the D_{580} for NR-OH and NR are 1.4×10^{-9} and 0.72×10^{-9} cm^2/s, respectively. A statistical analysis of these results shows that the two D values differ at 99.9% confidence. This suggests the NR-OH molecules might be present in the inner space of the nanotubes, in which the molecules spend a relatively longer time diffusing freely in the ethanol phase filling the tubes. The NR molecules are thus concluded to spend relatively more time diffusing in the tube walls. The conclusion that NR-OH may spend more time in solution inside the nanotubes is consistent with the expectation that it may be deprotonated by interaction with the amine groups on the tube inner surfaces.

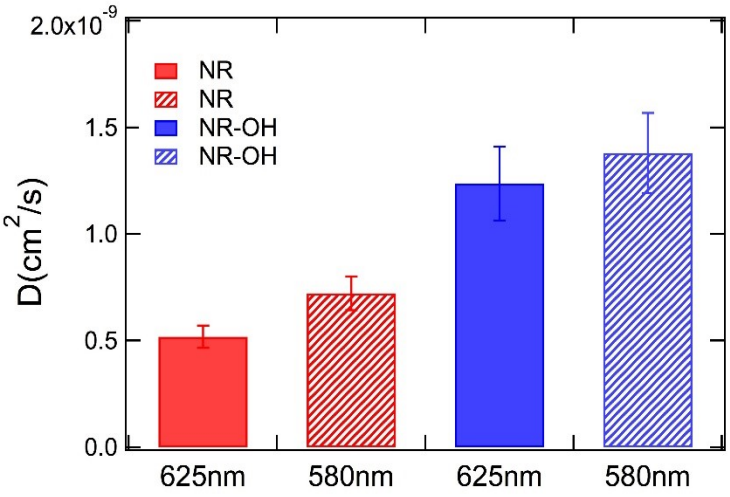

Figure 6.6 Averaged apparent diffusion coefficients for NR (red) and NR-OH (blue) at 625 nm and 580 nm image channels. The *D* values at 580 and 625 nm were obtained from the split-channel videos in two image channels. Error bars are standard errors on the mean.

A statistical analysis of the diffusion coefficient results obtained for the individual imaging channels indicates that the D_{580} value for NR is larger than the D_{625} value at a 96% confidence level. This might reflect the slowing of these molecules by H-bonding interactions with the triglycine moieties near the tube walls, the amine groups on the tube inner surfaces or the glucose group on the tube outer surfaces. Molecules found in these more polar regions of the tube should emit more strongly in the 625 nm channel. In contrast, the *D* values obtained for the NR-OH molecules were statistically indistinguishable in the two channels. This observation may suggest efficient partitioning of NR-OH out of the hydrophobic tube wall. But, the different situations for the *D* values of NR and NR-OH could be due to the greater experimental error in the latter, as depicted in the figure. More experiments will be required to draw any clear conclusions.

6.4 Modification of NR-OH

A two-step reaction was carried out to remove the acidic proton on the NR-OH and modify its structure. First, to a mixture of triethylene glycol (0.45mL, 3.3 mmol) and toluene (15 mL) was added concentrated HBr (0.41 mL of 48% aqueous solution, 3.7 mmol). The heterogeneous mixture was stirred and heated at reflux for 14 hr. The reaction mixture was allowed to cool to room temperature and the organic phase was separated. The organic layer was washed with

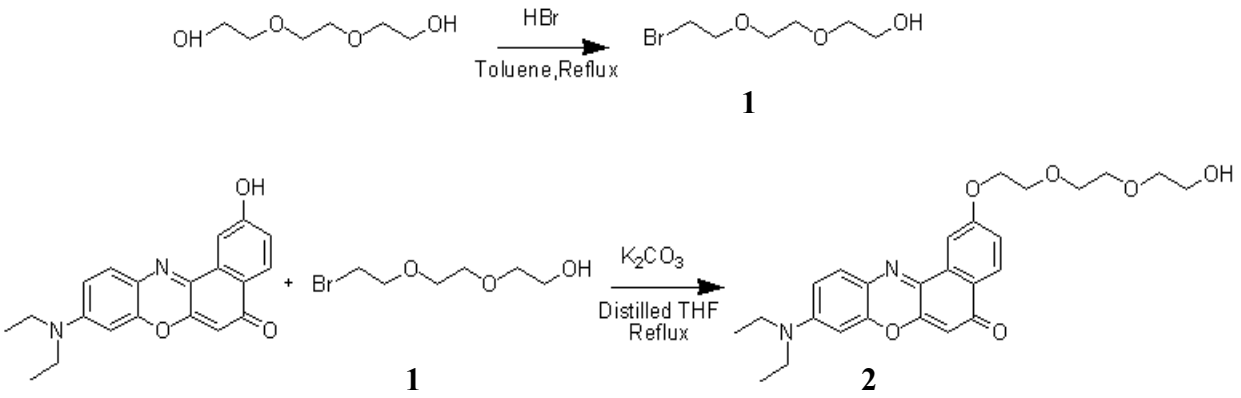

Figure 6.7 Synthesis route to NR-OH derivative 2.

brine, dried with $NaSO_4$ and concentrated on a rotary evaporator. Column chromatography of the crude product on a silica gel column with ethyl acetate as the mobile phase provided 94 mg of **1**. ^1H NMR ($CDCl_3$) δ ppm: 1.62 (br s, 1H), 3.48 (t, J=6.44 Hz, 2H), 3.58-3.77 (m, 8H), 3.82 (t, J=6.44 Hz, 2H). In the second step, a mixture of NR-OH (10 mg, 0.03 mmol), potassium carbonate (12.5 mg, 0.09 mmol) and **1** (9.6 mg, 0.05 mmol) in distilled THF (4 mL) was heated under reflux for 15 hr. Excess potassium carbonate was filtered out and the filtrate was extracted and concentrated on a rotary evaporator. The crude product was purified by column chromatography (with ethyl acetate as the mobile phase) and yielded a red solid, **2**. Unfortunately, the mass of the

product obtained was too small to conduct further experiments. This synthesis will need to be repeated to obtain enough of the final product for fluorescence measurements.

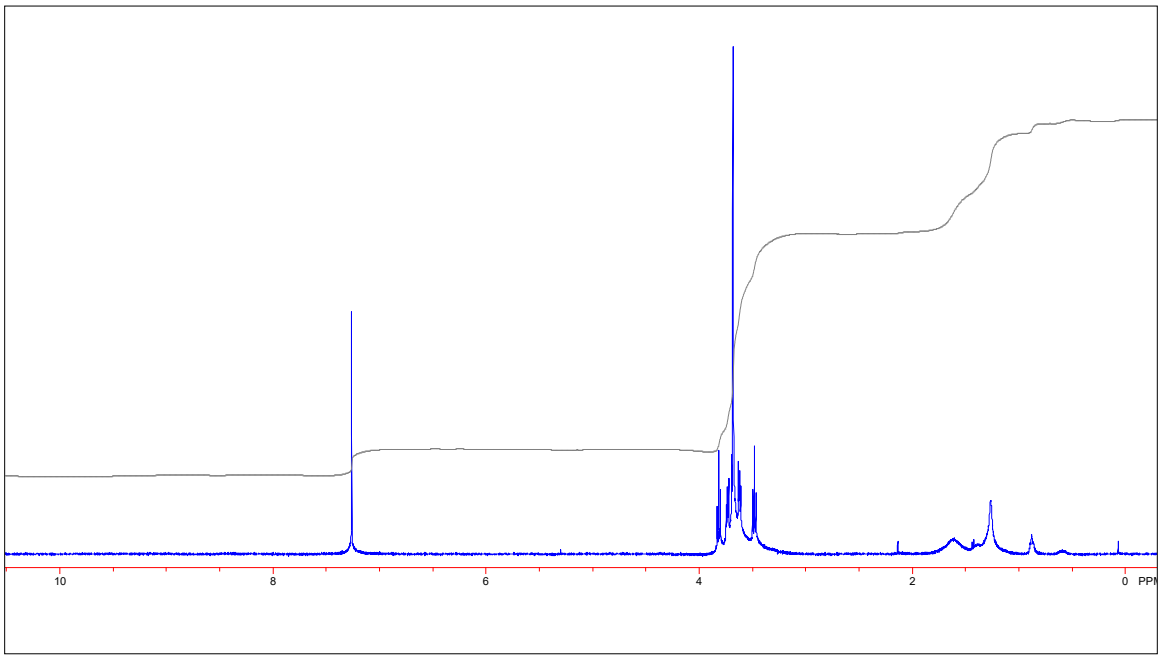

Figure 6.8 ^{1}H NMR spectrum of 1: 2-(2-(2-Bromoethoxy)ethoxy)ethanol.

6.5 Conclusions

In this chapter, the interaction and diffusion of NR and NR-OH dye molecules within self-assembled organic nanotubes immersed in ethanol solution were investigated. We sought to information on the partitioning of the molecules with different polarity characteristics in organic solvent. The goal was to explore the molecular partitioning and diffusion within the nanotubes, and to obtain information on the accessibility of reactants to the active sites on the nanotubes in catalysis, but it is uncertain that there is a good connection at this point. So far, we obtained the partitioning information for hydrophobic NR molecules. They were found to mostly interact with the nonpolar tube wall regions of the nanotubes. NR-OH diffuses faster than NR, as it is likely to

be found more commonly in the ethanol solvated regions inside the nanotubes. To compare NR with a more hydrophilic dye molecule, NR-OH later would be alkylated to remove the acidic proton, and thus eliminate the possibility of its deprotonation.

6.6 Contributions

NR-OH dye used in the experiments was synthesized by Saroja Ginagunta and purified by column chromatography by Shinobu Nagasaka. Shinobu Nagasaka also helped with the organic nanotube synthesis and sample preparation. Man Zhang conducted the NMR measurements in the NR-OH derivative synthesis and provided suggestions on synthesis experiments. Daniel Higgins and Takashi Ito guided the research and advised the experimental trouble-shooting.

Chapter 7 - General Conclusions and Future Directions

This dissertation presented the characterization of molecular diffusion and interaction within self-assembled nanomaterials. Single molecule imaging, imaging-FCS and spectroscopic imaging allow for detection of mass transport and the results obtained reflect the local material characteristics of the incorporated nanostructures. They are much more advantageous than the conventional ensemble methods that only provide averaged information across each sample region. Single molecule imaging allowed for molecule diffusion in local material structures to be monitored. Imaging-FCS could be used to assess the local probe dynamics with both high spatial resolution and time resolution on a broad sample region (ca. ~3 μm x 3 μm). Spectroscopic imaging, on the other hand, provided the data necessary to evaluate probe partitioning within the nanostructures.

In Chapter 4, single molecule imaging was employed to investigate the diffusion of individual DNA molecules in flow aligned hexagonal F127 mesophase. The results showed that the ds-DNA molecules were elongated with the long axis of the DNA molecules aligned parallel to the flow direction. DNA elongation and alignment may involve adsorption of one strand end to the glass surface, or its capture by an adsorbed, structured surface layer of F127. Electrophoretic migration was observed to occur exclusively along the local flow alignment direction within hexagonal mesophase for fields applied parallel to flow alignment, at ~45^{o} and at ~90^{o}. These results show that ds-DNA was strongly confined by the micelles comprising the gel.

Chapter 5 elucidated the diffusion of SRB dye molecules within organic nanotubes self-assembled from bolaamphiphile surfactants. The rate and mechanism of diffusion were explored by imaging-FCS. The technique also enabled the spatial resolution of the SRB transport dynamics. The results show that coulombic interactions between cationic ammonium ions on the inner

nanotube surface and the anionic SRB molecules play a critical role in governing mass transport of the dye. The apparent dye diffusion coefficient was found to generally increase with increasing ionic strength and pH. A desorption-mediated Fickian diffusion mechanism was proposed to describe mass transport of the SRB molecules. Molecular motions were slowed by coulombic interactions with the inner surfaces of the nanotubes.

In Chapter 6, spectroscopic imaging was applied to study the partitioning of NR and a NR-OH derivative in the organic nanotubes. The spectroscopic response of solvatochromic NR to different environmental polarities was established on the wide-field microscope. This relationship was employed to obtain the location of probe molecules, based on CM factors measured for the environments. The calculated CM factor indicated that NR molecules mostly partition into nonpolar regions in the nanotubes. These regions may represent the hydrophobic tube walls, possibly near the triglycine moieties. The partitioning of NR-OH could not be determined because the phenolic hydroxyl group appeared to be deprotonated in the presence of amine groups such as those covering the inner surfaces of the nanotubes. Modification of the NR-OH structure has been conducted but repeated synthesis is needed. The diffusion of NR and NR-OH was investigated by imaging-FCS. NR-OH were found to diffuse faster than NR, which might reflect the preferential partitioning of the NR-OH dye into the ethanol-filled tube, while NR spends more time diffusing in the tube walls.

This dissertation has described the application of fluorescence microscopy techniques in revealing mass transport of probe molecules in nanomaterials and the material properties. Imaging-FCS, as one of the important techniques, was proved to be a convenient tool to detect fast molecule diffusion over a relatively large sample region. However, there are two issues that need to be more carefully considered and optimized in the future. First, the dye concentration in the detection

region needs to be low enough owing to the mechanism of imaging-FCS. However, relatively low dye concentration can decrease the S/N ratio of the fluorescence signal. Laser power can be tuned high to increase S/N ratio but severe photobleaching could then be induced. The parameters need to be balanced with some data accuracy lost. It was later found that very small laser power (ca. ~0.01mW) could be sufficient to detect single molecule fluorescence under certain experimental conditions. Thus the laser power can be further optimized with the dye concentration to obtain higher level of data accuracy. Also, since the imaging-FCS data was analyzed from each pixel for each selected tube region, it is important to make sure the pixels selected are precisely from the tubes. Thus it would be advantageous to establish a model of quantitatively selecting the tube regions rather than determining the area by the observed fluorescence.

References

(1) Schmidt-Mende, L.; Fechtenkotter, A.; Mullen, K.; Moons, E.; Friend, R. H.; MacKenzie, J. D. Self-Organized Discotic Liquid Crystals for High-Efficiency Organic Photovoltaics. *Science* **2001**, *293*, 1119-1122.

(2) Schwiebert, K. E.; Chin, D. N.; MacDonald, J. C.; Whitesides, G. M. Engineering the Solid State with 2-Benzimidazolones. *Journal of the American Chemical Society* **1996**, *118*, 4018-4029.

(3) De Rosa, C.; Park, C.; Thomas, E. L.; Lotz, B. Microdomain Patterns from Directional Eutectic Solidification and Epitaxy. *Nature* **2000**, *405*, 433-437.

(4) Xia, Y. N.; Yang, P. D.; Sun, Y. G.; Wu, Y. Y.; Mayers, B.; Gates, B.; Yin, Y. D.; Kim, F.; Yan, Y. Q. One-Dimensional Nanostructures: Synthesis, Characterization, and Applications. *Advanced Materials* **2003**, *15*, 353-389.

(5) Ito, T. Block Copolymer-Derived Monolithic Polymer Films and Membranes Comprising Self-Organized Cylindrical Nanopores for Chemical Sensing and Separations. *Chemistry-an Asian Journal* **2014**, *9*, 2708-2718.

(6) Kameta, N.; Minamikawa, H.; Masuda, M. Supramolecular Organic Nanotubes: How to Utilize the Inner Nanospace and the Outer Space. *Soft Matter* **2011**, *7*, 4539-4561.

(7) Zhang, H.; Xiong, L. F.; He, Z. D.; Zhong, A. Q.; Wang, T. Q.; Xu, Y.; Zhou, M. H.; Huang, K. Functionalized Microporous Organic Nanotube Networks as a New Platform for Highly Efficient Heterogeneous Catalysis. *Polymer Chemistry* **2016**, *7*, 4975-4982.

(8) Zhou, Z.; He, C.; Xiu, J. H.; Yang, L.; Duan, C. Y. Metal-Organic Polymers Containing Discrete Single-Walled Nanotube as a Heterogeneous Catalyst for the Cycloaddition

of Carbon Dioxide to Epoxides. *Journal of the American Chemical Society* **2015**, *137*, 15066-15069.

(9) Beck, J. S.; Vartuli, J. C.; Roth, W. J.; Leonowicz, M. E.; Kresge, C. T.; Schmitt, K. D.; Chu, C. T. W.; Olson, D. H.; Sheppard, E. W.; McCullen, S. B.; Higgins, J. B.; Schlenker, J. L. A New Family of Mesoporous Molecular-Sieves Prepared with Liquid-Crystal Templates. *Journal of the American Chemical Society* **1992**, *114*, 10834-10843.

(10) Weitzel, C. R.; Everett, T. A.; Higgins, D. A. Aggregation and Its Influence on Macroscopic In-Plane Organization in Thin Films of Electrostatically Self-Assembled Perylene-Diimide/Polyelectrolyte Nanofibers. *Langmuir* **2009**, *25*, 1188-1195.

(11) Papathanassoglou, D. A.; Vohnsen, B. Direct Visualization of Evanescent Optical Waves. *American Journal of Physics* **2003**, *71*, 670-677.

(12) Ahmad, M.; Hench, L. L. Effect of Taper Geometries and Launch Angle on Evanescent Wave Penetration Depth in Optical Fibers. *Biosensor & Bioelectronics* **2005**, *20*, 1312-1319.

(13) Hood, K.; Nix, B. A. J.; Iles, T. C. Asymptotic Information and Variance-Covariance Matrices for the Linear Structural Model. *Journal of the Royal Statistical Society Series D-the Statistician* **1999**, *48*, 477-493.

(14) Selvam, P.; Bhatia, S. K.; Sonwane, C. G. Recent Advances in Processing and Characterization of Periodic Mesoporous MCM-41 Silicate Molecular Sieves. *Industrial & Engineering Chemistry Research* **2001**, *40*, 3237-3261.

(15) Kuchibhatla, S.; Karakoti, A. S.; Bera, D.; Seal, S. One Dimensional Nanostructured Materials. *Progress in Materials Science* **2007**, *52*, 699-913.

(16) Karger, J.; Valiullin, R. Mass Transfer in Mesoporous Materials: the Benefit of Microscopic Diffusion Measurement. *Chemical Society Reviews* **2013**, *42*, 4172-4197.

(17) Higgins, D. A.; Tran-Ba, K. H.; Ito, T. Following Single Molecules to a Better Understanding of Self-Assembled One-Dimensional Nanostructures. *Journal of Physical Chemistry Letters* **2013**, *4*, 3095-3103.

(18) Higgins, D. A.; Park, S. C.; Tran-Ba, K.-H.; Ito, T. Single-Molecule Investigations of Morphology and Mass Transport Dynamics in Nanostructured Materials. *Annu. Rev. Anal. Chem.* **2015**, *8*, 193-216.

(19) Schmidt, T.; Schutz, G. J.; Baumgartner, W.; Gruber, H. J.; Schindler, H. Imaging of Single Molecule Diffusion. *Proceedings of the National Academy of Sciences of the United States of America* **1996**, *93*, 2926-2929.

(20) Krichevsky, O.; Bonnet, G. Fluorescence Correlation Spectroscopy: the Technique and its Applications. *Reports on Progress in Physics* **2002**, *65*, 251-297.

(21) Cooper, J. T.; Harris, J. M. Imaging Fluorescence-Correlation Spectroscopy for Measuring Fast Surface Diffusion at Liquid/Solid Interfaces. *Analytical Chemistry* **2014**, *86*, 7618-7626.

(22) Xu, H.; Nagasaka, S.; Kameta, N.; Masuda, M.; Ito, T.; Higgins, D. A. Imaging Fluorescence Correlation Spectroscopy Studies of Dye Diffusion in Self-Assembled Organic Nanotubes. *Physical Chemistry Chemical Physics* **2016**, *18*, 16766-16774.

(23) Whitesides, G. M.; Grzybowski, B. Self-Assembly at All Scales. *Science* **2002**, *295*, 2418-2421.

(24) Hecht, S. Welding, Organizing, and Planting Organic Molecules on Substrate Surfaces - Promising Approaches towards Nanoarchitectonics from the Bottom up. *Angewandte Chemie-International Edition* **2003**, *42*, 24-26.

(25) Daniel, M. C.; Astruc, D. Gold Nanoparticles: Assembly, Supramolecular Chemistry, Quantum-Size-related Properties, and Applications toward Biology, Catalysis, and Nanotechnology. *Chemical Reviews* **2004**, *104*, 293-346.

(26) Park, C.; Yoon, J.; Thomas, E. L. Enabling Nanotechnology with Self Assembled Block Copolymer Patterns. *Polymer* **2003**, *44*, 6725-6760.

(27) Hamley, I. W. Nanotechnology with Soft Materials. *Angewandte Chemie-International Edition* **2003**, *42*, 1692-1712.

(28) Olson, D. A.; Chen, L.; Hillmyer, M. A. Templating Nanoporous Polymers with Ordered Block Copolymers. *Chemistry of Materials* **2008**, *20*, 869-890.

(29) Croy, S. R.; Kwon, G. S. Polymeric Micelles for Drug Delivery. *Current Pharmaceutical Design* **2006**, *12*, 4669-4684.

(30) Hu, H. Q.; Gopinadhan, M.; Osuji, C. O. Directed Self-assembly of Block Copolymers: a Tutorial Review of Strategies for Enabling Nanotechnology with Soft Matter. *Soft Matter* **2014**, *10*, 3867-3889.

(31) Hillmyer, M. A. Nanoporous Materials from Block Copolymer Precursors. *Block Copolymers II* **2005**, *190*, 137-181.

(32) Kim, B. J.; Fredrickson, G. H.; Kramer, E. J. Effect of Polymer Ligand Molecular Weight on Polymer-Coated Nanoparticle Location in Block Copolymers. *Macromolecules* **2008**, *41*, 436-447.

(33) Liu, G.; Zhao, J. Guided Alignment and Positioning of Single DNA Molecules by a Structured Contact Line on a Block Copolymer Surface. *Langmuir* **2006**, *22*, 2923-2926.

(34) Wischerhoff, E.; Badi, N.; Laschewsky, A.; Lutz, J. F. Smart Polymer Surfaces: Concepts and Applications in Biosciences. *Bioactive Surfaces* **2011**, *240*, 1-33.

(35) Kabanov, A. V.; Batrakova, E. V.; Alakhov, V. Y. Pluronic block Copolymers as Novel Polymer Therapeutics for Drug and Gene Delivery. *Journal of Controlled Release* **2002**, *82*, 189-212.

(36) Batrakova, E. V.; Kabanov, A. V. Pluronic Block Copolymers: Evolution of Drug Delivery Concept from Inert Nanocarriers to Biological Response Modifiers. *Journal of Controlled Release* **2008**, *130*, 98-106.

(37) Holmqvist, P.; Alexandridis, P.; Lindman, B. Modification of the Microstructure in Block Copolymer-Water-"Oil" Systems by Varying the Copolymer Composition and the "Oil" Type: Small-Angle X-ray Scattering and Deuterium-NMR Investigation. *Journal of Physical Chemistry B* **1998**, *102*, 1149-1158.

(38) Lee, Y.; Chung, H. J.; Yeo, S.; Ahn, C. H.; Lee, H.; Messersmith, P. B.; Park, T. G. Thermo-Sensitive, Injectable, and Tissue Adhesive Sol-Gel Transition Hyaluronic Acid/Pluronic Composite Hydrogels Prepared from Bio-Inspired Catechol-Thiol Reaction. *Soft Matter* **2010**, *6*, 977-983.

(39) Bates, F. S.; Fredrickson, G. H. Block Copolymers - Designer Soft Materials. *Physics Today* **1999**, *52*, 32-38.

(40) Zhang, L. F.; Eisenberg, A. Multiple Morphologies and Characteristics of "Crew-cut" Micelle-like Aggregates of Polystyrene-b-poly(acrylic acid) Diblock Copolymers in Aqueous Solutions. *Journal of the American Chemical Society* **1996**, *118*, 3168-3181.

(41) Bates, F. S.; Fredrickson, G. H. Block Copolymer Thermodynamics - Theory and Experiment. *Annual Review of Physical Chemistry* **1990**, *41*, 525-557.

(42) Marencic, A. P.; Register, R. A. Controlling Order in Block Copolymer Thin Films for Nanopatterning Applications. *Annual Review of Chemical and Biomolecular Engineering, Vol 1* **2010**, *1*, 277-297.

(43) Nikoubashman, A.; Register, R. A.; Panagiotopoulos, A. Z. Simulations of Shear-Induced Morphological Transitions in Block Copolymers. *Soft Matter* **2013**, *9*, 9960-9971.

(44) Zheng, W.; Wang, Z. G. Morphology of ABC Triblock Copolymers. *Macromolecules* **1995**, *28*, 7215-7223.

(45) Melosh, N. A.; Davidson, P.; Feng, P.; Pine, D. J.; Chmelka, B. F. Macroscopic Shear Alignment of Bulk Transparent Mesostructured Silica. *Journal of the American Chemical Society* **2001**, *123*, 1240-1241.

(46) Imperor-Clerc, M.; Hamley, I. W.; Davidson, P. Fast and Easy Flow-Alignment Technique of Lyotropic Liquid-Crystalline Hexagonal Phases of Block Copolymers and Surfactants. *Macromolecules* **2001**, *34*, 3503-3506.

(47) Albalak, R. J.; Thomas, E. L. Microphase Separation of Block Copolymer Solutions in a Flow Field. *Journal of Polymer Science Part B-Polymer Physics* **1993**, *31*, 37-46.

(48) Angelescu, D. E.; Waller, J. H.; Adamson, D. H.; Deshpande, P.; Chou, S. Y.; Register, R. A.; Chaikin, P. M. Macroscopic Orientation of Block Copolymer Cylinders in Single-Layer Films by Shearing. *Advanced Materials* **2004**, *16*, 1736-1740.

(49) Sundrani, D.; Darling, S. B.; Sibener, S. J. Guiding polymers to perfection: Macroscopic alignment of nanoscale domains. *Nano Letters* **2004**, *4*, 273-276.

(50) Sundrani, D.; Darling, S. B.; Sibener, S. J. Hierarchical Assembly and Compliance of Aligned Nanoscale Polymer Cylinders in Confinement. *Langmuir* **2004**, *20*, 5091-5099.

(51) Park, S. M.; Craig, G. S. W.; Liu, C. C.; La, Y. H.; Ferrier, N. J.; Nealey, P. F. Characterization of Cylinder-Forming Block Copolymers Directed to Assemble on Spotted Chemical Patterns. *Macromolecules* **2008**, *41*, 9118-9123.

(52) Tranchemontagne, D. J. L.; Ni, Z.; O'Keeffe, M.; Yaghi, O. M. Reticular Chemistry of Metal-Organic Polyhedra. *Angewandte Chemie-International Edition* **2008**, *47*, 5136-5147.

(53) Kitagawa, S.; Matsuda, R. Chemistry of Coordination Space of Porous Coordination Polymers. *Coordination Chemistry Reviews* **2007**, *251*, 2490-2509.

(54) Lee, W.; Ji, R.; Gosele, U.; Nielsch, K. Fast Fabrication of Long-Range Ordered Porous Alumina Membranes by Hard Anodization. *Nature Materials* **2006**, *5*, 741-747.

(55) Yoshizawa, M.; Klosterman, J. K.; Fujita, M. Functional Molecular Flasks: New Properties and Reactions within Discrete, Self-Assembled Hosts. *Angewandte Chemie-International Edition* **2009**, *48*, 3418-3438.

(56) Nakashima, N.; Asakuma, S.; Kim, J. M.; Kunitake, T. Helical Superstructures are Formed from Chiral Ammonium Bilayers. *Chemistry Letters* **1984**, 1709-1712.

(57) Yamada, K.; Ihara, H.; Ide, T.; Fukumoto, T.; Hirayama, C. Formation of Helical Super Structure from Single-Walled Bilayers by Amphiphiles with Oligo-L-Glutamic Acid-Head Group. *Chemistry Letters* **1984**, 1713-1716.

(58) Kogiso, M.; Aoyagi, M.; Asakawa, M.; Shimizu, T. Highly Efficient Production of Various Organic Nanotubes with Different Surfaces and their Application to an Adsorbent. *Soft Matter* **2010**, *6*, 4528-4535.

(59) Kogiso, M.; Aoyagi, M.; Asakawa, M.; Shimizu, T. Semisolid Phase Synthesis of Metal-complexed Organic Nanotubes. *Chemistry Letters* **2010**, *39*, 822-823.

(60) Seifert, G.; Kohler, T.; Tenne, R. Stability of Metal Chalcogenide Nanotubes. *Journal of Physical Chemistry B* **2002**, *106*, 2497-2501.

(61) Yao, B. D.; Chan, Y. F.; Zhang, X. Y.; Zhang, W. F.; Yang, Z. Y.; Wang, N. Formation Mechanism of TiO2 Nanotubes. *Applied Physics Letters* **2003**, *82*, 281-283.

(62) Israelachivili, J. N.: *Intermolecular and Surface Forces*; Academic Press: New York, 1985.

(63) Steinhart, M. Supramolecular Organization of Polymeric Materials in Nanoporous Hard Templates. *Self-Assembled Nanomaterials Ii: Nanotubes* **2008**, *220*, 123-187.

(64) Masuda, M.; Shimizu, T. Lipid Nanotubes and Microtubes: Experimental Evidence for Unsymmetrical Monolayer Membrane Formation from Unsymmetrical Bolaamphiphiles. *Langmuir* **2004**, *20*, 5969-5977.

(65) Fuhrhop, A. H.; Wang, T. Y. Bolaamphiphiles. *Chemical Reviews* **2004**, *104*, 2901-2937.

(66) Kameta, N.; Masuda, M.; Minamikawa, H.; Mishima, Y.; Yamashita, I.; Shimizu, T. Functionalizable Organic Nanochannels Based on Lipid Nanotubes: Encapsulation and Nanofluidic Behavior of Biomacromolecules. *Chemistry of Materials* **2007**, *19*, 3553-3560.

(67) Kameta, N.; Masuda, M.; Minamikawa, H.; Goutev, N. V.; Rim, J. A.; Jung, J. H.; Shimizu, T. Selective Construction of Supramolecular Nanotube Hosts with Cationic Inner Surfaces. *Advanced Materials* **2005**, *17*, 2732-2736.

(68) Kameta, N.; Minamikawa, H.; Masuda, M.; Mizuno, G.; Shimizu, T. Controllable Biomolecule Release from Self-assembled Organic Nanotubes with Asymmetric Surfaces: pH and Temperature Dependence. *Soft Matter* **2008**, *4*, 1681-1687.

(69) Kameta, N.; Mizuno, G.; Masuda, M.; Minamikawa, H.; Kogiso, M.; Shimizu, T. Molecular Monolayer Nanotubes Having 7-9 nm Inner Diameters Covered with Different Inner and Outer Surfaces. *Chemistry Letters* **2007**, *36*, 896-897.

(70) Kameta, N.; Yoshida, K.; Masuda, M.; Shimizu, T. Supramolecular Nanotube Hydrogels: Remarkable Resistance Effect of Confined Proteins to Denaturants. *Chemistry of Materials* **2009**, *21*, 5892-5898.

(71) Liu, P.; Ni, R.; Mehta, A. K.; Childers, W. S.; Lakdawala, A.; Pingali, S. V.; Thiyagarajan, P.; Lynn, D. G. Nucleobase-Directed Amyloid Nanotube Assembly. *Journal of the American Chemical Society* **2008**, *130*, 16867-16869.

(72) Childers, W. S.; Ni, R.; Mehta, A. K.; Lynn, D. G. Peptide Membranes in Chemical Evolution. *Current Opinion in Chemical Biology* **2009**, *13*, 652-659.

(73) Savariar, E. N.; Sochat, M. M.; Klaikherd, A.; Thayumanavan, S. Functional Group Density and Recognition in Polymer Nanotubes. *Angewandte Chemie-International Edition* **2009**, *48*, 110-114.

(74) Kim, D. H.; Karan, P.; Goring, P.; Leclaire, J.; Caminade, A. M.; Majoral, J. P.; Gosele, U.; Steinhart, M.; Knoll, W. Formation of Dendrimer Nanotubes by Layer-by-Layer Deposition. *Small* **2005**, *1*, 99-102.

(75) Shimizu, T.; Masuda, M.; Minamikawa, H. Supramolecular Nanotube Architectures Based on Amphiphilic Molecules. *Chemical Reviews* **2005**, *105*, 1401-1443.

(76) Markowitz, M. A.; Schnur, J. M.; Singh, A. The Influence of the Polar Headgroups of Acidic Diacetylenic Phospholipids on Tubule Formation, Microstruture Morphology and Langmuir Film Behavior. *Chemistry and Physics of Lipids* **1992**, *62*, 193-204.

(77) Singh, A.; Wong, E. M.; Schnur, J. M. Toward the Rational Control of Nanoscale Structures using Chiral Self-Assembly: Diacetylenic Phosphocholines. *Langmuir* **2003**, *19*, 1888-1898.

(78) Douliez, J. P.; Pontoire, B.; Gaillard, C. Lipid Tubes with a Temperature-Tunable Diameter. *Chemphyschem* **2006**, *7*, 2071-2073.

(79) Douliez, J. P.; Gaillard, C.; Navailles, L.; Nallet, F. Novel Lipid System Forming Hollow Microtubes at High Yields and Concentration. *Langmuir* **2006**, *22*, 2942-2945.

(80) B.R. Ratna; S. Baral-Tosh; B. Kahn; J.M. Schnur; Rudolph, A. S. Effect of Alcohol Chain Length on Tubule Formation in 1,2-Bis(10,12-Tricosadiynoyl)-*sn*-Glycero-3-Phosphocholine. *Chemistry and Physics of Lipids* **1992**, *63*, 47-53.

(81) Thomas, B. N.; Safinya, C. R.; Plano, R. J.; Clark, N. A. Lipid Tubule Self-Assembly - Length Dependence on Cooling Rate through a First-Order Phase-Transition. *Science* **1995**, *267*, 1635-1638.

(82) Caffrey, M.; Hogan, J.; Rudolph, A. S. Diacetylenic Lipid Microstructures - Structural Characterization by X-ray-Diffraction and Comparison with the Ssturated Phosphatidylcholine Analog. *Biochemistry* **1991**, *30*, 2134-2146.

(83) Kogiso, M.; Zhou, Y.; Shimizu, T. Instant Preparation of Self-Assembled Metal-Complexed Lipid Nanotubes that Act as Templates to Produce Metal Oxide Nanotubes. *Advanced Materials* **2007**, *19*, 242-246.

(84) Shimizu, T.; Minamikawa, H.; Kogiso, M.; Aoyagi, M.; Kameta, N.; Ding, W.; Masuda, M. Self-organized Nanotube Materials and Their Application in Bioengineering. *Polymer Journal* **2014**, *46*, 831-858.

(85) Cao, H.; Duan, P. F.; Zhu, X. F.; Jiang, J.; Liu, M. H. Self-Assembled Organic Nanotubes through Instant Gelation and Universal Capacity for Guest Molecule Encapsulation. *Chemistry-a European Journal* **2012**, *18*, 5546-5550.

(86) Henricus, M. M.; Johnson, K. T.; Banerjee, I. A. Investigation of Insulin Loaded Self-Assembled Microtubules for Drug Release. *Bioconjugate Chemistry* **2008**, *19*, 2394-2400.

(87) Meilander, N. J.; Yu, X. J.; Ziats, N. P.; Bellamkonda, R. V. Lipid-based Microtubular Drug Delivery Vehicles. *Journal of Controlled Release* **2001**, *71*, 141-152.

(88) Ding, W. X.; Kameta, N.; Minamikawa, H.; Wada, M.; Shimizu, T.; Masuda, M. Hybrid Organic Nanotubes with Dual Functionalities Localized on Cylindrical Nanochannels Control the Release of Doxorubicin. *Advanced Healthcare Materials* **2012**, *1*, 699-706.

(89) Wakasugi, A.; Asakawa, M.; Kogiso, M.; Shimizu, T.; Sato, M.; Maitani, Y. Organic Nanotubes for Drug Loading and Cellular Delivery. *International Journal of Pharmaceutics* **2011**, *413*, 271-278.

(90) Maitani, Y.; Nakamura, Y.; Kon, M.; Sanada, E.; Sumiyoshi, K.; Fujine, N.; Asakawa, M.; Kogiso, M.; Shimizu, T. Higher Lung Accumulation of Intravenously Injected Organic Nanotubes. *International Journal of Nanomedicine* **2013**, *8*, 315-323.

(91) Song, S.; Chen, Y. P.; Yan, Z. M.; Fenniri, H.; Webster, T. J. Self-Assembled Rosette Nanotubes for Incorporating Hydrophobic Drugs in Physiological Environments. *International Journal of Nanomedicine* **2011**, *6*, 101-107.

(92) Cheetham, A. G.; Zhang, P. C.; Lin, Y. A.; Lock, L. L.; Cui, H. G. Supramolecular Nanostructures Formed by Anticancer Drug Assembly. *Journal of the American Chemical Society* **2013**, *135*, 2907-2910.

(93) Kameta, N.; Lee, S. J.; Masuda, M.; Shimizu, T. Biologically Responsive, Sustainable Release from Metallo-Drug Coordinated 1D Nanostructures. *Journal of Materials Chemistry B* **2013**, *1*, 276-283.

(94) Ding, W. X.; Wada, M.; Minamikawa, H.; Kameta, N.; Masuda, M.; Shimizu, T. Cisplatin-Encapsulated Organic Nanotubes by Endo-Complexation in the Hollow Cylinder. *Chemical Communications* **2012**, *48*, 8625-8627.

(95) Geng, Y.; Dalhaimer, P.; Cai, S.; Tsai, R.; Tewari, M.; Minko, T.; Discher, D. E. Shape effects of filaments versus spherical particles in flow and drug delivery. *Nature Nanotechnology* **2007**, *2*, 249-255.

(96) Meilander, N. J.; Pasumarthy, M. K.; Kowalczyk, T. H.; Cooper, M. J.; Bellamkonda, R. V. Sustained release of plasmid DNA using lipid microtubules and agarose hydrogel. *Journal of Controlled Release* **2003**, *88*, 321-331.

(97) Hsieh, W. H.; Chang, S. F.; Chen, H. M.; Chen, J. H.; Liaw, J. H. Oral Gene Delivery with cyclo-(D-Trp-Tyr) Peptide Nanotubes. *Molecular Pharmaceutics* **2012**, *9*, 1231-1249.

(98) Ding, W.; Wada, M.; Kameta, N.; Minamikawa, H.; Shimizu, T.; Masuda, M. Functionalized Organic Nanotubes as Tubular Nonviral Gene Transfer Vector. *Journal of Controlled Release* **2011**, *156*, 70-75.

(99) Jin, Q. X.; Zhang, L.; Cao, H.; Wang, T. Y.; Zhu, X. F.; Jiang, J.; Liu, M. H. Self-Assembly of Copper(II) Ion-Mediated Nanotube and Its Supramolecular Chiral Catalytic Behavior. *Langmuir* **2011**, *27*, 13847-13853.

(100) Huang, Z. P.; Guan, S. W.; Wang, Y. G.; Shi, G. N.; Cao, L. N.; Gao, Y. Z.; Dong, Z. Y.; Xu, J. Y.; Luo, Q.; Liu, J. Q. Self-Assembly of Amphiphilic Peptides into Bio-Functionalized Nanotubes: a Novel Hydrolase Model. *Journal of Materials Chemistry B* **2013**, *1*, 2297-2304.

(101) Yu, L. T.; Banerjee, I. A.; Gao, X. Y.; Nuraje, N.; Matsui, H. Fabrication and Application of Enzyme-Incorporated Peptide Nanotubes. *Bioconjugate Chemistry* **2005**, *16*, 1484-1487.

(102) Gemeay, A. H.; Mansour, L. A.; El-Sharkawy, R. G.; Zaki, A. B. Kinetics of the Oxidative Degradation of Thionine Dye by Hydrogen Peroxide Catalyzed by Supported Transition Metal Ions Complexes. *Journal of Chemical Technology and Biotechnology* **2004**, *79*, 85-96.

(103) Chattopadhyay, T.; Kogiso, M.; Aoyagi, M.; Yui, H.; Asakawa, M.; Shimizu, T. Single Bilayered Organic Nanotubes: Anchors for Production of a Reusable Catalyst with Nickel Ions. *Green Chemistry* **2011**, *13*, 1138-1140.

(104) Chattopadhyay, T.; Kogiso, M.; Asakawa, M.; Shimizu, T.; Aoyagi, M. Copper(II)-Coordinated Organic Nanotube: A Novel Heterogeneous Catalyst for Various Oxidation Reactions. *Catalysis Communications* **2010**, *12*, 9-13.

(105) Schoch, R. B.; Han, J. Y.; Renaud, P. Transport Phenomena in Nanofluidics. *Reviews of Modern Physics* **2008**, *80*, 839-883.

(106) van den Berg, A.; Craighead, H. G.; Yang, P. D. From Microfluidic Applications to Nanofluidic Phenomena. *Chemical Society Reviews* **2010**, *39*, 899-900.

(107) Nogawa, K., Tagawa, Y., Nakajima, M., Arai, F., Shimizu, T., Kamiya, S. & Fukuda, T. Development of Novel Nanopipette with a Lipid Nanotube as Nanochannel. *Journal of Robotics and Mecantronics* **2007**, *19*, 528–534.

(108) Gurrieri, S.; Wells, K. S.; Johnson, I. D.; Bustamante, C. Direct Visualization of Individual DNA Molecules by Fluorescence Microscopy: Characterization of the Factors Affecting Signal/Background and Optimization of Imaging Conditions Using YOYO. *Analytical Biochemistry* **1997**, *249*, 44-53.

(109) Paik, D. H.; Perkins, T. T. Dynamics and Multiple Stable Binding Modes of DNA Intercalators Revealed by Single-Molecule Force Spectroscopy. *Angewandte Chemie-International Edition* **2012**, *51*, 1811-1815.

(110) Smith, S. B.; Finzi, L.; Bustamante, C. Direct Mechanical Measurements of the Elasticity of Single DNA-Molecules by using Magnetic Beads. *Science* **1992**, *258*, 1122-1126.

(111) Krautbauer, R.; Fischerlander, S.; Allen, S.; Gaub, H. E. Mechanical Fingerprints of DNA Drug Complexes. *Single Molecules* **2002**, *3*, 97-103.

(112) Xu, H.; Minter, C. J.; Nagasaka, S.; Ito, T.; Higgins, D. A. Elongation, Alignment, and Guided Electrophoretic Migration of ds-DNA in Flow-Aligned Hexagonal F127 Gels. *Journal of Physical Chemistry B* **2014**, *118*, 4151-4159.

(113) Moerner, W. E.; Fromm, D. P. Methods of Single-Molecule Fluorescence Spectroscopy and Microscopy. *Review of Scientific Instruments* **2003**, *74*, 3597-3619.

(114) Kisley, L.; Landes, C. F. Molecular Approaches to Chromatography Using Single Molecule Spectroscopy. *Analytical Chemistry* **2015**, *87*, 83-98.

(115) Axelrod, D. Total Internal Reflection Fluorescence Microscopy in Cell Biology. *Traffic* **2001**, *2*, 764-774.

(116) Fu, Y.; Ye, F. M.; Sanders, W. G.; Collinson, M. M.; Higgins, D. A. Single Molecule Spectroscopy Studies of Diffusion in Mesoporous Silica Thin Films. *Journal of Physical Chemistry B* **2006**, *110*, 9164-9170.

(117) Park, S. C.; Ito, T.; Higgins, D. A. Dimensionality of Diffusion in Flow-Aligned Surfactant-Templated Mesoporous Silica: A Single Molecule Tracking Study of Pore Wall Permeability. *Journal of Physical Chemistry C* **2015**, *119*, 26101-26110.

(118) Tran-Ba, K. H.; Higgins, D. A.; Ito, T. Single-Molecule Tracking Studies of Flow-Induced Microdomain Alignment in Cylinder-Forming Polystyrene-Poly(ethylene oxide) Diblock Copolymer Films. *Journal of Physical Chemistry B* **2014**, *118*, 11406-11415.

(119) Tran-Ba, K. H.; Higgins, D. A.; Ito, T. Fluorescence Recovery after Photobleaching and Single-Molecule Tracking Measurements of Anisotropic Diffusion within Identical Regions of a Cylinder-Forming Diblock Copolymer Film. *Analytical Chemistry* **2015**, *87*, 5802-5809.

(120) Kisley, L.; Brunetti, R.; Tauzin, L. J.; Shuang, B.; Yi, X.; Kirkeminde, A. W.; Higgins, D. A.; Weiss, S.; Landes, C. F. Characterization of Porous Materials by Fluorescence Correlation Spectroscopy Super-resolution Optical Fluctuation Imaging. *Acs Nano* **2015**, *9*, 9158-9166.

(121) Burkhardt, M.; Schwille, P. Electron Multiplying CCD based Detection for Spatially Resolved Fluorescence Correlation Spectroscopy. *Optics Express* **2006**, *14*, 5013-5020.

(122) Kannan, B.; Guo, L.; Sudhaharan, T.; Ahmed, S.; Maruyama, I.; Wohland, T. Spatially Resolved Total Internal Reflection Fluorescence Correlation Microscopy using an Electron Multiplying Charge-Coupled Device Camera. *Analytical Chemistry* **2007**, *79*, 4463-4470.

(123) Kannan, B.; Har, J. Y.; Liu, P.; Maruyama, I.; Ding, J. L.; Wohland, T. Electron Multiplying Charge-Coupled Device Camera based Fluorescence Correlation Spectroscopy. *Analytical Chemistry* **2006**, *78*, 3444-3451.

(124) Guo, L.; Har, J. Y.; Sankaran, J.; Hong, Y. M.; Kannan, B.; Wohland, T. Molecular Diffusion Measurement in Lipid Bilayers over Wide Concentration Ranges: A Comparative Study. *Chemphyschem* **2008**, *9*, 721-728.

(125) Nakata, M.; Zanchetta, G.; Buscaglia, M.; Bellini, T.; Clark, N. A. Liquid Crystal Alignment on a Chiral Surface: Interfacial Interaction with Sheared DNA Films. *Langmuir* **2008**, *24*, 10390-10394.

(126) Malone, S. M.; Schwartz, D. K. Macroscopic Liquid Crystal Response to Isolated DNA Helices. *Langmuir* **2011**, *27*, 11767-11772.

(127) Zinchenko, A. A.; Chen, N. Compaction of DNA on Nanoscale Three-Dimensional Templates. *Journal of Physics:Condensed Matter* **2006**, *18*, 453-480.

(128) Makarucha, A. J.; Todorova, N.; Yarovsky, I. Nanomaterials in Biological Environment: A Review of Computer Modelling Studies. *European Biophysics Journal* **2011**, *40*, 103-115.

(129) Rill, R. L.; Locke, B. R.; Liu, Y. J.; Van Winkle, D. H. Electrophoresis in Lyotropic Polymer Liquid Crystals. *Proceedings of the National Academy of Sciences of the United States of America* **1998**, *95*, 1534-1539.

(130) Wu, C. H.; Liu, T. B.; Chu, B. Viscosity-Adjustable Block Copolymer for DNA Separation by Capillary Electrophoresis. *Electrophoresis* **1998**, *19*, 231-241.

(131) Kuroda, D.; Zhang, Y.; Wang, J.; Kaji, N.; Tokeshi, M.; Baba, Y. A Viscosity-Tunable Polymer for DNA Separation by Microchip Electrophoresis. *Analytical and Bioanalytical Chemistry* **2008**, *391*, 2543-2549.

(132) Collins, A. M.; Zabkiewicz, J.; Ghiggi, C.; Hauser, J. C.; Burnett, A. K.; Mann, S. Tris(8-hydroxyquinolinato)gallium(III)-Loaded Copolymer Micelles as Cytotoxic Nanoconstructs for Cosolvent-Free Organometallic Drug Delivery. *Small* **2011**, *7*, 1635-1640.

(133) Iwabata, K.; Sugai, U.; Seki, Y.; Furue, H.; Sakaguchi, K. Applications of Biomaterials to Liquid Crystals. *Molecules* **2013**, *18*, 4703-4717.

(134) Wan, F.; Zhang, J.; Lau, A.; Tan, S.; Burger, C.; Chu, B. Nanostructured Copolymer Gels for dsDNA Separation by CE. *Electrophoresis* **2008**, *29*, 4704-4713.

(135) You, S.; Van Winkle, D. H. Single Molecule Observation of DNA Electrophoresis in Pluronic F127. *Journal of Physical Chemistry B* **2010**, *114*, 4171-4177.

(136) Svingen, R.; Alexandridis, P.; Åkerman, B. On the Mechanism of Electrophoretic Migration of DNA in Pluronic Gels. *Langmuir* **2002**, *18*, 8616-8619.

(137) Svingen, R.; Åkerman, B. Mechanism of Electrophoretic Migration of DNA in the Cubic Phase of Pluronic F127 and Water. *Journal of Physical Chemistry B* **2004**, *108*, 2735-2743.

(138) Kirkeminde, A. W.; Torres, T.; Ito, T.; Higgins, D. A. Multiple Diffusion Pathways in Pluronic F127 Mesophases Revealed by Single Molecule Tracking and Fluorescence Correlation Spectroscopy. *Journal of Physical Chemistry B* **2011**, *115*, 12736-12743.

(139) Constantin, D.; Oswald, P.; Imperor-Clerc, M.; Davidson, P.; Sotta, P. Connectivity of the Hexagonal, Cubic, and Isotropic Phases of the C12EO6/H2O Lyotropic Mixture Investigated by Tracer Diffusion and X-ray Scattering. *Journal of Physical Chemistry B* **2001**, *105*, 668-673.

(140) Shiraishi, Y.; Inoue, T.; Hirai, T. Local Viscosity Analysis of Triblock Copolymer Micelle with Cyanine Dyes as a Fluorescent Probe. *Langmuir* **2010**, *26*, 17505-17512.

(141) Nivaggioli, T.; Tsao, B.; Alexandridis, P.; Hatton, T. A. Microviscosity in Pluronic and Tetronic Poly(Ethylene Oxide) Poly(Propylene Oxide) Block-Copolymer Micelles. *Langmuir* **1995**, *11*, 119-126.

(142) Dorfman, K. D.; King, S. B.; Olson, D. W.; Thomas, J. D. P.; Tree, D. R. Beyond Gel Electrophoresis: Microfluidic Separations, Fluorescence Burst Analysis, and DNA Stretching. *Chemical Reviews* **2013**, *113*, 2584-2667.

(143) Tran Ba, K. H.; Everett, T. A.; Ito, T.; Higgins, D. A. Trajectory Angle Determination in One Dimensional Single Molecule Tracking Data by Orthogonal Regression Analysis. *Physical Chemistry Chemical Physics* **2011**, *13*, 1827-1835.

(144) Watson, J. D.; Crick, F. H. C. The Structure of DNA. *Cold Spring Harbor Symposia on Quantitative Biology* **1953**, *18*, 123-131.

(145) Park, S. C.; Ito, T.; Higgins, D. A. Single Molecule Tracking Studies of Flow-Aligned Mesoporous Silica Monoliths: Aging-Time Dependence of Pore Order. *Journal of Physical Chemistry B* **2013**, *117*, 4222-4230.

(146) Reisner, W.; Pedersen, J. N.; Austin, R. H. DNA Confinement in Nanochannels: Physics and Biological Applications. *Report on Progress in Physics* **2012**, *75*, 106601.

(147) Günther, K.; Mertig, M.; Seidel, R. Mechanical and Structural Properties of YOYO-1 Complexed DNA. *Nucleic Acids Res* **2010**, *38*, 6526-6532.

(148) Mel'nikov, S. M.; Khan, M. O.; Lindman, B.; Jonsson, B. Phase behavior of single DNA in mixed solvents. *Journal of American Chemical Society* **1999**, *121*, 1130-1136.

(149) Dawson, J. R.; Harpst, J. A. Light Scattering and Hydrodynamic Properties of Linear and Circular Bacteriophage Lambda DNA. *Biopolymers* **1971**, *10*, 2499-2508.

(150) Ueberschar, O.; Wagner, C.; Stangner, T.; Kuhne, K.; Gutsche, C.; Kremer, F. Drag Reduction by DNA-Grafting for Single Microspheres in a Dilute Lambda-DNA Solution. *Polymer* **2011**, *52*, 4021-4032.

(151) Ouyang, W.; Qiu, Y. Rheological Properties of Polyvinyl Butyral/Pluronic F127/PEG200 Blend Systems. *Journal of Central South University of Technology* **2011**, *18*, 1891-1896.

(152) Malmsten, M.; Linse, P.; Cosgrove, T. Adsorption of PEO-PPO-PEO Block Copolymers at Silica. *Macromolecules* **1992**, *25*, 2474-2481.

(153) Odijk, T. On the Statistics and Dynamics of Confined or Entangled Stiff Polymers. *Macromolecules* **1983**, *16*, 1340-1344.

(154) Reisner, W.; Morton, K. J.; Riehn, R.; Wang, Y. M.; Yu, Z. N.; Rosen, M.; Sturm, J. C.; Chou, S. Y.; Frey, E.; Austin, R. H. Statics and Dynamics of Single DNA Molecules Confined in Nanochannels. *Physical Review Letters* **2005**, *94,* 196101.

(155) Zhang, C.; Zhang, F.; van Kan, J. A.; van der Maarel, J. R. C. Effects of Electrostatic Screening on the Conformation of Single DNA Molecules Confined in a Nanochannel. *Journal of Chemical Physics* **2008**, *128*, 225109.

(156) Tree, D. R.; Wang, Y.; Dorfman, K. D. Extension of DNA in a Nanochannel as a Rod-to-Coil Transition. *Physical Review Letters* **2013**, *110*, 208103.

(157) Jing, J. P.; Reed, J.; Huang, J.; Hu, X. H.; Clarke, V.; Edington, J.; Housman, D.; Anantharaman, T. S.; Huff, E. J.; Mishra, B.; Porter, B.; Shenker, A.; Wolfson, E.; Hiort, C.; Kantor, R.; Aston, C.; Schwartz, D. C. Automated High Resolution Optical Mapping using Arrayed, Fluid-

Fixed DNA Molecules. *Proceedings of the National Academy of Sciences of the United States of America* **1998**, *95*, 8046-8051.

(158) Dimalanta, E. T.; Lim, A.; Runnheim, R.; Lamers, C.; Churas, C.; Forrest, D. K.; de Pablo, J. J.; Graham, M. D.; Coppersmith, S. N.; Goldstein, S.; Schwartz, D. C. A Microfluidic System for Large DNA Molecule Arrays. *Analytical Chemistry* **2004**, *76*, 5293-5301.

(159) Bong, D. T.; Clark, T. D.; Granja, J. R.; Ghadiri, M. R. Self-assembling Organic Nanotubes. *Angewandte Chemie-International Edition* **2001**, *40*, 988-1011.

(160) Shimizu, T. Self-Assembled Organic Nanotubes: Toward Attoliter Chemistry. *Journal of Polymer Science Part a-Polymer Chemistry* **2008**, *46*, 2601-2611.

(161) Yan, X.; He, Q.; Wang, K.; Duan, L.; Cui, Y.; Li, J. Transition of Cationic Dipeptide Nanotubes into Vesicles and Oligonucleotide Delivery. *Angewandte Chemie-International Edition* **2007**, *46*, 2431-2434.

(162) Hughes, G. A. Nanostructure-Mediated Drug Delivery. *Nanomedicine* **2005**, *1*, 22-30.

(163) Langer, R. Drug Delivery and Targeting. *Nature* **1998**, *392*, 5-10.

(164) Fu, Y.; Kao, W. J. Drug Release Kinetics and Transport Mechanisms of Non-degradable and Degradable Polymeric Delivery Systems. *Expert Opinion on Drug Delivery* **2010**, *7*, 429-444.

(165) Maderuelo, C.; Zarzuelo, A.; Lanao, J. M. Critical Factors in the Research of Drugs from Sustained Release Hydrophilic Matrices. *Journal of Controlled Release* **2011**, *154*, 2-19.

(166) Okamoto, K.; Shook, C. J.; Bivona, L.; Lee, S. B.; English, D. S. Direct Observation of Wetting and Diffusion in the Hydrophobic Interior of Silica Nanotubes. *Nano Letters* **2004**, *4*, 233-239.

(167) Guo, L.; Chowdhury, P.; Fang, J. Y.; Gai, F. Heterogeneous and Anomalous Diffusion inside Lipid Tubules. *Journal of Physical Chemistry B* **2007**, *111*, 14244-14249.

(168) Boening, D.; Groemer, T. W.; Klingauf, J. Applicability of an EM-CCD for Spatially Resolved TIR-ICS. *Optics Express* **2010**, *18*, 13516-13528.

(169) Sabatini, D. A. Sorption and Intraparticle Diffusion of Fluorescent Dyes with Consolidated Aquifer Media. *Ground Water* **2000**, *38*, 651-656.

(170) Koppel, D. E. Statistical Accuracy in Fluorescence Correlation Spectroscopy. *Physical Review A* **1974**, *10*, 1938-1945.

(171) Tcherniak, A.; Reznik, C.; Link, S.; Landes, C. F. Fluorescence Correlation Spectroscopy: Criteria for Analysis in Complex Systems. *Analytical Chemistry* **2009**, *81*, 746-754.

(172) Schenter, G. K.; Lu, H. P.; Xie, X. S. Statistical Analyses and Theoretical Models of Single-Molecule Enzymatic Dynamics. *Journal of Physical Chemistry A* **1999**, *103*, 10477-10488.

(173) Wirth, M. J.; Swinton, D. J. Single-molecule Probing of Mixed-mode Adsorption at a Chromatographic Interface. *Analytical Chemistry***1 998**, *70*, 5264-5271.

(174) Kolin, D. L.; Costantino, S.; Wiseman, P. W. Sampling Effects, Noise, and Photobleaching in Temporal Image Correlation Spectroscopy. *Biophysical Journal* **2006**, *90*, 628-639.

(175) Elson, E. L.; Magde, D. Fluorescence Correlation Spectroscopy. I. Conceptual Basis and Theory. *Biopolymers* **1974**, *13*, 1-27.

(176) Ye, F.; Collinson, M. M.; Higgins, D. A. Molecular Orientation and its Influence on Autocorrelation Amplitudes in Single-molecule Imaging Experiments. *Analytical Chemistry* **2007**, *79*, 6465-6472.

(177) Chambers, R. W.; Kajiwara, T.; Kearns, D. R. Effect of Dimer Formation on the Electronic Absorption and Emission Spectra of Ionic Dyes. Rhodamines and Other Common Dyes. *Journal of Physical Chemistry* **1974**, *78*, 380-387.

(178) Kasnavia, T.; Vu, D.; Sabatini, D. A. Fluorescent Dye and Media Properties Affecting Sorption and Tracer Selection. *Ground Water* **1999**, *37*, 376-381.

(179) Yui, H.; Guo, Y.; Koyama, K.; Sawada, T.; John, G.; Yang, B.; Masuda, M.; Shimizu, T. Local Environment and Property of Water inside the Hollow Cylinder of a Lipid Nanotube. *Langmuir* **2005**, *21*, 721-727.

(180) Ray, K.; Nakahara, H. Adsorption of Sulforhodamine Dyes in Cationic Langmuir-Blodgett Films: Spectroscopic and Structural Studies. *Journal of Physical Chemistry B***2 002**, *106*, 92-100.

(181) Kameta, N.; Minamikawa, H.; Someya, Y.; Yui, H.; Masuda, M.; Shimizu, T. Confinement Effect of Organic Nanotubes Toward Green Fluorescent Protein (GFP) Depending on the Inner Diameter Size. *Chemistry - A European Journal* **2010**, *16*, 4217-4223.

(182) van der Vegte, E. W.; Hadziioannou, G. Acid-Base Properties and the Chemical Imaging of Surface-Bound Functional Groups Studied with Scanning Force Microscopy. *Journal of Physical Chemistry B* **1997**, *101*, 9563-9569.

(183) Moses, P. R.; Wier, L. M.; Lennox, J. C.; Finklea, H. O.; Lenhard, J. R.; Murray, R. W. X-ray Photoelectron Spectroscopy of Alkylamine-Silanes Bound to Metal Oxide Electrodes. *Analytical Chemistry* **1978**, *50*, 576-585.

(184) Skaug, M. J.; Mabry, J. N.; Schwartz, D. K. Single-Molecule Tracking of Polymer Surface Diffusion. *Journal of American Chemical Society* **2014**, *136*, 1327-1332.

(185) Walder, R.; Nelson, N.; Schwartz, D. K. Single Molecule Observations of Desorption-Mediated Diffusion at the Solid-Liquid Interface. *Physical Reviews Letter* **2011**, *107*, 156102.

(186) Giri, D.; Ashraf, K. M.; Collinson, M. M.; Higgins, D. A. Single-Molecule Perspective on Mass Transport in Condensed Water Layers over Gradient Self-Assembled Monolayers. *Journal of Physical Chemistry C* **2015**, *119*, 9418-9428.

(187) Eissen, M.; Metzger, J. O.; Schmidt, E.; Schneidewind, U. 10 Years after Rio - Concepts on the Contribution of Chemistry to a Sustainable Development. *Angewandte Chemie-International Edition* **2002**, *41*, 414-436.

(188) Tanaka, K.; Toda, F. Solvent-Free Organic Synthesis. *Chemical Reviews* **2000**, *100*, 1025-1074.

(189) Coperet, C.; Chabanas, M.; Saint-Arroman, R. P.; Basset, J. M. Homogeneous and Heterogeneous Catalysis: Bridging the Gap through Surface Organometallic Chemistry. *Angewandte Chemie-International Edition* **2003**, *42*, 156-181.

(190) Schlogl, R. Heterogeneous Catalysis. *Angewandte Chemie-International Edition* **2015**, *54*, 3465-3520.

(191) Gawande, M. B.; Goswami, A.; Felpin, F. X.; Asefa, T.; Huang, X. X.; Silva, R.; Zou, X. X.; Zboril, R.; Varma, R. S. Cu and Cu-Based Nanoparticles: Synthesis and Applications in Review Catalysis. *Chemical Reviews* **2016**, *116*, 3722-3811.

(192) Zhou, Y.; Shimizu, T. Lipid Nanotubes: a Unique Template to Create Diverse One-Dimensional Nanostructures. *Chemistry of Materials* **2008**, *20*, 625-633.

(193) Lapointe, D.; Fagnou, K. Overview of the Mechanistic Work on the Concerted Metallation-Deprotonation Pathway. *Chemistry Letters* **2010**, *39*, 1119-1126.

(194) Kurniasih, I. N.; Liang, H.; Mohr, P. C.; Khot, G.; Rabe, J. P.; Mohr, A. Nile Red Dye in Aqueous Surfactant and Micellar Solution. *Langmuir* **2015**, *31*, 2639-2648.

(195) Giri, D.; Hanks, C. N.; Collinson, M. M.; Higgins, D. A. Single-Molecule Spectroscopic Imaging Studies of Polarity Gradients Prepared by Infusion-Withdrawal Dip-Coating. *Journal of Physical Chemistry C* **2014**, *118*, 6423-6432.

(196) Kumarasinghe, R.; Higgins, E. D.; Ito, T.; Higgins, D. A. Spectroscopic and Polarization-Dependent Single-Molecule Tracking Reveal the One-Dimensional Diffusion Pathways in Surfactant-Templated Mesoporous Silica. *Journal of Physical Chemistry C* **2016**, *120*, 715-723.

(197) Hess, C. M.; Riley, E. A.; Palos-Chavez, J.; Reid, P. J. Measuring the Spatial Distribution of Dielectric Constants in Polymers through Quasi-Single Molecule Microscopy. *Journal of Physical Chemistry B* **2013**, *117*, 7106-7112.

(198) Nagy, K.; Gokturk, S.; Biczok, L. Effect of Microenvironment on the Fluorescence of 2-Hydroxy-Substituted Nile Red Dye: a New Fluorescent Probe for the Study of Micelles. *Journal of Physical Chemistry A* **2003**, *107*, 8784-8790.

(199) Steigman, J.; Sussman, D. Acid-Base Reactions in Concentrated Aqueous Quaternary Ammonium Salt Solutions. I. Strong Acids and Bases Carboxylic Acids Amines and Phenol. *Journal of the American Chemical Society* **1967**, *89*, 6400-6406.